MiniBAR/GARRE1 is a dual Rac and Rab effector required for ciliogenesis

Murielle Serres, Ronan Shaughnessy, Sophie Escot, Hussein Hammich, Frédérique Cuvelier, Audrey Salles, Murielle Rocancourt, Quentin Verdon, Anne-Lise Gaffuri, Yannick Sourigues, et al.

MiniBAR / GARRE1 is a dual Rac and Rab effector required for ciliogenesis

Murielle P. Serres[1,9], Ronan Shaughnessy[1,9], Sophie Escot[2,9], Hussein Hammich[3], Frédérique Cuvelier[1], Audrey Salles[4], Murielle Rocancourt[1], Quentin Verdon[1], Anne-Lise Gaffuri[1], Yannick Sourigues[3], Gilles Malherbe[3], Leonid Velikovsky[3], Florian Chardon[3], Nathalie Sassoon[1], Jean-Yves Tinevez[5], Isabelle Callebaut[6], Etienne Formstecher[7], Anne Houdusse[3], Nicolas David[2], Olena Pylypenko[3,8] and Arnaud Echard[1,10,*]

[1]Institut Pasteur, Université de Paris, CNRS UMR3691, Membrane Traffic and Cell Division Lab, 25-28 rue du Dr Roux, F-75015 Paris, France

[2]Laboratoire d'Optique et Biosciences (LOB), CNRS, INSERM, Ecole Polytechnique, Institut Polytechnique de Paris, 91120 Palaiseau, France.

[3]Institut Curie, PSL Research University, CNRS UMR144, Structural Motility, 26 rue d'Ulm, F-75005 Paris, France

[4] Institut Pasteur, Université de Paris, UTechS Photonic BioImaging (UTechS PBI), Centre de Recherche et de Ressources Technologiques C2RT, 25-28 rue du Dr Roux, F-75015 Paris, France

[5]Institut Pasteur, Université de Paris, Image Analysis Hub, 25-28 rue du Dr Roux, F-75015 Paris, France

[6]Sorbonne Université, Muséum National d'Histoire Naturelle, UMR CNRS 7590, Institut de Minéralogie, de Physique des Matériaux et de Cosmochimie, IMPMC, Paris, France

[7]Hybrigenics Services SAS, 1 rue Pierre Fontaine 91000 Evry – Courcouronnes, France.

[8]Present address: Institut Curie, PSL Research University, CNRS UMR144, Dynamics of Intracellular Organization, 26 rue d'Ulm, F-75005 Paris, France

[9]These authors contributed equally

[10]Lead contact

*Correspondence: arnaud.echard@pasteur.fr

SUMMARY

Cilia protrude from the cell surface and play critical roles in intracellular signaling, environmental sensing and development. Actin-dependent contractility and intracellular trafficking are both required for ciliogenesis, but little is known about how these processes are coordinated. Here, we identified a Rac1- and Rab35-binding protein with a truncated BAR domain that we named MiniBAR (aka KIAA0355/GARRE1) which plays a key role in ciliogenesis. MiniBAR colocalizes with Rac1 and Rab35 at the plasma membrane and on intracellular vesicles trafficking to the ciliary base and exhibits fast pulses at the ciliary membrane. MiniBAR depletion leads to short cilia resulting from abnormal Rac-GTP/Rho-GTP levels, increased acto-Myosin II-dependent contractility together with defective trafficking of IFT88 and ARL13B into cilia. MiniBAR-depleted zebrafish embryos display dysfunctional short cilia and hallmarks of ciliopathies including left-right asymmetry defects. Thus, MiniBAR is a dual Rac and Rab effector that controls both actin cytoskeleton and membrane trafficking for ciliogenesis.

GRAPHICAL ABSTRACT

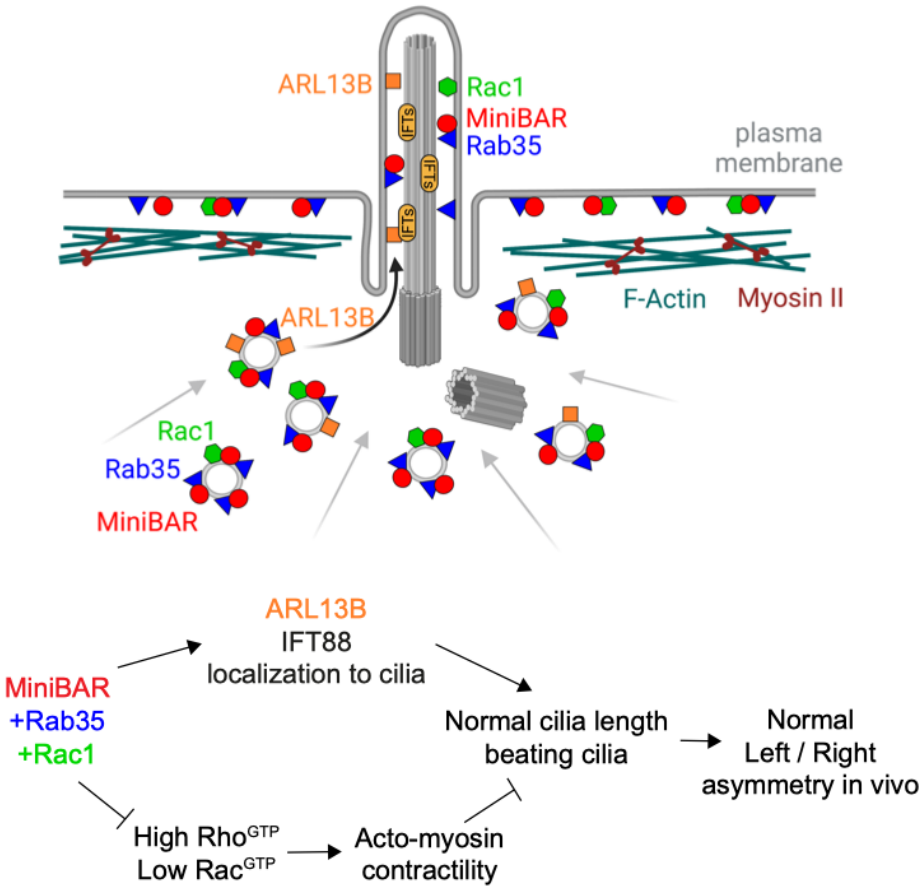

INTRODUCTION

Flagella and cilia are evolutionarily conserved microtubule-based protrusions essential for cell locomotion, fluid movement and sensing of extracellular cues[1]. Primary cilia are found at the surface of most vertebrate cells and function as cellular antennas that detect various chemical and mechanical signals, thereby playing crucial roles in intracellular signaling and development[1]. Motile cilia in the embryonic node control left-right patterning of the body plan, in particular by generating a directional fluid flow essential for symmetry breaking of key transcription factors[2]. Strikingly, dozens of proteins are required for the formation and maintenance of cilia[3,4]. Mutations of the corresponding genes in humans can lead to severe diseases known as ciliopathies in up to 1 out of 725 individuals, which can cause various pathologies including polycystic kidney diseases, nephrophtisis, heterotaxis and *situs inversus*, and Meckel-Gruber, Bardet-Biedl or Joubert syndromes[5].

Primary cilia consist of a membrane evagination protruding from the cell surface that surrounds a microtubule-based axoneme nucleated by a basal body[6]. Depending on the cell type, the basal body either docks to the plasma membrane and the primary cilium directly growths from this location, or the axoneme starts to grow into an intracellular ciliary vesicle which subsequently fuses to the plasma membrane, as in RPE-1 (Retinal Pigment Epithelial) cells[7,8]. In both pathways, the assembly, growth, maintenance and proper functioning of the cilium requires the selective delivery of membrane and cytosolic cargoes within the cilium. This relies on both highly conserved intraflagellar transport (IFT) and intracellular membrane trafficking[9]. Accordingly, Rab GTPases, which are key regulators of membrane trafficking in eukaryotic cells[10], play a pivotal role in cilium biology, with at least ten Rab proteins involved in cilium formation, function and composition[11]. For instance, a Rab11-Rabin8-Rab8 cascade and their effectors (EHD1, MICAL-L1 and the exocyst), together with the coat and adaptor complex BBSome, control trafficking to the ciliary vesicle and cilium growth[12-17].

In parallel, the actin cytoskeleton and actin binding proteins participate in several aspects of cilia formation, elongation and shedding[18-23]. Importantly, excessive actin polymerization and contractility impair ciliogenesis possibly by imposing a physical barrier to cilia-targeted vesicle transport and by increasing cortical or membrane tension that prevents outward growth of cilia[18,19]. Consequently, pharmacological inhibition of F-actin polymerization and of acto-Myosin II-dependent contractility can enhance ciliogenesis in

normal cells or restore normal ciliogenesis in cells depleted of important ciliary proteins[3,24,25]. Thus, both intracellular trafficking and the actin cytoskeleton dynamics play critical roles in cilia initiation and growth. Yet, little is known about how these two important cellular processes are coordinated during ciliogenesis.

Rab35 is a plasma membrane and endosomal Rab GTPase implicated in diverse cellular functions, ranging from cytokinesis, phagocytosis, cell migration and neurite outgrowth to autophagy[26-28]. Recently, Rab35 was reported to control cilia length and function, both in human cultured cells and in zebrafish embryos, but the Rab35 effectors involved remain unknown[29]. Here, we identified MiniBAR as a Rab35 and Rac1 effector with a truncated BAR domain that plays a critical role in ciliogenesis in RPE-1 cells and zebrafish embryos. We demonstrate that the interaction of MiniBAR with each GTPase is necessary for proper cilia growth. We also show that this dual Rab/Rac effector promotes ciliogenesis by controlling and coordinating both membrane trafficking of key ciliary cargoes and acto-Myosin II-dependent cellular contractility.

RESULTS

MiniBAR is a dual Rac1 and Rab35 effector with a truncated BAR domain

Using both GTP-locked mutants of Rab35 ($Rab35^{Q67L}$) and of Rac1 ($Rac1^{G12V}$) as baits in yeast two hybrid screens, we identified the poorly characterized human protein KIAA0355 among the top hits (see Methods), indicating that KIAA0355 might be a dual Rab35 and Rac1 effector protein. Interestingly, while we were studying KIAA0355, this protein was found through systematic Rho-family GTPase proximity interaction assays and named GARRE1 for "Granule-associated Rac and RhoG effector protein 1", since it directly interacted *in vitro* with $Rac1^{G12V}$ and potentially with other Rac-family members —Rac2, Rac3 and RhoG[30]. However, neither the function of this 1070 aa protein conserved in Vertebrates (**Figure 1A and S1A**), nor the relevance of its interaction with Rac1 were known. Based on its structure and localization (see below), we propose to name KIAA0355/GARRE1 as MiniBAR, and we will use this alias here.

We first delimited the Rac1 binding domain or Rac1BD (aa 70-208, $MiniBAR^{70\text{-}208}$) and the Rab35 binding domain or Rab35BD (aa 225-553, $MiniBAR^{225\text{-}553}$) using yeast two hybrid assays (**Figure 1A-B**). Each domain as well as the full-length protein interacted with Rac1 and Rab35 mutants preferentially bound to GTP ($Rac1^{Q61L}$, $Rab35^{Q67L}$), while interactions with GDP-bound/nucleotide free mutants ($Rac1^{T17N}$, $Rab35^{S22N}$) were not detected (**Figure 1B**). Among the 55 Rab GTPases tested, only Rab35 interacted with MiniBAR, suggesting that MiniBAR is a Rab35-specific effector (**Figure S1B**). Gel filtration experiments with recombinant, purified proteins demonstrated that Rac1BD and Rab35BD assembled into complexes with the Rac1 and Rab35 loaded with non hydrolyzable GTP analogue, respectively (**Figure 1C and S1C**). These complexes were not detected in the presence of Rac1 loaded with GDP and were decreased in the presence of Rab35 loaded with GDP (**Figure S1C**). Importantly, Rac1 and Rab35 also interacted individually and simultaneously with $MiniBAR^{70\text{-}553}$ containing the two binding domains (**Figure S1D-E**). Thus, based on preferential binding to GTP-bound GTPases, MiniBAR can be considered as a dual Rac1-Rab35 effector. Isothermal titration calorimetry (ITC) revealed that MiniBAR interacted with GTP-bound Rac1 and Rab35, with Kds of approximately 0.2 μM and 2-4 μM, respectively (**Figure S1F**). Finally, preferential binding of endogenous MiniBAR to GTP-bound Rac1 and Rab35 was validated by coimmunoprecipitation experiments from RPE-1 cells (**Figure 1D**). Altogether, MiniBAR

interacts preferentially with GTP-bound sates of Rac1 and Rab35 via two distinct, adjacent domains.

The Rac1BD overlaps with a domain of unknown function 4745 (DUF4745) in the Pfam database that is predicted to form a BAR (Bin/Amphiphysin/Rvs) domain, which is known to sense membrane curvature[30,31] (**Figure S2A**). Intriguingly, we noticed that the helices that form "extended arms" in the canonical BAR-domain of Amphiphysin (**grey in Figure S2A**) were shorter in DUF4745 and MiniBAR (**red in Figure S2A**). Accordingly, the crystal structure of the Rac1BD that we solved (**Figure 1E**, **Movie 1 and Table S1**) revealed an unusual, truncated or "Mini" BAR domain consisting of a 3-helix-based homodimer, with strong similarity to the central part of a canonical BAR-domain[31] (**Figure S2B**, top panels). The "Mini" BAR domain surface has a positively charged cluster that might mediate interactions with negatively charged membranes (**Figure S2B**, lower panels). However, this cluster is condensed in the middle part of the MiniBAR homodimer, which differs from the more peripheral distribution in canonical BAR domains (**Figure S2B**). Small-Angle X-ray Scattering (SAXS) experiments of the Rac1BD are consistent with the formation of a homodimer in solution (**Figure S2C and Table S1**). In addition, the Rac1BD : Rac1 complex molecular mass defined by Multi-Angle-Light-Scattering (MALS) corresponds to 2 Rac1 : 1 Rac1BD homodimer stoichiometry (**Table S1**).

The crystal structure of the Rab35BD that we determined revealed that it comprises three subdomains (SD-1,2,3), with the topologically central subdomain SD-3 exhibiting a Cystatin/Monellin characteristic protein fold (**Figure 1F, S3A-C, Movie 1 and Table S1**). SAXS further showed that the Rab35BD is monomeric in solution, with the last 40 residues (including helix α13 and a preceding loop) being flexible (**Figure S2D and Table S1**). Furthermore, oligomerization of the Rac1BD resulted in the dimerization of the entire Rac1BD-Rab35BD unit (MiniBAR$^{70\text{-}553}$) (**Table S1**). Finally, SAXS suggested that different orientations of two Rab35BDs with respect to the central Rac1BD dimer are likely present in solution (**Figure S2E**).

Based on these biochemical and structural evidence, we conclude that MiniBAR is a Rac1 and Rab35 binding protein and propose a structural model for the overall organization of the complex (**Figure 1G** and results below for Rac/Rab interfaces). To our knowledge, MiniBAR represents the only known dual Rho-family and Rab-family interacting protein with a truncated BAR domain.

MiniBAR partially colocalizes with Rac1 and Rab35 at the plasma membrane and on dynamic intracellular vesicles

GTP-bound Rac1 localizes at the plasma membrane and on intracellular compartments, including endosomes, where it activates actin polymerization[32,33]. In conditions that do not induce cilia formation, time-lapse spinning-disk confocal microscopy revealed that stably expressed MiniBAR-GFP largely colocalized with mCherry-Rac1^{WT} at plasma membrane ruffles in RPE-1 cells (**Figure 2A and Movie 2**). MiniBAR also partially colocalized with mCherry-Rac1^{WT} on dynamic intracellular vesicles, with approximately 60% of MiniBAR vesicles being positive for Rac1 (**Figure 2A and Movie 2**). Similar results were obtained in cells expressing mCherry-Rac1^{Q61L} (**Figure S4A**).

GTP-bound Rab35 is known to localize at the plasma membrane and on a particular class of intracellular recycling endosomes[34-39]. As observed with Rac1, MiniBAR-GFP colocalized with mCherry-Rab35^{WT} at plasma membrane ruffles and protrusions (**Figure 2B and Movie 2**) and was found on dynamic vesicles that were largely positive (> 75%) for mCherry-Rab35^{WT} (**Figure 2B and Movie 2**). MiniBAR/KIAA0355 was recently shown to establish proximity labeling with components (GW182 and Ago2) of membrane-less, phase-separated RNA-containing P-granules[30,40]. However, co-localization of MiniBAR with P-granules has not been directly investigated. In our experimental conditions and cells, we found that endogenous MiniBAR is present on dynamic membrane vesicles rather than on membrane-less P-granules (**Figure S4B-G**).

Consistent with membrane association, MiniBAR-GFP was enriched at the extremities and/or in discrete spots along intracellular tubulo-vesicles labelled by MICAL-L1, a marker of the Rab35 recycling endosomes[36,41] (**Figure S4H**). Videomicroscopy confirmed the uneven localization of MiniBAR along MICAL-L1 tubules in cells expressing both MICAL-L1-GFP and MiniBAR-mCherry (**Figure 2C and Movie 3**). Finally, triple co-localization of GFP-Rac1, mCherry-Rab35 and MiniBAR-iRFP was observed on intracellular vesicular structures and at the plasma membrane (**Figure 2D**). Noteworthy, the formation of prominent MiniBAR-positive tubules was induced by the expression of Rab35 and even more potently by its co-expression with Rac1 (**Figure 2D**), suggesting that the three proteins act together to sculpt internal membranes.

We conclude that MiniBAR partially colocalizes with Rac1 and Rab35 at the plasma membrane and on dynamic intracellular vesicles in RPE-1 cells.

Direct MiniBAR / Rab35 interaction is required for vesicular localization of MiniBAR

Guided by our crystal structures (**Figure 1E-F**), we next designed specific point mutations in MiniBAR that selectively disrupted its binding to either Rac1 or Rab35 (**Figure S5A**). Point mutations A140V (as well as A140T and M144K) in helix α2 of Rac1BD and A461R in helix α11 of Rab35BD abolished the interaction of full-length MiniBAR with Rac1 and Rab35, respectively (**Figure S5A**). The corresponding mutations in recombinant MiniBAR$^{70\text{-}553}$ (Rac1BD-Rab35BD) also abolished the direct binding to the corresponding GTPase but left unchanged the binding to the other partner (**Figure 2E-F**). The results of the experimental mutational analysis are consistent with the AlphaFold[42] predicted models of the GTPases/MiniBAR complexes (**Figure S5B**). Thus, A140V in MiniBAR selectively disrupts the interaction with Rac1, while A461R selectively disrupts the interaction with Rab35.

Full-length MiniBAR^{A140V}-GFP localized to the plasma membrane and remained associated with MICAL-L1 intracellular structures (**Figure 2G**). In contrast, MiniBAR^{A461R}-GFP largely lost its association with MICAL-L1 vesicles, while preserving its association with the plasma membrane (**Figure 2G**). We conclude that the interaction of MiniBAR with intracellular vesicles critically depends on its ability to interact with Rab35 but not with Rac1.

MiniBAR accumulates at the ciliary base and rapidly pulses at the ciliary membrane

Since intracellular trafficking and notably Rab35 have been recently implicated in cilium biology, we next examined MiniBAR localization during ciliogenesis. Super-resolution structured illumination microscopy in RPE-1 cells after serum starvation —which induces cilia formation— revealed that endogenous MiniBAR accumulated as vesicular structures surrounding the ciliary base in 100 % of ciliated cells (n= 157 cells) (**Figure 3A and S6A** for staining specificity). Time course after serum removal showed that MiniBAR staining was present before cilia start to elongate, culminated in the early times of ciliogenesis (2-4 h) but remained at the ciliary base at later steps of ciliogenesis (**Figure 3B**). Videomicroscopy confirmed that trafficking at the ciliary base of MiniBAR-GFP vesicles positive for Rac1 and Rab35 occurred before (**Figure 3C-D)** and during cilia elongation (**Figure 3E-F)**. Of note, serum starvation did not significantly change the percentage of MiniBAR vesicles positive for mCherry-Rac1^{WT}, as compared to non-starved cells (**Figure S6B**). Together, the timing and localization data suggest that MiniBAR vesicles could deliver cargoes in the ciliary base region, before and during cilia elongation.

Beside dynamic tubulo-vesicles at the ciliary base (**Figure 3G**, yellow arrowhead), MiniBAR-GFP was usually present at low levels at the plasma membrane, in particular at the ciliary membrane. However, while acquiring movies at 2 second frequencies, we observed striking, transient accumulations of MiniBAR-GFP along cilia, as shown in **Figure 3G** (white brackets) **and Movie 4**. MiniBAR-GFP could fill the entire axoneme within 2-4 seconds and accumulated strongly in cilia in the next 15 seconds before rapidly disappearing (**Figure 3G**). In this example, 5 distinct MiniBAR pulses were observed during a 6-minute long movie. We could distinctly observe MiniBAR-GFP as lines parallel to the axoneme signal at the resolution of confocal microscopy (**Figure 3G**, time point 189 s), suggesting that MiniBAR-GFP associated with the ciliary membrane. At least one MiniBAR pulse was observed during 6-minutes long movies in approximately 60% of the ciliated cells with clear SiR-Tubulin-positive axonema (as in **Figure 3G**) and analyzed 4-8 hours after serum removal (**Figure 3H**). Although irregular, one pulse every 1.6 ± 1.16 minutes (mean ± SD, n= 27 cilia) was detected in pulsating cells in average. When movies were extended to 12 minutes, all ciliated cells showed at least one MiniBAR pulse along cilia 4-8 hours after serum removal (n = 10/10 cells). We observed that the proportion of ciliated cells that displayed MiniBAR pulses in 6-minute long movies progressively decreased during the course of ciliogenesis: 59% (n= 34/58) at 4-8 hours after serum removal, 51 % (n= 22/43) at 12-16 hours and 19% (n= 13/16) at 24-28 hours. Of note, pulses could still be observed in a fraction of cells when cilia elongation stopped (24-28 hours post-starvation) (**Figure S6C**).

mCherry-Rac1 was found at constant levels along the cilium (**Figure 3I**) and MiniBAR^{A140V} pulsed in as many cells as wild-type MiniBAR (**Figure 3H**), indicating that Rac1/MiniBAR interaction is not required for MiniBAR pulsatile behavior. In contrast, several lines of evidence indicated that Rab35 drives MiniBAR pulsation in cilia. First, mCherry-Rab35 also showed pulsatile behavior, and MiniBAR pulses occurred simultaneously (**Figure 3j and Movie 5**). Second, MiniBAR^{A461R}-GFP never showed pulsatile behavior (**Figure 3H**, n= 0/23 cells). Third, Rab35 depletion essentially abolished MiniBAR pulses in cilia (**Figure 3H**, n= 1/11 cilia). Altogether, high-frequency acquisition movies revealed the existence of fast (38 s ± 23.6 s, mean ± SD, n= 35 pulses from 14 cells) pulses of MiniBAR at the ciliary membrane that critically depend on its interaction with Rab35.

MiniBAR promotes cilia growth and controls the localization of IFT88 and ARL13 into cilia

To investigate the function of MiniBAR, we used RNAi to knockdown MiniBAR in RPE-1 cells (**Figure 4A**). We verified that MiniBAR depletion did not impact endogenous Rab35 levels (**Figure S6D**) and had no effect on Rab35-GTP levels in cells (**Figure S6E**). Forty-eight hours after induction of ciliogenesis, the proportion of ciliated cells was modestly but reproducibly decreased upon MiniBAR depletion (**Figure 4B**). Importantly, cilia length was significantly reduced (**Figure 4C**). These results were confirmed with a second, independent siRNA (**Figure S6F-G**). Using stable cell lines that expressed siRNA-resistant version of wild-type MiniBAR-GFP or mutants (**Figure S6H**), we observed that the percentage of ciliated cells as well as cilia length in knock-down cells were rescued by the expression of wild-type MiniBAR (**Figure 4D-E**) but not MiniBAR^{A140V} or MiniBAR^{A461R} mutants (**Figure 4D-E**). Thus, MiniBAR promotes primary cilia formation and elongation in RPE-1 cells, and its interaction with both Rac1 and Rab35 is required for its function in ciliogenesis.

Both the Joubert syndrome protein ARL13B (associated with anterograde IFT-B trains) and the IFT-B train component IFT88 promote cilia elongation[43-47]. Consistent with a key role of MiniBAR in controlling cilia length, we observed a 2-fold reduction of the mean intensity of endogenous ARL13B present in cilia upon MiniBAR depletion (**Figure 4F and Figure S6I**). Expression of MiniBAR^{WT} or MiniBAR^{A140V}, but not of MiniBAR^{A461R} restored the cilia localization of ARL13B in MiniBAR-depleted cells (**Figure 4G**), indicating that MiniBAR's interaction with Rab35 is key for ARL13B correct localization. ARL13B is known to traffic intracellularly on vesicles labelled by Rab22/ARF6 in non-ciliated cells[48]. Since the ARF6 and the Rab35 pathways are physically and functionally connected[36,37,41,49,50], we investigated whether ARL13B could partially traffic through the MiniBAR pathway. Videomicroscopy in cells co-expressing ARL13B-mCherry and MiniBAR-GFP revealed that ARL13B frequently co-localized with MiniBAR on moving vesicles (56% of ARL13B vesicles were positive for MiniBAR, n = 20-95 vesicles analyzed per cell from 6 cells, **Figure 4H and Movie 6**). We conclude that a major pool of ARL13B is transported by the MiniBAR vesicles in ciliated cells. In addition, the correct accumulation of ARL13B in cilia relies on the presence of MiniBAR and on its interaction with Rab35.

Beside ARL13B, we observed that IFT88 was mislocalized in MiniBAR-depleted cells. In control cells, IFT88 localized both at the ciliary base (star) and within the cilium (bracket) in 85% of cilia (**Figure 4I**). In MiniBAR-depleted cells, IFT88 was detected only at the ciliary base

more frequently than in control cells (**Figure 4I**). Again, the interaction between MiniBAR and Rab35 (but not with Rac1) was necessary for the correct localization of IFT88 within cilia, where it fulfills its IFT function (**Figure 4J**).

We conclude that both MiniBAR and its interaction with Rab35 are required for the normal localization of ARL13B and IFT88 to cilia. This likely explains, at least in part, how MiniBAR controls cilia elongation.

MiniBAR also controls cilia length by regulating actin-dependent contractility and RhoA vs. Rac1 activation

Beside trafficking and cargo delivery to the cilia, cilia elongation depends on the actin cytoskeleton, and excessive acto-Myosin II activation is detrimental for ciliogenesis[18,19]. In MiniBAR-depleted cells, we observed numerous, closely packed and thin stress fibers labelled with fluorescent phalloidin, instead of a few and thick stress fibers seen in control cells (**Figure 5A**). Associated with these changes in global actin organization, the total F-actin levels and the intensity of the Ser19 phospho-MRLC staining —a proxy of Myosin II activation— were increased in MiniBAR-depleted cells (**Figure 5A-B and Figure S6J**). Since MRLC phosphorylation depends on kinases such as the Rho-activated kinase (ROCK), we hypothesized that the Rho GTPase might be over-activated in MiniBAR-depleted cells. Accordingly, pull-down assays using Rho effectors revealed that the levels of GTP-bound RhoA ($RhoA^{GTP}$) were 3-fold higher upon MiniBAR depletion, as compared to control cells (**Figure 5C**). Consistent with the known mutual antagonism between Rac and Rho GTPases[51], $Rac1^{GTP}$ levels tended to be reduced in MiniBAR-depleted cells (**Figure 5C**). Thus, the presence of MiniBAR limits acto-Myosin II-dependent cellular contractility.

To test whether the increased contractility observed upon MiniBAR depletion could impact on cilia length, we treated MiniBAR-depleted cells with the ROCK inhibitor Y27632 to reduce Myosin II activity (**Figure 5D**). We found that both the decrease in the percentage of ciliated cells and the shortening of cilia observed upon MiniBAR depletion were partially rescued by treating the cells with Y27632 (**Figure 5D-E**). Of note, these relatively low doses of Y27632 had no impact on ciliogenesis in control cells suggesting a specific rescue of cilia defects in MiniBAR-depleted cells rather than a general promotion of ciliogenesis.

We conclude that MiniBAR limits the $RhoA^{GTP}$ /$Rac1^{GTP}$ balance, thus the cellular acto-Myosin II-dependent contractility, which in turn favors normal ciliogenesis. Mechanistically,

the ciliogenesis defects observed after MiniBAR depletion could be explained by a combined increase in cell contractility and defective trafficking or translocation of key cargos to cilia.

MiniBAR depletion leads to dysfunctional cilia and hallmarks of ciliopathy *in vivo*

To investigate whether MiniBAR could play a role in ciliogenesis *in vivo*, we studied MiniBAR function during zebrafish embryogenesis. We identified a unique and highly conserved MiniBAR homologue in zebrafish (si:ch211-79l17.1 or Garre1) (**Figure S1A**). *In situ* hybridization showed that *minibar* mRNA was maternally expressed, then not detectable during gastrulation, and ubiquitously expressed at the 10-somite stage and 24 hpf (**Figure S7A**). Injection of antisense morpholinos (MO) targeting *minibar* mRNA at the 1-cell stage efficiently reduced MiniBAR expression at 24 hpf (**Figure 6A**) and resulted in multiple developmental defects characteristic of cilium dysfunction. Indeed, *minibar* morphants displayed a curved axis (**Figure 6B**), cystic kidneys (**Figure 6C**) and supra-numerous otoliths in the otic vesicles (**Figure 6D**). In addition, MiniBAR depletion resulted in left-right (L/R) asymmetry defects visible on heart jogging (**Figure 6E**) and pancreas positioning (**Figure S7B**). To further determine the role of MiniBAR in the establishment of L/R asymmetry, we analyzed the cascade of genes expressed asymmetrically in the left lateral plate mesoderm. In *minibar* morphants, the expression of the nodal related gene *southpaw* (*spaw*) and its downstream target *pitx2* are altered, with higher frequency of embryos presenting bilateral, right or absent expression compared to control embryos (**Figure 6F and Figure S7C**). The striking heart L/R asymmetry defects were confirmed with a second, independent MO (MO minibar #2) and rescue experiments (**Figure S7D**). Long-term depletion of MiniBAR using maternal zygotic *minibar* $^{-/-}$ mutants led to the disappearance of full-length MiniBAR, as expected (**Figure S7E-F**), but we did not detect L/R patterning defects. This difference in phenotype between morphants and mutants could be due to a genetic compensation, a process described with several zebrafish mutants[52]. Nonetheless, CRISPR/Cas13d-mediated transient down-regulation[53] of MiniBAR after co-injection of specific *minibar* gRNAs and Cas13d at the 1-cell stage, resulted in MiniBAR knock-down and heart jogging defects 24 hours later, similar to those observed upon MO injection (**Figure S7G**).

L/R asymmetry patterning requires a break in symmetry that occurs in the zebrafish L/R organizer, the Kupffer's vesicle (KV). Within the KV, cilia rotate and create a fluid flow that is critical to establish laterality[2]. Cilia of the KV were shorter in *minibar* morphants compared

to control embryos (**Figure 6G**), while the number of ciliated cells per KV was unchanged (**Figure S7H**). The reduction in cilia length upon MiniBAR depletion was confirmed using CRISPR/Cas13d (**Figure S7G**). Using a two-photon microscope at a scanning speed lower than the cilia beat frequency and transgenic embryos[54], we quantified a higher proportion of immobile cilia in the KV of *minibar* morphants, compared to control embryos (**Figure 6H and Figure S7I**). Furthermore, motile cilia displayed an abnormal beating pattern with a smaller angle of beating upon MiniBAR depletion (**Figure 6I**). All defects observed upon MiniBAR depletion were partially rescued by co-injecting morpholino resistant *miniBAR* mRNA with the minibar MO (**Figure 6B-E, G-I and S7I**).

Collectively, these results demonstrate a role of MiniBAR in cilia elongation in zebrafish, as seen in human RPE-1 cells. The importance of MiniBAR for normal cilia length and beating in the KV likely explains its requirement for the establishment of the L/R axis during zebrafish development. In addition, MiniBAR depletion leads to other characteristic defects observed upon inactivation of genes involved in ciliopathies.

DISCUSSION

Here, we report a conserved function in ciliogenesis of MiniBAR, a dual Rac/Rab effector with a truncated BAR domain that controls both actin cytoskeleton contractility and membrane trafficking for cilia elongation.

MiniBAR, the only known dual Rab/Rac effector with a truncated BAR domain

MiniBAR is one of the few reported dual Rac/Rab effectors. Other examples are Nischarin and OCRL1 which were shown to interact with Rac1 and multiple Rab GTPases[55,56]. In contrast, among all Rab GTPases tested, MiniBAR only interacts with active Rab35 (**Figure S1B**), suggesting that it is a specific Rab35 effector whereas most characterized Rab effectors interact with multiple Rab GTPases[10]. Our biochemical data show that Rab35 and Rac1 can bind simultaneously to two separate domains of MiniBAR. The Rac1 binding domain overlaps with the domain of unknown function DUF4745 and forms a truncated BAR domain, which is not previously described in any other proteins. Furthermore, the Rab35BD central subdomain bears no similarity to other structurally resolved Rab effectors. Interestingly, the truncated BAR domain can be found across evolution in all Bilateria metazoa, i.e. in both Protostomia (such as Arthropods, Mollusks, Annelids, Worms) and Deuterostomia (such as Chordates including Vertebrates and Echinoderms) (**Figure S3A-C**). Furthermore, the DUF4745 (with putative Rac1BD) followed by the Rab35BD is a very ancient innovation and was likely present in the metazoa ancestor, which is known to have both Rho- and Rab-family proteins (**Figure S3D**).

MiniBAR is present on intracellular vesicles and exhibit pulses along cilia

MiniBAR partially colocalizes with both Rac1 and Rab35 at the plasma membrane and on dynamic intracellular vesicles (**Figure 2A-B, 3C-F**). MiniBAR crucially depends on its interaction with Rab35 to localize on vesicles (**Figure 2G**) and the co-overexpression of Rac1 and Rab35 induces the formation of intracellular MiniBAR tubules (**Figure 2D**), suggesting that both GTPases regulate MiniBAR function on membranes. Altogether, MiniBAR is a component of the Rab35 endocytic recycling pathway.

In addition to be transported on vesicles, MiniBAR and Rab35 exhibit striking, fast (15-30 seconds) pulses along cilia present 4-8 hours after serum starvation (**Figure 3G,J**).

Mechanistically, Rab35 pulses drive MiniBAR pulses (**Figure 3H**). To our knowledge, Rab35 and MiniBAR are the first membrane-associated proteins shown to pulse at the ciliary membrane. This raises two interesting questions that will require future investigations. First, how does Rab35/MiniBAR accumulate quickly and transiently at the membrane of cilia? The only case of transient accumulation of proteins in cilia that we are aware of has recently been described for the microtubule-associated kinesin KIF13b and is closely coordinated with IFTs, although the exact mechanism of transient accumulation is not yet understood[57]. Of note, MiniBAR signals spread from either tip to base (**Movie 4,** time 98 s), center to both base and tip (**Movie 4**, time 180 s) or base to tip (**Movie 5**, time 100 s). An interesting possibility is that a soluble pool[58] of GDP-Rab35 is locally activated within cilia and thereby concentrates at the ciliary membrane, where it recruits MiniBAR. We cannot exclude that Rab35/MiniBAR complexes may pulse at the surface of intracellular ciliary vesicles, but we consider this unlikely since at 4-8 hours post-starvation cilia were all (n = 25/ 25) labelled within 2-5 minutes upon addition of CellBrite® (a fluorescent lipid that integrates the plasma membrane and that shows no sign of internalization at this time scale). Interestingly, intraciliary pulses of Ca^{2+} have been reported in the mouse node and the zebrafish KV[59,60], with similar frequency in mouse embryos (1 spike per minute) and contribute to L/R asymmetry establishment *in vivo*[60]. Ca^{2+} pulses might control Rab35 GEF/GAP activities and consequently MiniBAR pulses. A second question raised by our observations is the physiological relevance of MiniBAR pulses. Since MiniBAR pulses are observed during early phases of ciliogenesis (4-16 hours) when cilia continuously elongate, one can speculate that pulses might help to deliver specific cargos necessary for cilia elongation. A non-mutually exclusive possibility is that MiniBAR pulses periodically change the cilia composition independently of cilia growth, especially after 24 hours post-starvation, since a lower but significant proportion of cells still display pulses whereas cilia elongation has stopped.

MiniBAR promotes cilia elongation by controlling membrane trafficking of key cilia proteins and by limiting acto-Myosin II-dependent contractility

Both in human RPE-1 cells and in the KV cells in zebrafish embryos, MiniBAR depletion leads to abnormally short cilia (**Figure 4C, 6G**) indicating that MiniBAR is a limiting factor for cilia growth. Point mutations that selectively disrupt either the binding with active Rac1 or with active Rab35 demonstrate that the interaction with each GTPase is required for normal

ciliogenesis (**Figure 4D-E**). Mechanistically, our data indicate that MiniBAR promotes ciliogenesis by controlling two pathways (**Figure 7**).

First, MiniBAR helps to deliver at least two proteins important for ciliogenesis within cilia: ARL13B and IFT88 (**Figure 7**, right panel). ARL13B is known to promote cilia elongation[43-46] but how it is targeted to the cilia is not well understood. We found that a pool of ARL13B is actively trafficked toward the ciliary base on dynamic MiniBAR vesicles (**Figures 3B-F and 4H**). Importantly, the accumulation of ARL13B within cilia depends on MiniBAR and on its interaction with Rab35 (**Figure 3G,H**). Of note, Rab35 likely plays multiple roles in ARL13B trafficking in and out of cilia, since Rab35 restricts ciliary accumulation of ARL13B[29]. This suggests that Rab35/MiniBAR promotes ARL13B delivery in cilia, while another Rab35 effector that remains to be identified controls the exit of ARL13B from cilia. A strength of our study is to unveil the specific role of Rab35 with MiniBAR, thanks to the crystal structure-guided design of a point MiniBAR mutant that selectively abolishes the interaction with Rab35, thus leaving untouched the interaction of Rab35 with its other effectors. The localization within cilia of the anterograde IFT component IFT88 is also perturbed in MiniBAR-depleted cells and our data suggest that MiniBAR and its interaction with Rab35 promotes the translocation of IFT88 into cilia (**Figure 4I-J**). Altogether, the Rab35/MiniBAR trafficking pathway helps to deliver two limiting factors for cilia growth, which can explain MiniBAR's requirement for cilia elongation.

Besides regulating trafficking, MiniBAR limits acto-Myosin II-dependent contractility (**Figure 5A-C and Figure 7**, right panel), which in turn favors cilia elongation (**Figure 5E**). The regulation of acto-Myosin II-dependent contractility likely involves the pool of MiniBAR at the plasma membrane (**Figure 2A-B**) rather than on internal vesicles. However, how MiniBAR controls the Rho^{GTP}/Rac^{GTP} balance is unknown. MiniBAR has no predicted RhoGAP or RacGAP domains but could regulate Rho^{GTP}/Rac^{GTP} directly —perhaps by protecting bound Rac1-GTP from endogenous GAPs, or indirectly —together with yet to be discovered partners. Interestingly, the fact that reducing Myosin II activity largely but not fully rescues cilia length suggests that MiniBAR controls both pathways —trafficking and contractility. It should be noted that increased levels of stress fibers and hyperactivation of RhoA have been also observed upon mutation/inactivation of different genes involved in ciliopathies[18,19]. Furthermore, ROCK inhibition can rescue ciliary defects in several ciliopathy models including Bardet-Biedl syndrome and polycystic-kidney disease models[25,61-64], as observed upon MiniBAR depletion.

While it is well established that membrane traffic and cell contractility contribute to ciliogenesis, little is known about proteins that regulate both. It was nevertheless recently reported that i) Rab19 helps to clear the actin cortex at the ciliary base —through unknown mechanisms— and promote cilia formation[65] and ii) the depletion of the dual Rab10/RhoA GEF DENN2B increases the number of ciliated cells and cilia length[66] —the opposite of what was observed upon MiniBAR depletion. Thus, there is increasing evidence that cell contractility and membrane traffic are intimately linked and must be tightly regulated during ciliogenesis. We propose that MiniBAR helps to coordinate these two processes to control cilia elongation.

MiniBAR controls cilia length and L/R asymmetry *in vivo*

MiniBAR-depleted zebrafish embryos display several typical defects associated with ciliopathies, such as cystic kidneys and *situs inversus*, likely due to shorter/defective cilia both in the KV and in other locations (**Figure 6A-F and S7A-B**). Both Rac1 and Rab35 GTPases were independently shown to promote ciliogenesis and their disruption also leads to L/R asymmetry defects in zebrafish, but direct effectors are yet to be discovered[3,29,67,68]. MiniBAR might thus represent a missing link between these two GTPases. Our *in vivo* data raises the possibility that genetic ciliopathies of unknown origin in Humans might originate from mutations in MiniBAR.

MiniBAR is likely important also in non-ciliated cells since dynamic MiniBAR-positive vesicles are found in proliferating cells (**Figure 2**). Interestingly, the three mutations shown to disrupt the interaction between MiniBAR and Rac1, A140V, 140T and M144K (**Figure S5A**) are somatic mutations found in cancer biopsies of endometrioid carcinoma, B cell lymphoma, lung squamous cell carcinoma and intestinal adenocarcinoma —in which inactivating RhoA mutations are often observed[69,70]. Thus, MiniBAR may represent a key integrator of Rac/Rab signaling that controls trafficking and the acto-myosin cytoskeleton in ciliogenesis and beyond, notably in pathological situations such as tumorigenesis.

Limitations of the study

While this study demonstrates a role of MiniBAR in ciliogenesis, we acknowledge several limitations. First, the function of the C-terminal part of MiniBAR has not been addressed. Second, the significance of Rab35/MiniBAR pulses and the existence of such pulses in vivo are

important questions for the future. Third, how MiniBAR controls the RhoA/Rac1 balance, potentially via additional interactors, will need further investigation. Finally, the conclusion that MiniBAR limits Myosin II contractility in ciliated cells remains to be confirmed *in vivo*.

ACKNOWLEDGMENTS

We thank Philippe Bastin, Patricia Bassereau, Renata Basto, Alexandre Benmerah, Antoine Jégou and members of our Labs for critical reading, discussions and suggestions; Chantal Desdouets for antibodies, Alexandre Benmerah for plasmids and antibodies, Claire Wyart for the Tg(actb2:Mmu.Arl13b-GFP) line, Marion Delous for the Tg(wt1b:gfp) line, Christine Vesque for the *spaw* and *pitx2* probes, Jean-Paul Concordet for the Cas13d protein, Bruno Goud and Stéphanie Miserey-Lenkei for the Yeast 2-hybrid Rab GTPase library, and Olivier Danot for GST protein. We thank Chiara Zurzolo and Inés Saenz-de-Santa-Maria for commissioning the moving kymograph tool, Pierre Lafaye from the Antibody Engineering platform, Institut Pasteur for initial immunization experiments, Pierre-Henri Commere from Cytometry and Biomarkers UTechS, Institut Pasteur for FACS sorting, Willy Supatto for the help with cilia motility imaging, Emilie Menant for fish care, P. Mahou and the Polytechnique Bioimaging Facility for imaging on their equipment supported by Région Ile-de-France (interDIM) and Agence Nationale de la Recherche (ANR-11-EQPX-0029 Morphoscope2, ANR-10-INBS-04 France BioImaging). UTechS PBI is part of the France–BioImaging infrastructure network (FBI) supported by the French National Research Agency (ANR-10-INBS-04; Investments for the Future), and acknowledges support from ANR/FBI and the Région Ile-de-France (program “Domaine d’Intérêt Majeur-Malinf”) for the use of the Zeiss LSM 780 Elyra PS1 microscope. We acknowledge SOLEIL for provision of synchrotron radiation facilities, and we would like to thank Pierre Legrand for assistance in using the "Proxima-1" beamline and for outstanding help in data processing and structure determination; William Shepard, Martin Savko, Serena Sirigu for assistance in using the "Proxima-2" beamline; Aurelien Thureau for assistance in using the "SWING" beamline and approval of data analysis. We thank Carlos Kikuti and Cecile Boutonnet for help and support in the SEC-MALS experiments, the IBENS platform for access to MicroCal-iTC200 instrument and David Stroebel for assistance in ITC data collection and processing. The *Structural Motility* Team is part of the Labex «Cell(n)Scale» with the references ANR-10-LABX-0038 and ANR-10-IDEX-0001-02. HH has been awarded a doctoral fellowship from the PSL Université. SE was supported by the European Union's Horizon 2020 programme under the Marie Skłodowska-Curie grant agreement No 840201. RS received a fellowship from Association de Recherche sur le Cancer ARC PDF20171206712. This work has been supported by the Institut Pasteur, the CNRS, ANR 18-CE13-0024, ANR 19-CE13-0018 and Fondation pour le Recherche Médicale: Recherche soutenue par la FRM EQU202103012627 to AE, ANR 18-CE13-0024 and ANR 20-CE13-0016 to ND, ANR 18-CE13-0024, INCa 2014-1-PL BIO-04-ICR-1, FRM ING20140129255 to AH and ANR-20-CE18-0016-02 to OP.

AUTHOR CONTRIBUTIONS

RS and MS performed experimental work in human and yeast cells (Figures 1B, 1D, 2, 3, 4, 5, S1B, S4, S5 and S6) with the technical help of FC, MR and NS. AS and RS did the SIM experiments (Figure 3A). QV and ANG constructed plasmids and obtained preliminary results. IC predicted the "MiniBAR" domain and did the evolutionary analysis and alignments (Figure S3). HH, YS, GM, LV, FC, OP performed experimental work on recombinant protein production and characterization; HH, OP performed structural characterization, binding assays, mutational analysis and analyzed the data (Figures 1C, 1E-G, 2E-F, S1C-F, S2B-E). SE conceived and performed experimental work in zebrafish (Figures 6 and S7). EF supervised 2-hybrid screens. RS, MS and AE designed the experiments in human and yeast cells. OP, AH designed experiments on structural characterization and *in vitro* binding assays. SE and ND designed the experiments in zebrafish. AE, OP, AH and ND secured funding and supervised the work. AE, MS, OP, AH, SE and ND wrote the manuscript.

DECLARATION OF INTERESTS

The authors declare no competing interest.

INCLUSION AND DIVERSITY

We support inclusive, diverse, and equitable conduct of research.

STAR METHODS

KEY RESOURCES TABLE

REAGENT or RESOURCE	SOURCE	IDENTIFIER
Antibodies		
Mouse anti-γ-Tubulin (IF: 1:1000, Methanol fixation in Figure 3B, 4C,I and 1:200, PFA fixation in Figure 3A, 4F, 5E)	Sigma	*Cat#T6557; RRID:AB_477584*
Human anti-Acetylated-Tubulin (IF: 1:200, PFA fixation in Figure 3A, 4F, 5E and methanol fixation in Figure 4C,I)	Institut Curie: Therapeutic recombinant antibodies platform	clone C3B9-hFc
Rabbit anti-pMRLC (IF: 1:100, PFA fixation)	Cell signaling	*Cat#3671; RRID:AB_330248*
Rabbit anti-ARL13B (IF: 1:200, PFA fixation)	Proteintech	*Cat#17711-1-AP; RRID:AB_2060867*
Rabbit anti-IFT88 (IF: 1:50, methanol fixation)	kind gift of C. Desdouets (Centre de Recherche des Cordeliers, INSERM, Paris, France) Robert et al.[71]	N.A.
Rabbit anti-DCP1 (IF: 1:200, PFA fixation)	Abnova	*Cat#55802; RRID:AB_529773*
Rabbit anti-GW182 (IF: 1:200, PFA fixation)	Abcam	*Cat#ab70522; RRID:AB_1310295*
Rabbit anti-MiniBAR (WB:1/500; IF: 1:1000, methanol fixation)	This paper	
Mouse anti-FLAG (WB:1/1000)	Sigma-Aldrich	*Cat#F1804; RRID:AB_262044*
Rabbit anti-FLAG (WB:1/1000)	Cell signaling	*Cat#14793; RRID:AB_2572291*
Mouse anti-GAPDH (WB:1/40000)	Proteintech	*Cat#60004-1-Ig; RRID:AB_2107436*
Mouse anti-RhoA (WB:1/500)	Cytoskeleton	*Cat#ARH05; RRID:AB_2884965*
Mouse anti-Rac1 (WB:1/500)	Cytoskeleton	*Cat#ARC03; RRID:AB_10709099*
Mouse anti-β-Tubulin (WB:1/5000)	Sigma-Aldrich	*Cat#T4026; RRID:AB_477577*

Rabbit anti-Rab35 (WB:1/1000)	Proteintech	*Cat#11329-2-AP; RRID:AB_2238179*
acetylated-Tubulin (IF: 1/500)	Sigma-Aldrich	*Cat#T6793; RRID:AB_477585*
ZO-1 (IF: 1/250)	Invitrogen	Cat#33-9100; RRID:AB_2533147
anti-mouse IgG2b Alexa Fluor 488 (IF: 1/500)	Invitrogen	Cat#A21141; RRID: AB_2535778
anti-mouse IgG1 Alexa Fluor 594 (IF: 1/500)	Invitrogen	Cat#A21125; RRID: AB_2535767
Donkey anti-mouse IgG AlexaFluor488 (IF: 1/500)	Jackson ImmunoResearch	*Cat#715-546-151; RRID:AB_2340850*
Donkey anti-mouse IgG CY3 (IF: 1/500)	Jackson ImmunoResearch	*Cat#715-165-151; RRID:AB_2315777*
Donkey anti-mouse IgG Alexa647 (IF: 1/500)	Jackson ImmunoResearch	*Cat#715-605-151; RRID:AB_2340863*
Donkey anti-mouse IgG AlexaFluor488 (IF: 1/500)	Jackson ImmunoResearch	*Cat#711-546-152; RRID:AB_2340619*
Donkey anti-rabbit IgG CY3 (IF: 1/500)	Jackson ImmunoResearch	*Cat#711-165-152; RRID:AB_2307443*
Donkey anti-rabbit IgG Alexa 647 (IF: 1/500)	Jackson ImmunoResearch	*Cat#711-605-152; RRID:AB_2492288*
Donkey anti-Human IgG AlexaFluor488 (IF: 1/500)	Jackson ImmunoResearch	*Cat#709-546-149; RRID:AB_2340569*
Donkey anti-Human IgG CY3 (IF: 1/500)	Jackson ImmunoResearch	*Cat#709-165-149; RRID:AB_2340535*
Donkey anti-Human IgG CY5 (IF: 1/500)	Jackson ImmunoResearch	*Cat#709-175-149; RRID:AB_2340539*
Donkey anti-mouse IgG HRP (WB: 1/10 000)	Jackson ImmunoResearch	*Cat#715-035-151; RRID:AB_2340771*
Donkey anti-rabbit IgG HRP (WB: 1/10 000)	Jackson ImmunoResearch	*Cat#711-035-152; RRID:AB_10015282*
Bacterial and virus strains		
E. coli DH5α	GIBCO	Cat# 18265017
E.Coli BL21(DE3)Star™	ThermoFisher Scientific	Cat# C601003
BL21(DE3) RIPL	Agilent Technologies	Cat#230280

Chemicals, peptides, and recombinant proteins		
Phalloidin conjugated with Alexa Fluor 568	Life Technology	Cat#A22287
CellBrite® (video: 1/2000)	Biotium	Cat#30107
SiR-Tubulin (video: 1/40 000)	Tebu-bio	Cat# SC002
DAPI	Serva	Cat#18860.01
Mowiol	Calbiochem	Cat#475904
PFA	Electron microscopy sciences	Cat#15714
BSA	Sigma-Aldrich	Cat#A7030
NP-40 / Igepal	Sigma-Aldrich	Cat#CA-630
Triton X-100	Merck	Cat#108643
Tween-20	Sigma-Aldrich	Cat#P1379
4x Laemmli Sample Buffer	biorad	Cat#1610747
anti-Flag M2 affinity beads	Sigma-Aldrich	Cat#A2220
Y27632	Calbiochem	Cat#146986-50-7
FBS	Dutscher	Cat#500105R1
Penicillin/Steptomycin	Gibco	Cat#15140122
DMEM-F12	Gibco	Cat# 31331028
GPPNHP	Jena Bioscience	Cat#NU-401
GDP	Jena Bioscience	Cat#NU-1172
Critical commercial assays		
ExceLenti LTX Lentivirus Packaging Mix	Oxford genetics	Cat# EXL10
X-tremGENE 9	Sigma-Aldrich	Cat#06365809001
RNAi max lipofectamine	Thermo Fisher Scientific	Cat#13778075
4-15 % gradient SDS–PAGE gels	BioRad Laboratories	Cat#4561084
4-12 % gradient SDS–PAGE gels	BioRad Laboratories	Cat#3450124
Pierce ECL western blotting substrate-SuperSignal West Pico PLUS	Thermo Fisher Scientific	Cat#34580
Pierce ECL western blotting substrate-SuperSignal West Dura	Thermo Fisher Scientific	Cat#37071
Pierce ECL western blotting substrate-SuperSignal West femto	Thermo Fisher Scientific	Cat#34094
RhoA and Rac1 Activation Assay Biochem Kit	Cytoskeleton	Cat#BK030
Quickchange	Agilent	Cat#200523
Gateway-BP clonase II enzyme mix	Thermo Fisher Scientific	Cat#10348102
Gateway-LR clonase II enzyme mix	Thermo Fisher Scientific	Cat#10134992
Deposited data		
MiniBAR Rac1-BD	This paper	PDB 8BUY
MiniBAR Rab35-BD	This paper	PDB 8BUX

Experimental models: Cell lines		
Human :HEK293FT	Thermofisher	Cat# R70007
Human : hTERT RPE-1 cells	kind gift of A. Benmerah , Institut Imagine, INSERM, Paris, France	ATCC-CRL-4000™
Human : RPE-1-LAP-GFP	This paper	N.A.
Human : RPE-1-MiniBAR-WT-LAP-GFP	This paper	N.A.
Human : RPE-1-MiniBAR-A140V-LAP-GFP	This paper	N.A.
Human : RPE-1-MiniBAR-A461R-LAP-GFP	This paper	N.A.
Experimental models: Organisms/strains		
Zebrafish : AB	ZIRC	
Zebrafish : Tg(wt1b:EGFP)	Bollig et al.[72]	ZDB-TGCONSTRCT-071127-1
Zebrafish : Tg(actb2:Mmu.Arl13b-GFP)	Borovina et al.[73]	ZDB-TGCONSTRCT-100721-1
Zebrafish : *minibar*^{sa35606}	ZIRC	ZDB-ALT-160601-4006
Oligonucleotides		
Morpholino: minibar MO 5'-GTATTCAATGAGCCCAAGGAGTGTC-3'	Gene Tool LLC Philomath	N.A.
Morpholino: minibar MO #2 5'-TCACCAAGCGGACACCTTTCAATGC-3'	Gene Tool LLC Philomath	N.A.
Morpholino: standard control 5′-CCTCTTACCTCAGTTACAATTTATA-3'	Gene Tool LLC Philomath	N.A.
gRNA Cas13d_minibar_1 5′-ACAGATAGTTTGTGCTTCTGCTAGG TTTCAAACCCCGACCAGTT-3'	This paper	N.A.
gRNA Cas13d_minibar_2 5′-GAGAGGAGCTGCTGAGGTGACGGAGGTTTCAAACCCCGACCAGTT-3'	This paper	N.A.
gRNA Cas13d_minibar_3 5′-GGTGCGAGAGGATTTGCCCATCAGGTTT CAAACCCCGACCAGTT-3'	This paper	N.A.
siRNA targeting luciferase: 5'-CGUACGCGGAAUACUUCGA-3'	This paper	N.A.

siRNA human MiniBAR: 5'-CUGCAAAUUUUACGGAUCA-3'	This paper	N.A.
siRNA human MiniBAR #2: 5'-CCAUAAAGCCUGAGAUCGC-3'	This paper	N.A.
Primer: MiniBAR siRNA resistant 5'-C**A**GC**T**AA**C**TT**C**AC**T**GA**C**CA-3'	This paper	N.A.
Recombinant DNA		
pCS2+-minibar -GFP	This paper	N.A.
pCRII-TOPO-minibar	This paper	N.A.
pET-28b-RfxCas13d-His	kind gift of J.P. Concordet, Sorbonne University, Paris, France	Addgene #141322
pDEST 3xFLAG C1-Rab35-WT,Rab35-Q67L,Rab35-S22N	Cauvin et al.[39]	N.A.
pmCherryFP-Rab35-WT	Klinkert et al.[74]	N.A.
pcDNA FLAG-Rac1-WT,Rac1-T17N,Rac1-Q61L	kind gift of A. Gautreau , Ecole Polytechnique, CNRS, Palaiseau, France	N.A.
peGFP-Rac1-WT	kind gift of A. Gautreau, Ecole Polytechnique, CNRS, Palaiseau, France	N.A.
pcDNAm FRT PC mCherry Rac1-WT, Rac1-Q61L	kind gift of A. Gautreau, Ecole Polytechnique, CNRS, Palaiseau, France	N.A.
pARL13B-mCherryFP	kind gift of A. Benmerah, Institut Imagine, INSERM, Paris, France	N.A.
EGFP-hAgo2	Addgene	#21981
pT7-EGFP-C1-HsDCP1a	Addgene	#25030
pLexA,pGAD constructs	Klinkert et al.[74]	N.A.
pENTR-MiniBAR WT, A140V, A461R-LAP-GFP	This paper	N.A.
pENTR-MiniBAR-WT-LAP-iRFP	This paper	N.A.
pENTR-MiniBAR-WT, A140V, A461RLAP-mCherry	This paper	N.A.
pDEST-MiniBAR WT, A140V, A461R-LAP-GFP	This paper	N.A.

pDEST-MiniBAR-WT, A140V, A461R-LAP-mCherry	This paper	N.A.
pDESTLenti-MiniBAR WT, A140V, A461R-LAP-GFP	This paper	N.A.
Software and algorithms		
Fiji (ImageJ)	ImageJ	https://imagej.nih.gov/ij/
Icy	Icy	http://icy.bioimageanalysis.org/
Graphpad Prism	Graphpad	https://www.graphpad.com/scientific-software/prism/
Metamorph	Molecular Devices	https://www.moleculardevices.com/products/cellular-imaging-systems/acquisition-and-analysis-software/metamorph-microscopy
Biorender	Biorender	https://www.biorender.com/
NEBaseChanger	NEB	https://nebasechanger.neb.com/
XDSme	Pierre Legrand, synchrotron Soleil	https://github.com/legrandp/xdsme
AutoPROC	Global Phasing,	https://www.globalphasing.com/autoproc/
CCP4 program suite (Phaser, Pirate, SHELX, Buccaneer, Coot, Archimboldo)		https://www.ccp4.ac.uk/download/#os=mac
PHENIX		https://phenix-online.org/
BUSTER	Global Phasing	https://www.globalphasing.com/buster/
Adobe Photoshop	Adobe	https://www.adobe.com/
Adobe Illustrator	Adobe	https://www.adobe.com/

RESOURCE AVAILABILITY

Lead contact

Further information and requests for resources and reagents should be directed to and will be fulfilled by the lead contact, Arnaud Echard (arnaud.echard@pasteur.fr).

Materials availability

All unique reagents and plasmids reported in this paper are available from the lead contact upon request.

Data and code availability

The atomic model of the Rac1BD and Rab35BD are available on the PDB under the accession code 8BUY and 8BUX, respectively. This paper does not report original code.

Any additional information required to reanalyze the data reported in this paper is available from the lead contact upon request.

EXPERIMENTAL MODEL AND STUDY PARTICIPANT DETAILS

Cell culture

hTERT RPE-1 cells (hTERT-immortalized retinal pigment epithelial cells) were grown in DMEM-F12 medium supplemented with 10 % fetal bovine serum and 1 % penicillin/streptomycin in 5 % CO2 at 37 °C. For serum starvation experiments, cells were washed twice with DMEM-F12 without serum and incubated with DMEM-F12 without serum.
For experiments with the ROCK inhibitor (Figure 5E), RPE-1 cells transfected with either siRNAs targeting Luciferase or MiniBAR for 72 h were treated with Y27632 at 50 µM for 24 h in DMEM-F12 without serum before fixation.

Stable cell lines

Stable cell lines expressing low levels of siRNA-resistant, -GFP-tagged, full-length MiniBAR^{WT} and mutants (MiniBAR^{A140V} or MiniBAR^{A461R}) were generated by lentiviral transduction in RPE-1 cells. Briefly, lentiviral particles were produced in the HEK293 FT packaging cells transfected with MiniBAR constructs and the Excelenti LTX Lentivirus Packaging mix using lipofectamine following manufacturer's instructions. After 48 h, the HEK293 FT culture supernatants were added to RPE-1 cells for 24 h. A week later, GFP-positive cells were sorted by FACS.

Zebrafish strains

Zebrafish (*Danio rerio*) were housed in 27°C water (pH 7.4 and conductivity 500 µS) with a 13 hr on/11 hr off light cycle. All zebrafish husbandry was performed under standard conditions according to institutional (Institut Polytechnique de Paris) and national (France) ethical and animal welfare regulations. Embryos were obtained by natural spawning of AB, Tg(wt1b:EGFP)[72] , Tg(actb2:Mmu.Arl13b-GFP)[73] and *minibar*^{sa35606} adult fishes. Embryos were incubated at 28°C and staged in hours post-fertilization (hpf) as described[75]. All animal studies were approved by the Ethical Committee N°59 and the Ministère de l'Education Nationale, de l'Enseignement Supérieur et de la Recherche under the file number APAFIS#15859-2018051710341011v3.

METHOD DETAILS

Plasmids

Human MiniBAR cDNA (KIAA0355) was subcloned into Gateway pENTR plasmid and -LAP-GFP, -LAP-mCherry and -iRFP expression vectors were generated by LR recombinaison. Point mutations in MiniBAR have been generated using NEBaseChanger, were amplified by PCR and introduced into pENTR gateway vectors, then recombined into the transient expression vector (-LAP-GFP, -LAP-mCherry, GAD) or lentiviral -GFP destination vector (ThermoFisher scientific). For rescue experiments, siRNA-resistant versions have been obtained by mutating 6 bp of the siRNA-targeting sequence using Quickchange.

Protein expression, purification

The human constructs (Rac1, Rab35, Rac1BD (MiniBAR$^{70-208}$), Rab35BD (MiniBAR$^{225-553}$) and Rac1BD-Rab35BD (MiniBAR$^{70-553}$), were cloned in pPROEX-HTb or pRSFduet plasmids with N-terminal His-tag and rTEV cleavage sites; expressed in *E. coli* BL21(DE3) or BL21(DE3)RIPL cells. The cells were grown in 2xYT media to 0.6 OD600 a 37ºC, induced with 0.2 mM IPTG at grown overnight at 17 °C. The cells were harvested by centrifugation, disrupted by sonication in (50

mM Tris pH8, 150 mM NaCl, 2 mM $MgCl_2$, 1 mM TCEP, 1 mM PMSF, complete protease inhibitor mix (GE Healthcare), 5 % glycerol (v/v), 40 mM imidazole). The cell lysate was applied on Ni-NTA column (GE Healthcare) after clarification by centrifugation. The Ni-NTA column was washed with (50 mM Tris pH8, 150 mM NaCl, 2 mM $MgCl_2$, 1 mM TCEP, 5 % glycerol, 40 mM imidazole) and the protein was eluted with 250mM imidazole. The His-tag was removed by overnight incubation with rTEV protease (1:100 protein:protease ratio). Gel-filtration was performed as a final purification step, using Superdex 200 or Superdex 75 columns (GE Healthcare) in running buffer: 50 mM Tris pH8, 50 mM NaCl2, 2 mM $MgCl_2$, 2 mM TCEP. The proteins were concentrated, flash frozen in liquid nitrogen and stored at -80 ºC.
The active GTP-bound form of Rac1 was produced by introducing Q61L mutation ($Rac1^{Q61L}$). The active form of Rab35 was generated by GPPNHP nucleotide exchange before the final gel-filtration: the purified Rab35 protein was incubated with 10 times molar excess of GPPNHP in 10 mM EDTA containing buffer, the exchange was terminated by adding 20 mM MgCl2. For Rab35-GTP pull down assays, GST-RUSC2 was purified as described in Fukuda et al.[76].

ITC

Isothermal titration calorimetry experiments were carried out on a MicroCal ITC-200 titration microcalorimeter (Malvern) at 10 °C. The protein samples were in 50 mM Tris pH 8, 50 mM NaCl, 2 mM $MgCl_2$, 2 mM TCEP. The titration processes were performed by injecting 2 µL aliquots of protein samples from a syringe (active form of Rac1 or Rab35 at a concentration of 480 µM) into protein samples in cell (MiniBAR fragments at a concentration of 60 µM) at time intervals of 2 min to ensure that the titration peak returned to the baseline. The titration data were analyzed using the instrument producer provided software (Origin7[77]) and fitted by the one-site binding model.

Analytical SEC and SEC-MALS

Absolute molar masses of proteins were determined using size-exclusion chromatography combined with multi-angle light scattering (SEC–MALS). Protein samples (Rac1BD, Rab35BD and Rac1BD-Rab35BD) (40 µL; 10-25 mg/ml) were loaded onto a Superdex-200 increase 10/300 column (GE Healthcare) or BioSec5 300 (Agilent) or XBridge BEH SEC 200 Å (Waters) in 50 mM Tris pH 8.0, 50 mM NaCl, 2 mM $MgCl_2$, 2 mM TCEP, at 0.3-0.5 ml/min flow rate using a Dionex UltiMate 3000 HPLC system. The column output was fed into a DAWN HELEOS II MALS detector (Wyatt Technology). Data were collected and analyzed using ASTRA software (Wyatt Technology). Molecular masses were calculated across eluted protein peaks. The eluted protein peak fractions were collected and analyzed by SDS-PAGE. Analytical SEC was performed using the same setup excluding MALS detector.

Crystallization and X-ray structure determination

Crystals were obtained by the hanging drop vapor diffusion method at 17 °C by mixing of 1 µL of concentrated protein solution with 1 µL of crystallization solution. Initial crystals were improved by microseeding.
Crystals of the selenomethionine substituted Rab35BD were grown with 1.26 M Sodium Malonate pH 6.3, 5 % (v/v) glycerol, 5% ethylene glycol, 10 mM DTT. The crystals were cryoprotected using the crystallization solution with increased Sodium Malonate concentration to 3M before flash freezing in liquid nitrogen. A single-wavelength anomalous diffraction dataset was collected at the SOLEIL synchrotron Proxima-1 beamline, processed with XDSME package[78] and phased using SHELX program suite[79]. The phases were improved

using Phaser[80] with subsequent density modification using Pirate[81]. The initial protein model was built with Buccaneer[82] and refined with BUSTER[83]. After iterative rebuilding in COOT[84] and refinement with PHENIX[85] using the data set reprocessed with AutoPROC[86,87] the final model (Suppl. Table 1) was deposited to the Protein Data Bank (PDB).
Rac1BD was crystallized in 100mM Ammonium Citrate dibasic, 16 % (w/v) PEG 3350, The crystals were cryoprotected by supplementing the crystallization solution with 22 % (v/v) ethylene glycol. A native data set was collected at the SOLEIL synchrotron Proxima-2 beamline. The data set was processed with AutoPROC[86] and the structure was determined by molecular replacement using Archimboldo program[88] from CCP4 program sute[87], model rebuilding was performed using COOT[84] and refinement -using PHENIX[85], the final structure (Suppl. Table 1) was deposited to the PDB.

Small angle X-ray scattering (SAXS)

SAXS data collection were performed at SOLEIL synchrotron SWING beamline (Suppl. Table 1), the samples were subjected to on-line size exclusion purification with the HPLC system connected to a quartz capillary placed under a vacuum cell[85]. Data reduction, averaging of identical frames corresponding to the elution peak and buffer subtraction were performed with the SWING in-house software Foxtrot. The radius of gyration (R_g) and forward intensity at zero angle I(0) were derived by the Guinier approximation using the software PRIMUS[89]. The maximum dimension (Dmax) and the Rg were derived from the pair distribution function P(r), calculated with the software GNOM[90]. The molecular weight was calculated with the PRIMUS Molecular Weight wizard[89]. The MultiFoXS web-server[91] was used to fit the theoretical scattering intensity from the X-ray structure into the experimental SAXS data (Suppl. Table 1); side chains and loops missing in the X-ray structures were modelled using Modeller[92] before the fitting.

Yeast two hybrid assays and screens

A placenta random-primed cDNA library was screened by Hybrigenics Services SAS using human LexA-Rab35^{Q67L} (aa 1-194, to delete the terminal prenylated cysteines) as a bait in the presence of 2 mM 3-aminoTriazole. 26 out of 227 isolated clones from 108 million screened interactions encoded part of KIAA0355. The same library was screened with human LexA-Rac1$^{G12V,\ C189S}$ (active Rac1 with mutated terminal prenylated cysteine). 336 clones were selected from 60 million interactions tested, of which 10 encoded for KIAA0355 fragments. Furthermore, 8 clones encoding for KIAA0355 fragments were also isolated using a Rac1^{G12V,C189S}- LexA fusion as a bait, from 53 million interactions tested and a total of 153 selected clones. No 3-aminotriazole was used in the Rac1 screens.
Yeast two-hybrid experiments were performed by co-transforming the Saccharomyces cerevisiae reporter strain L40 with either pGAD-MiniBAR full length, MiniBAR Rac1BD, or MiniBAR Rab35BD together with either pLex-human Rab35^{WT}, pLex-human Rab35^{Q67L}, pLex-human Rab35^{S22N}, or pLex-human Rac1^{WT}, pLex-human Rac1^{Q61L}, pLex-human Rac1^{T17N}. Transformed yeast colonies were selected on DOB agarose plates without Tryptophane and Leucine. Colonies were picked and grown on DOB agar plates with Histidine to select co-transformants and without Histidine to detect interactions, as described in Fremont et al.[93].

Human cell transfection and RNA interference

Plasmids were transfected in RPE-1 cells for 24 h (Figure 2B,C ; Figure 3D,F,J) or 48 h (for Figure 4H) using X-tremeGENE 9 DNA reagent following the manufacturer's instructions.

For Rab35 silencing experiment, MiniBAR-GFP stable cell line was transfected with 25 nM of siRNAs targeting luciferase or human Rab35[34] using Lipofectamine RNAiMAX, following the manufacturer's instructions. Time lapse microscopy after siRNA Rab35 (Figure 3H) were started 72 h after siRNA transfection.
For MiniBAR silencing experiments, RPE-1 cells or MiniBAR-GFP stable cell lines were transfected with 25 nM of siRNAs targeting either luciferase or human MiniBAR using Lipofectamine RNAiMAX, following the manufacturer's instructions. For MiniBAR siRNA experiments with serum removal (Figure 4A-J, 5A-E, S6D,E,G and S6I-J), the serum was removed to induce ciliogenesis for 48 h after 24 h of siRNA transfection. In Figure S6F-G and S6I-J, we used a second independent siRNA targeting MiniBAR (siRNA MiniBAR #2).

Western blots

RPE-1 cells transfected with siRNAs were lysed in cell lysis buffer (cytoskeleton, Part #CLB01) supplemented with protease inhibitors. 30 µg of lysate was migrated in 4-15 % gradient SDS–PAGE gels, transferred onto PVDF membranes (Millipore) and incubated with indicated primary antibodies in TBS, 5 % low-fat milk and 0.1 % Tween20. The membranes were incubated with HRP-coupled secondary antibodies and revealed by chemiluminescence.
MiniBAR-GFP stable cell lines transfected with siRNAs were directly collected in 1x loading buffer, boiled 5 min and 10 µL of total extracts were migrated in SDS-PAGE.
3 to 5 zebrafish embryos were directly collected in 1x loading buffer, boiled 5 min and 1/4 of the total extracts was migrated in SDS-PAGE.

Pull down assays

$RhoA^{GTP}$ and $Rac1^{GTP}$ pull down assays were performed using the RhoA and Rac1 Activation Assay Biochem Kit according to the manufacturer's instructions. Rab35 GTP pull down assays were performed as described in references[50,76].

Co-immunoprecipitation assays

RPE-1 cells were transfected with the different Flag constructs for 48 h using X-tremeGENE 9 DNA reagent. Cells were lysed in 20 mM Tris (pH 7.4), 100 mM KCl, 2 mM $MgCl_2$ and 0.1 % NP-40 for Rab35 coIPs and in 30 mM Tris (pH 7.4), 150 mM NaCl, 5 mM $MgCl_2$ and 0.1 % NP-40 for Rac1 coIPs. Supernatants (10 min at 20 000*g*) were incubated with anti-Flag M2 affinity beads for 3 h, washed with lysis buffer and resuspended into 1 × Laemmli buffer and boiled at 95 °C for 5 min. The amount of co-immunoprecipitated MiniBAR endogenous protein in each condition was probed by western blot using anti-MiniBAR antibodies.

Immunofluorescence in human cells and image acquisition

Cells were grown on coverslips and then fixed with 4 % paraformaldehyde (PFA) for 15 min at room temperature or with ice-cold methanol for 3 min at -20 °C depending on the antibodies (see Key ressources table section). For ciliogenesis induction, the serum was removed 48 h before fixation. For ARL13B and IFT88, cells were permeabilized after fixation with 0.1 % Triton-X100 for 3 min, blocked with 0.2 % BSA/PBS for 30 min and successively incubated for 1 h at room temperature with primary and secondary antibodies diluted in PBS containing 0.2 % BSA. For phospho-Myosin II and phalloidin staining, cells were fixed with 4 % paraformaldehyde (PFA) in cytoskeleton buffer (10 mM MES, 138 mM KCl, 3 mM $MgCl_2$, 2 mM EGTA supplemented with sucrose) permeabilized with 0.1 % Triton-X100 for 5 min and incubated with primary antibodies and phalloidin (1:200) overnight in cytoskeleton buffer

containing 0.2 % BSA. For MiniBAR staining, cells were permeabilized and saturated with 0.2 % BSA/PBS/saponin 0.1 % for 30 min, then incubated with primary and secondary antibodies diluted in 0.2 % BSA/PBS/saponin 0.1%. Cells were mounted in Mowiol after DAPI staining (0.5 µg /mL).
Images in Figure 2G, 3B and 5A-B were acquired with an inverted TiE Nikon microscope, using a x100 1.4 NA PL-APO objective lens or a x60 1.4 NA PL-APO VC objective lens and MetaMorph software (MDS) driving a CCD camera (Photometrics Coolsnap HQ). For co-transfected cells (Figure2G), cells were fixed 24 h after transfection and directly mounted in Mowiol.
Images in Figure 4C, 4F, 4I and 5E were acquired using an inverted Nikon Eclipse Ti-E microscope equipped with a CSU-X1 spinning disk confocal scanning unit (Yokogawa) and with an electron-multiplying CCD (EMCCD) camera (Evolve 512 Delta, Photometrics) or a Prime 95S sCMOS camera (Teledyne Photometrics).

Structured Illumination Microscopy (SIM)

SIM was performed on a Zeiss LSM 780 Elyra PS1 microscope (Carl Zeiss, Germany) using C Plan-Apochromat 63×/1.4 oil objective with a 1.518 refractive index oil (Carl Zeiss). The fluorescence signal was detected on an EMCCD Andor Ixon 887 1K. Raw images were composed of fifteen images per plane per channel (five phases, three angles), and acquired with a Z-distance of 110 nm. The SIMcheck plugin[94] in ImageJ was used to analyze the quality of the acquisition and the processing in order to optimize parameters for resolution, signal-to-noise ratio, and reconstruction pattern.

Time-lapse microscopy in human cells

For spinning disk confocal experiments, RPE-1 cells or MiniBAR-GFP stable cell lines were plated on 35 mm glass bottom plates (MatTek). For transfection experiments, cells were imaged 24 h (Figure 2B-C and 3D,F,J) or 48 h after transfection (Figure 4H). For serum starvation experiment, serum was removed 3-4 h before imaging and SiR-Tubulin was added at the same time and kept during the time of the movie for 2-4 h. Cells were incubated in an open chamber (Life Imaging) equilibrated with 5 % CO2 and maintained at 37 °C. Images were acquired using an inverted Nikon Eclipse Ti-E microscope equipped with a CSU-X1 spinning disk confocal scanning unit (Yokogawa) and with an electron-multiplying CCD (EMCCD) camera (Evolve 512 Delta,Photometrics) or a Prime 95S sCMOS camera (Teledyne Photometrics).

Imaging of zebrafish embryos

Imaging of Kupffer's vesicle and kidney was done on an inverted TCS SP8 confocal microscope (Leica) using a High NA oil immersion objective (HC PL APO 63x 1.40, Leica). Whole-mount immunostained KV were dissected and mounted on a slide. Imaging of Kupffer's vesicle for cilia motility quantification was done under an upright TriM Scope II (La Vision Biotech) two-photon microscope equipped with an environmental chamber (okolab) at 28 °C. Injected embryos were mounted at 8- somite in 0.2 % agarose in embryo medium.
Whole embryo imaging was performed with a M205FCA stereomicroscope (Leica) and a MC170HD Camera (Leica).

Whole-mount In Situ Hybridization in zebrafish embryos

Zebrafish embryos were fixed in 4 % paraformaldehyde at 4 °C for 48 hpf. Whole-mount *in situ* hybridisations were performed as previously described[95] using *spaw*, *ptx2, nkx2.5*, *insulin*, and *minibar* probe.

Whole-mount immunostaining in zebrafish embryos

Embryos from 8 to 10-somite stage were fixed with 4 % paraformaldehyde overnight at 4 °C. Embryos were washed with PBDT (PBS 1x, BSA 1 %, DMSO 1 %, and Triton X-100 0.3 %) and blocked for 1-2 hours in blocking buffer (PBDT and 0.5 % goat serum). Primary antibodies were diluted in blocking buffer and incubated overnight at 4 °C. Embryos were rinsed several times with PBDT and incubated with secondary antibodies for 4 h at room temperature. Embryos were rinsed in PBDT and mounted in 50 % Glycerol/PBS.

Zebrafish injection

Translation blocking morpholinos (Gene Tool LLC Philomath) were injected in 1-cell stage embryos with 2 nl of injection volume and 0.5 mM concentration.
For rescue experiments, pCS2+-Minbar-GFP plasmid was linearized with NotI and Capped MiniBAR-GFP mRNA was synthetized using mMessage mMachine SP6 kit (Thermo Fischer). MiniBAR-GFP mRNA was injected in 1-cell stage embryos with 2 nl of injection volume and 90 ng/µL.

minibar sa35606 mutant

minibar^{sa35606} mutants carry a point mutation at Chr 18: 369582 location, leading to a premature stop codon. Fishes were genotyped by fin clipping. DNA preparation was performed by placing fin clip in lysis buffer (50 mM KCl, 10 mM Tris pH 8.3, 0.3 % Tween-20, 0.3 % NP-40) with fresh Proteinase K (Merck Cat #03115887001) at 55 °C overnight followed by 15 min of inactivation of proteinase K inactivated at 95 °C. Genotyping was performed by PCR followed by restriction enzyme digestion. The PCR product (218 bp spanning the mutation) was digested with PvuII. Digestion can only occur in WT amplification, leading to a 190 bp fragment in WT and 218 bp in mutants.

CRISPR/Cas13d in zebrafish embryos

Three different guide RNAs targeting minibar were prepared following Kushawah et al. protocol[53]. Targeted sequences can be found in the Key Ressources Table. RfxCas13d protein, purified from bacteria cells transformed with the plasmid pET-28b-RfxCas13d-His.
RfxCas13d purified protein and a mix of 3 guide RNAs targeting minibar were injected in 1-cell stage embryos with 2 nl of injection volume and 600 ng/µL (gRNAs) and 3µg/µL (Cas13d) concentrations. RfxCas13d purified protein was injected alone as a control.

QUANTIFICATION AND STATISTICAL ANALYSIS

Image quantification and kymograph analysis

Quantification of MiniBAR mean intensity around centrosomal area was done manually following MiniBAR staining around γ-Tubulin staining using Fiji. For quantification of total F-actin and mean phospho-Myosin II per cell, cell contours were defined manually.
For analyzing MiniBAR pulses a kymograph must be extracted from end-points that follow the cilium base and tip as they move. To this end we used TrackMate[96] to manually track the cilium base and tip. For each time-point, we then extracted an intensity profile between these two points, averaged over a width of 5 pixels. The intensity profiles are collected for every frame of the movie, following the cilium movement. The profiles are then stacked along time and centered in their middle to generate a kymograph like the one shown in Figure 3G.

Statistics and reproducibility data

All values are displayed as mean ± SD (standard deviation) for at least three independent experiments (as indicated in the figure legends). Significance was calculated using paired two-sided *t*-tests, or one-sided exact Fisher's tests or mixed linear model, as indicated in the figure legends. For comparing distribution, a nonparametric Kolmogorov–Smirnov (KS) test was used. P values are indicated in each individual graph and were rounded to the nearest significant figure. In all statistical tests $P > 0.05$ was considered as non-significant. Quantifications of images and Western blots were done with Fiji.

REFERENCES

1. Anvarian, Z., Mykytyn, K., Mukhopadhyay, S., Pedersen, L.B., and Christensen, S.T. (2019). Cellular signalling by primary cilia in development, organ function and disease. Nature reviews. Nephrology *15*, 199-219. 10.1038/s41581-019-0116-9.
2. Grimes, D.T., and Burdine, R.D. (2017). Left-Right Patterning: Breaking Symmetry to Asymmetric Morphogenesis. Trends Genet *33*, 616-628. 10.1016/j.tig.2017.06.004.
3. Kim, J., Lee, J.E., Heynen-Genel, S., Suyama, E., Ono, K., Lee, K., Ideker, T., Aza-Blanc, P., and Gleeson, J.G. (2010). Functional genomic screen for modulators of ciliogenesis and cilium length. Nature *464*, 1048-1051. nature08895 [pii] 10.1038/nature08895.
4. Wheway, G., Schmidts, M., Mans, D.A., Szymanska, K., Nguyen, T.T., Racher, H., Phelps, I.G., Toedt, G., Kennedy, J., Wunderlich, K.A., et al. (2015). An siRNA-based functional genomics screen for the identification of regulators of ciliogenesis and ciliopathy genes. Nature cell biology *17*, 1074-1087. 10.1038/ncb3201.
5. Reiter, J.F., and Leroux, M.R. (2017). Genes and molecular pathways underpinning ciliopathies. Nature reviews. Molecular cell biology *18*, 533-547. 10.1038/nrm.2017.60.
6. Malicki, J.J., and Johnson, C.A. (2017). The Cilium: Cellular Antenna and Central Processing Unit. Trends in cell biology *27*, 126-140. 10.1016/j.tcb.2016.08.002.
7. Sorokin, S.P. (1968). Reconstructions of centriole formation and ciliogenesis in mammalian lungs. J Cell Sci *3*, 207-230. 10.1242/jcs.3.2.207.
8. Molla-Herman, A., Ghossoub, R., Blisnick, T., Meunier, A., Serres, C., Silbermann, F., Emmerson, C., Romeo, K., Bourdoncle, P., Schmitt, A., et al. (2010). The ciliary pocket: an endocytic membrane domain at the base of primary and motile cilia. J Cell Sci *123*, 1785-1795. 10.1242/jcs.059519.
9. Mul, W., Mitra, A., and Peterman, E.J.G. (2022). Mechanisms of Regulation in Intraflagellar Transport. Cells *11*. 10.3390/cells11172737.
10. Homma, Y., Hiragi, S., and Fukuda, M. (2021). Rab family of small GTPases: an updated view on their regulation and functions. Febs j *288*, 36-55. 10.1111/febs.15453.
11. Blacque, O.E., Scheidel, N., and Kuhns, S. (2018). Rab GTPases in cilium formation and function. Small GTPases *9*, 76-94. 10.1080/21541248.2017.1353847.
12. Nachury, M.V., Loktev, A.V., Zhang, Q., Westlake, C.J., Peranen, J., Merdes, A., Slusarski, D.C., Scheller, R.H., Bazan, J.F., Sheffield, V.C., and Jackson, P.K. (2007). A core complex of BBS proteins cooperates with the GTPase Rab8 to promote ciliary membrane biogenesis. Cell *129*, 1201-1213.
13. Knödler, A., Feng, S., Zhang, J., Zhang, X., Das, A., Peränen, J., and Guo, W. (2010). Coordination of Rab8 and Rab11 in primary ciliogenesis. Proceedings of the National Academy of Sciences of the United States of America *107*, 6346-6351. 10.1073/pnas.1002401107.
14. Westlake, C.J., Baye, L.M., Nachury, M.V., Wright, K.J., Ervin, K.E., Phu, L., Chalouni, C., Beck, J.S., Kirkpatrick, D.S., Slusarski, D.C., et al. (2011). Primary cilia membrane assembly is initiated by Rab11 and transport protein particle II (TRAPPII) complex-dependent trafficking of Rabin8 to the centrosome. Proceedings of the National Academy of Sciences of the United States of America *108*, 2759-2764. 10.1073/pnas.1018823108.

15. Lu, Q., Insinna, C., Ott, C., Stauffer, J., Pintado, P.A., Rahajeng, J., Baxa, U., Walia, V., Cuenca, A., Hwang, Y.S., et al. (2015). Early steps in primary cilium assembly require EHD1/EHD3-dependent ciliary vesicle formation. Nature cell biology *17*, 228-240. 10.1038/ncb3109.
16. Xie, S., Farmer, T., Naslavsky, N., and Caplan, S. (2019). MICAL-L1 coordinates ciliogenesis by recruiting EHD1 to the primary cilium. J Cell Sci *132*. 10.1242/jcs.233973.
17. Wingfield, J.L., Lechtreck, K.F., and Lorentzen, E. (2018). Trafficking of ciliary membrane proteins by the intraflagellar transport/BBSome machinery. Essays Biochem *62*, 753-763. 10.1042/ebc20180030.
18. Smith, C.E.L., Lake, A.V.R., and Johnson, C.A. (2020). Primary Cilia, Ciliogenesis and the Actin Cytoskeleton: A Little Less Resorption, A Little More Actin Please. Front Cell Dev Biol *8*, 622822. 10.3389/fcell.2020.622822.
19. Hoffman, H.K., and Prekeris, R. (2022). Roles of the actin cytoskeleton in ciliogenesis. J Cell Sci *135*. 10.1242/jcs.259030.
20. Wu, C.T., Chen, H.Y., and Tang, T.K. (2018). Myosin-Va is required for preciliary vesicle transportation to the mother centriole during ciliogenesis. Nature cell biology *20*, 175-185. 10.1038/s41556-017-0018-7.
21. Magistrati, E., Maestrini, G., Niño, C.A., Lince-Faria, M., Beznoussenko, G., Mironov, A., Maspero, E., Bettencourt-Dias, M., and Polo, S. (2022). Myosin VI regulates ciliogenesis by promoting the turnover of the centrosomal/satellite protein OFD1. EMBO Rep *23*, e54160. 10.15252/embr.202154160.
22. Nager, A.R., Goldstein, J.S., Herranz-Pérez, V., Portran, D., Ye, F., Garcia-Verdugo, J.M., and Nachury, M.V. (2017). An Actin Network Dispatches Ciliary GPCRs into Extracellular Vesicles to Modulate Signaling. Cell *168*, 252-263.e214. 10.1016/j.cell.2016.11.036.
23. Phua, S.C., Chiba, S., Suzuki, M., Su, E., Roberson, E.C., Pusapati, G.V., Schurmans, S., Setou, M., Rohatgi, R., Reiter, J.F., et al. (2017). Dynamic Remodeling of Membrane Composition Drives Cell Cycle through Primary Cilia Excision. Cell *168*, 264-279.e215. 10.1016/j.cell.2016.12.032.
24. Pitaval, A., Tseng, Q., Bornens, M., and Théry, M. (2010). Cell shape and contractility regulate ciliogenesis in cell cycle-arrested cells. The Journal of cell biology *191*, 303-312. 10.1083/jcb.201004003.
25. Kim, J., Jo, H., Hong, H., Kim, M.H., Kim, J.M., Lee, J.K., Heo, W.D., and Kim, J. (2015). Actin remodelling factors control ciliogenesis by regulating YAP/TAZ activity and vesicle trafficking. Nat Commun *6*, 6781. 10.1038/ncomms7781.
26. Chaineau, M., Ioannou, M.S., and McPherson, P.S. (2013). Rab35: GEFs, GAPs and Effectors. Traffic *14*, 1109-1117. 10.1111/tra.12096.
27. Klinkert, K., and Echard, A. (2016). Rab35 GTPase: a central regulator of phosphoinositides and F-actin in endocytic recycling and beyond. Traffic. 10.1111/tra.12422.
28. Shaughnessy, R., and Echard, A. (2018). Rab35 GTPase and cancer: Linking membrane trafficking to tumorigenesis. Traffic. 10.1111/tra.12546.
29. Kuhns, S., Seixas, C., Pestana, S., Tavares, B., Nogueira, R., Jacinto, R., Ramalho, J.S., Simpson, J.C., Andersen, J.S., Echard, A., et al. (2019). Rab35 controls cilium length, function and membrane composition. EMBO Rep *20*, e47625. 10.15252/embr.201847625.

30. Bagci, H., Sriskandarajah, N., Robert, A., Boulais, J., Elkholi, I.E., Tran, V., Lin, Z.Y., Thibault, M.P., Dubé, N., Faubert, D., et al. (2020). Mapping the proximity interaction network of the Rho-family GTPases reveals signalling pathways and regulatory mechanisms. Nature cell biology *22*, 120-134. 10.1038/s41556-019-0438-7.
31. Carman, P.J., and Dominguez, R. (2018). BAR domain proteins-a linkage between cellular membranes, signaling pathways, and the actin cytoskeleton. Biophys Rev *10*, 1587-1604. 10.1007/s12551-018-0467-7.
32. Phuyal, S., and Farhan, H. (2019). Multifaceted Rho GTPase Signaling at the Endomembranes. Front Cell Dev Biol *7*, 127. 10.3389/fcell.2019.00127.
33. Gautreau, A.M., Fregoso, F.E., Simanov, G., and Dominguez, R. (2022). Nucleation, stabilization, and disassembly of branched actin networks. Trends in cell biology *32*, 421-432. 10.1016/j.tcb.2021.10.006.
34. Kouranti, I., Sachse, M., Arouche, N., Goud, B., and Echard, A. (2006). Rab35 regulates an endocytic recycling pathway essential for the terminal steps of cytokinesis. Current biology : CB *16*, 1719-1725.
35. Allaire, P.D., Marat, A.L., Dall'Armi, C., Di Paolo, G., McPherson, P.S., and Ritter, B. (2010). The Connecdenn DENN domain: a GEF for Rab35 mediating cargo-specific exit from early endosomes. Mol Cell *37*, 370-382. S1097-2765(10)00076-6 [pii] 10.1016/j.molcel.2009.12.037.
36. Rahajeng, J., Giridharan, S.S., Cai, B., Naslavsky, N., and Caplan, S. (2012). MICAL-L1 is a tubular endosomal membrane hub that connects Rab35 and Arf6 with Rab8a. Traffic *13*, 82-93. 10.1111/j.1600-0854.2011.01294.x.
37. Allaire, P.D., Seyed Sadr, M., Chaineau, M., Seyed Sadr, E., Konefal, S., Fotouhi, M., Maret, D., Ritter, B., Del Maestro, R.F., and McPherson, P.S. (2013). Interplay between Rab35 and Arf6 controls cargo recycling to coordinate cell adhesion and migration. J Cell Sci *126*, 722-731. 10.1242/jcs.112375.
38. Kobayashi, H., and Fukuda, M. (2013). Rab35 establishes the EHD1-association site by coordinating two distinct effectors during neurite outgrowth. J Cell Sci *126*, 2424-2435. 10.1242/jcs.117846.
39. Cauvin, C., Rosendale, M., Gupta-Rossi, N., Rocancourt, M., Larraufie, P., Salomon, R., Perrais, D., and Echard, A. (2016). Rab35 GTPase Triggers Switch-like Recruitment of the Lowe Syndrome Lipid Phosphatase OCRL on Newborn Endosomes. Current biology : CB *26*, 120-128. 10.1016/j.cub.2015.11.040.
40. Youn, J.Y., Dunham, W.H., Hong, S.J., Knight, J.D.R., Bashkurov, M., Chen, G.I., Bagci, H., Rathod, B., MacLeod, G., Eng, S.W.M., et al. (2018). High-Density Proximity Mapping Reveals the Subcellular Organization of mRNA-Associated Granules and Bodies. Mol Cell *69*, 517-532.e511. 10.1016/j.molcel.2017.12.020.
41. Kobayashi, H., Etoh, K., Ohbayashi, N., and Fukuda, M. (2014). Rab35 promotes the recruitment of Rab8, Rab13 and Rab36 to recycling endosomes through MICAL-L1 during neurite outgrowth. Biol Open *3*, 803-814. 10.1242/bio.20148771.
42. Varadi, M., Anyango, S., Deshpande, M., Nair, S., Natassia, C., Yordanova, G., Yuan, D., Stroe, O., Wood, G., Laydon, A., et al. (2022). AlphaFold Protein Structure Database: massively expanding the structural coverage of protein-sequence space with high-accuracy models. Nucleic acids research *50*, D439-d444. 10.1093/nar/gkab1061.
43. Caspary, T., Larkins, C.E., and Anderson, K.V. (2007). The graded response to Sonic Hedgehog depends on cilia architecture. Developmental cell *12*, 767-778. 10.1016/j.devcel.2007.03.004.

44. Cevik, S., Sanders, A.A., Van Wijk, E., Boldt, K., Clarke, L., van Reeuwijk, J., Hori, Y., Horn, N., Hetterschijt, L., Wdowicz, A., et al. (2013). Active transport and diffusion barriers restrict Joubert Syndrome-associated ARL13B/ARL-13 to an Inv-like ciliary membrane subdomain. PLoS genetics *9*, e1003977. 10.1371/journal.pgen.1003977.
45. Lu, H., Toh, M.T., Narasimhan, V., Thamilselvam, S.K., Choksi, S.P., and Roy, S. (2015). A function for the Joubert syndrome protein Arl13b in ciliary membrane extension and ciliary length regulation. Dev Biol *397*, 225-236. 10.1016/j.ydbio.2014.11.009.
46. Nozaki, S., Katoh, Y., Terada, M., Michisaka, S., Funabashi, T., Takahashi, S., Kontani, K., and Nakayama, K. (2017). Regulation of ciliary retrograde protein trafficking by the Joubert syndrome proteins ARL13B and INPP5E. J Cell Sci *130*, 563-576. 10.1242/jcs.197004.
47. Yoder, B.K., Tousson, A., Millican, L., Wu, J.H., Bugg, C.E., Jr., Schafer, J.A., and Balkovetz, D.F. (2002). Polaris, a protein disrupted in orpk mutant mice, is required for assembly of renal cilium. Am J Physiol Renal Physiol *282*, F541-552. 10.1152/ajprenal.00273.2001.
48. Barral, D.C., Garg, S., Casalou, C., Watts, G.F., Sandoval, J.L., Ramalho, J.S., Hsu, V.W., and Brenner, M.B. (2012). Arl13b regulates endocytic recycling traffic. Proceedings of the National Academy of Sciences of the United States of America *109*, 21354-21359. 10.1073/pnas.1218272110.
49. Kobayashi, H., and Fukuda, M. (2012). Rab35 regulates Arf6 activity through centaurin-beta2 (ACAP2) during neurite outgrowth. J Cell Sci *125*, 2235-2243. 10.1242/jcs.098657.
50. Chesneau, L., Dambournet, D., Machicoane, M., Kouranti, I., Fukuda, M., Goud, B., and Echard, A. (2012). An ARF6/Rab35 GTPase cascade for endocytic recycling and successful cytokinesis. Current biology : CB *22*, 147-153. S0960-9822(11)01378-9 [pii] 10.1016/j.cub.2011.11.058.
51. Sander, E.E., ten Klooster, J.P., van Delft, S., van der Kammen, R.A., and Collard, J.G. (1999). Rac downregulates Rho activity: reciprocal balance between both GTPases determines cellular morphology and migratory behavior. The Journal of cell biology *147*, 1009-1022. 10.1083/jcb.147.5.1009.
52. Rossi, A., Kontarakis, Z., Gerri, C., Nolte, H., Hölper, S., Krüger, M., and Stainier, D.Y. (2015). Genetic compensation induced by deleterious mutations but not gene knockdowns. Nature *524*, 230-233. 10.1038/nature14580.
53. Kushawah, G., Hernandez-Huertas, L., Abugattas-Nuñez Del Prado, J., Martinez-Morales, J.R., DeVore, M.L., Hassan, H., Moreno-Sanchez, I., Tomas-Gallardo, L., Diaz-Moscoso, A., Monges, D.E., et al. (2020). CRISPR-Cas13d Induces Efficient mRNA Knockdown in Animal Embryos. Developmental cell *54*, 805-817.e807. 10.1016/j.devcel.2020.07.013.
54. Ferreira, R.R., Pakula, G., Klaeyle, L., Fukui, H., Vilfan, A., Supatto, W., and Vermot, J. (2018). Chiral Cilia Orientation in the Left-Right Organizer. Cell reports *25*, 2008-2016.e2004. 10.1016/j.celrep.2018.10.069.
55. Kuijl, C., Pilli, M., Alahari, S.K., Janssen, H., Khoo, P.S., Ervin, K.E., Calero, M., Jonnalagadda, S., Scheller, R.H., Neefjes, J., and Junutula, J.R. (2013). Rac and Rab GTPases dual effector Nischarin regulates vesicle maturation to facilitate survival of intracellular bacteria. The EMBO journal *32*, 713-727. 10.1038/emboj.2013.10.
56. Fukuda, M., Kanno, E., Ishibashi, K., and Itoh, T. (2008). Large scale screening for novel rab effectors reveals unexpected broad Rab binding specificity. Molecular & cellular

proteomics : MCP *7*, 1031-1042. M700569-MCP200 [pii] 10.1074/mcp.M700569-MCP200.

57. Juhl, A.D., Anvarian, Z., Kuhns, S., Berges, J., Andersen, J.S., Wüstner, D., and Pedersen, L.B. (2023). Transient accumulation and bidirectional movement of KIF13B in primary cilia. J Cell Sci *136*. 10.1242/jcs.259257.
58. Breslow, D.K., Koslover, E.F., Seydel, F., Spakowitz, A.J., and Nachury, M.V. (2013). An in vitro assay for entry into cilia reveals unique properties of the soluble diffusion barrier. The Journal of cell biology *203*, 129-147. 10.1083/jcb.201212024.
59. Yuan, S., Zhao, L., Brueckner, M., and Sun, Z. (2015). Intraciliary calcium oscillations initiate vertebrate left-right asymmetry. Current biology : CB *25*, 556-567. 10.1016/j.cub.2014.12.051.
60. Mizuno, K., Shiozawa, K., Katoh, T.A., Minegishi, K., Ide, T., Ikawa, Y., Nishimura, H., Takaoka, K., Itabashi, T., Iwane, A.H., et al. (2020). Role of Ca(2+) transients at the node of the mouse embryo in breaking of left-right symmetry. Sci Adv *6*, eaba1195. 10.1126/sciadv.aba1195.
61. Hernandez-Hernandez, V., Pravincumar, P., Diaz-Font, A., May-Simera, H., Jenkins, D., Knight, M., and Beales, P.L. (2013). Bardet-Biedl syndrome proteins control the cilia length through regulation of actin polymerization. Hum Mol Genet *22*, 3858-3868. 10.1093/hmg/ddt241.
62. Stewart, K., Gaitan, Y., Shafer, M.E., Aoudjit, L., Hu, D., Sharma, R., Tremblay, M., Ishii, H., Marcotte, M., Stanga, D., et al. (2016). A Point Mutation in p190A RhoGAP Affects Ciliogenesis and Leads to Glomerulocystic Kidney Defects. PLoS genetics *12*, e1005785. 10.1371/journal.pgen.1005785.
63. Cai, J., Song, X., Wang, W., Watnick, T., Pei, Y., Qian, F., and Pan, D. (2018). A RhoA-YAP-c-Myc signaling axis promotes the development of polycystic kidney disease. Genes Dev *32*, 781-793. 10.1101/gad.315127.118.
64. Streets, A.J., Prosseda, P.P., and Ong, A.C. (2020). Polycystin-1 regulates ARHGAP35-dependent centrosomal RhoA activation and ROCK signaling. JCI Insight *5*. 10.1172/jci.insight.135385.
65. Jewett, C.E., Soh, A.W.J., Lin, C.H., Lu, Q., Lencer, E., Westlake, C.J., Pearson, C.G., and Prekeris, R. (2021). RAB19 Directs Cortical Remodeling and Membrane Growth for Primary Ciliogenesis. Developmental cell *56*, 325-340.e328. 10.1016/j.devcel.2020.12.003.
66. Kumar, R., Francis, V., Kulasekaran, G., Khan, M., Armstrong, G.A.B., and McPherson, P.S. (2022). A cell-based GEF assay reveals new substrates for DENN domains and a role for DENND2B in primary ciliogenesis. Sci Adv *8*, eabk3088. 10.1126/sciadv.abk3088.
67. Hashimoto, M., Shinohara, K., Wang, J., Ikeuchi, S., Yoshiba, S., Meno, C., Nonaka, S., Takada, S., Hatta, K., Wynshaw-Boris, A., and Hamada, H. (2010). Planar polarization of node cells determines the rotational axis of node cilia. Nature cell biology *12*, 170-176. 10.1038/ncb2020.
68. Epting, D., Slanchev, K., Boehlke, C., Hoff, S., Loges, N.T., Yasunaga, T., Indorf, L., Nestel, S., Lienkamp, S.S., Omran, H., et al. (2015). The Rac1 regulator ELMO controls basal body migration and docking in multiciliated cells through interaction with Ezrin. Development *142*, 174-184. 10.1242/dev.112250.
69. Wang, K., Yuen, S.T., Xu, J., Lee, S.P., Yan, H.H., Shi, S.T., Siu, H.C., Deng, S., Chu, K.M., Law, S., et al. (2014). Whole-genome sequencing and comprehensive molecular

profiling identify new driver mutations in gastric cancer. Nat Genet *46*, 573-582. 10.1038/ng.2983.
70. Tate, J.G., Bamford, S., Jubb, H.C., Sondka, Z., Beare, D.M., Bindal, N., Boutselakis, H., Cole, C.G., Creatore, C., Dawson, E., et al. (2019). COSMIC: the Catalogue Of Somatic Mutations In Cancer. Nucleic acids research *47*, D941-d947. 10.1093/nar/gky1015.
71. Robert, A., Margall-Ducos, G., Guidotti, J.E., Brégerie, O., Celati, C., Bréchot, C., and Desdouets, C. (2007). The intraflagellar transport component IFT88/polaris is a centrosomal protein regulating G1-S transition in non-ciliated cells. J Cell Sci *120*, 628-637. 10.1242/jcs.03366.
72. Bollig, F., Perner, B., Besenbeck, B., Köthe, S., Ebert, C., Taudien, S., and Englert, C. (2009). A highly conserved retinoic acid responsive element controls wt1a expression in the zebrafish pronephros. Development *136*, 2883-2892. 10.1242/dev.031773.
73. Borovina, A., Superina, S., Voskas, D., and Ciruna, B. (2010). Vangl2 directs the posterior tilting and asymmetric localization of motile primary cilia. Nature cell biology *12*, 407-412. 10.1038/ncb2042.
74. Klinkert, K., Rocancourt, M., Houdusse, A., and Echard, A. (2016). Rab35 GTPase couples cell division with initiation of epithelial apico-basal polarity and lumen opening. Nat Commun *7*, 11166. 10.1038/ncomms11166.
75. Kimmel, C.B., Ballard, W.W., Kimmel, S.R., Ullmann, B., and Schilling, T.F. (1995). Stages of embryonic development of the zebrafish. Dev Dyn *203*, 253-310. 10.1002/aja.1002030302.
76. Fukuda, M., Kobayashi, H., Ishibashi, K., and Ohbayashi, N. (2011). Genome-wide Investigation of the Rab Binding Activity of RUN Domains: Development of a Novel Tool that Specifically Traps GTP-Rab35. Cell Struct Funct. JST.JSTAGE/csf/11001 [pii].
77. Edwards, P. (2002). Origin 7.0: Scientific Graphing and Data Analysis Software. J. Chem. Inf. Comput. Sci., 1270-1271.
78. Legrand, P. (2017). XDSME: XDS Made Easier. GitHub repository *https://github.com/legrandp/xdsme*. DOI:10.5281/zenodo.837885.
79. Sheldrick, G.M. (2008). A short history of SHELX. Acta Crystallogr A *64*, 112-122. 10.1107/s0108767307043930.
80. Read, R.J., and McCoy, A.J. (2011). Using SAD data in Phaser. Acta Crystallogr D Biol Crystallogr *67*, 338-344. 10.1107/s0907444910051371.
81. Cowtan, K. (2000). General quadratic functions in real and reciprocal space and their application to likelihood phasing. Acta Crystallogr D Biol Crystallogr *56*, 1612-1621. 10.1107/s0907444900013263.
82. Cowtan, K. (2006). The Buccaneer software for automated model building. 1. Tracing protein chains. Acta Crystallogr D Biol Crystallogr *62*, 1002-1011. 10.1107/s0907444906022116.
83. Bricogne G., B.E., Brandl M., Flensburg C., Keller P., Paciorek W.,, and Roversi P, S.A., Smart O.S., Vonrhein C., Womack T.O. (2017). BUSTER version 2.10.3 Cambridge,. United Kingdom: Global Phasing Ltd.
84. Emsley, P., and Cowtan, K. (2004). Coot: model-building tools for molecular graphics. Acta Crystallogr D Biol Crystallogr *60*, 2126-2132. 10.1107/s0907444904019158.
85. Adams, P.D., Afonine, P.V., Bunkóczi, G., Chen, V.B., Davis, I.W., Echols, N., Headd, J.J., Hung, L.W., Kapral, G.J., Grosse-Kunstleve, R.W., et al. (2010). PHENIX: a comprehensive Python-based system for macromolecular structure solution. Acta Crystallogr D Biol Crystallogr *66*, 213-221. 10.1107/s0907444909052925.

86. Vonrhein, C., Flensburg, C., Keller, P., Sharff, A., Smart, O., Paciorek, W., Womack, T., and Bricogne, G. (2011). Data processing and analysis with the autoPROC toolbox. Acta Crystallogr D Biol Crystallogr *67*, 293-302. 10.1107/s0907444911007773.
87. Winn, M.D., Ballard, C.C., Cowtan, K.D., Dodson, E.J., Emsley, P., Evans, P.R., Keegan, R.M., Krissinel, E.B., Leslie, A.G., McCoy, A., et al. (2011). Overview of the CCP4 suite and current developments. Acta Crystallogr D Biol Crystallogr *67*, 235-242. 10.1107/s0907444910045749.
88. Rodríguez, D., Sammito, M., Meindl, K., de Ilarduya, I.M., Potratz, M., Sheldrick, G.M., and Usón, I. (2012). Practical structure solution with ARCIMBOLDO. Acta Crystallogr D Biol Crystallogr *68*, 336-343. 10.1107/s0907444911056071.
89. Konarev PV, Volkov V, Sokolova AV, Koch MHJ, and DI, S. (2003). PRIMUS: a Windows PC-based system for small-angle scattering data analysis. J. Appl. Cryst. *36*, 1277-1282.
90. Svergun DI (1992). Determination of the regularization parameter in indirect-transform methods using perceptual criteria. J. Appl. Cryst. *25*, 495-503.
91. Schneidman-Duhovny, D., Hammel, M., Tainer, J.A., and Sali, A. (2016). FoXS, FoXSDock and MultiFoXS: Single-state and multi-state structural modeling of proteins and their complexes based on SAXS profiles. Nucleic acids research *44*, W424-429. 10.1093/nar/gkw389.
92. Webb, B., and Sali, A. (2016). Comparative Protein Structure Modeling Using MODELLER. Curr Protoc Bioinformatics *54*, 5.6.1-5.6.37. 10.1002/cpbi.3.
93. Fremont, S., Hammich, H., Bai, J., Wioland, H., Klinkert, K., Rocancourt, M., Kikuti, C., Stroebel, D., Romet-Lemonne, G., Pylypenko, O., et al. (2017). Oxidation of F-actin controls the terminal steps of cytokinesis. Nat Commun *8*, 14528. 10.1038/ncomms14528.
94. Ball, G., Demmerle, J., Kaufmann, R., Davis, I., Dobbie, I.M., and Schermelleh, L. (2015). SIMcheck: a Toolbox for Successful Super-resolution Structured Illumination Microscopy. Scientific reports *5*, 15915. 10.1038/srep15915.
95. Hauptmann, G., and Gerster, T. (1994). Two-color whole-mount in situ hybridization to vertebrate and Drosophila embryos. Trends Genet *10*, 266. 10.1016/0168-9525(90)90008-t.
96. Ershov, D., Phan, M.S., Pylvänäinen, J.W., Rigaud, S.U., Le Blanc, L., Charles-Orszag, A., Conway, J.R.W., Laine, R.F., Roy, N.H., Bonazzi, D., et al. (2022). TrackMate 7: integrating state-of-the-art segmentation algorithms into tracking pipelines. Nat Methods *19*, 829-832. 10.1038/s41592-022-01507-1.

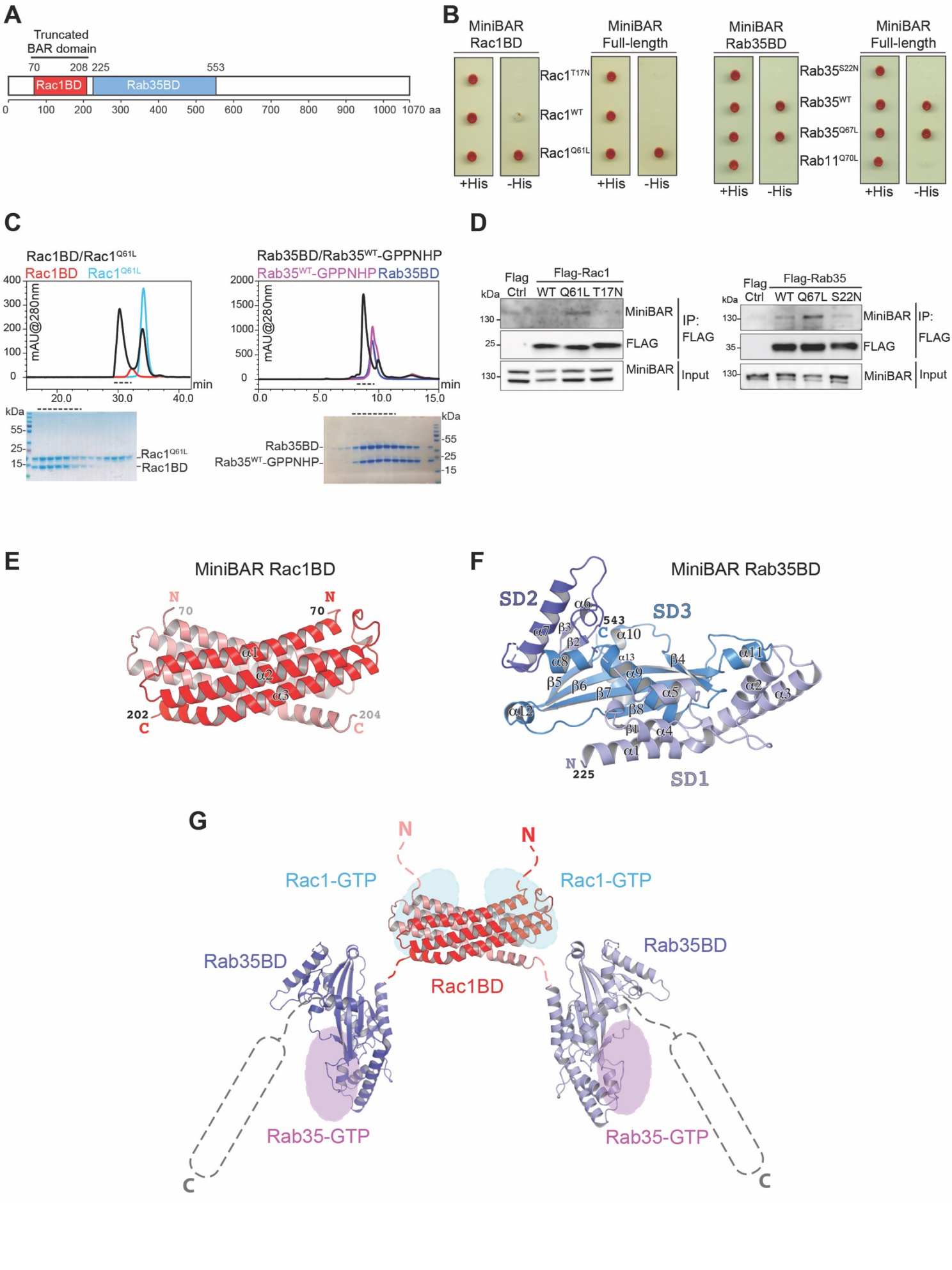
A
Truncated BAR domain
70
208
225
553
Rac1BD
Rab35BD
0
100
200
300
400
500
600
700
800
900
1000
1070 aa
B
MiniBAR Rac1BD
MiniBAR Full-length
MiniBAR Rab35BD
MiniBAR Full-length
Rac1T17N
Rac1WT
Rac1Q61L
Rab35S22N
Rab35WT
Rab35Q67L
Rab11Q70L
+His
-His
C
Rac1BD/Rac1Q61L
Rac1BD
Rac1Q61L
mAU@280nm
min
kDa
Rac1Q61L
Rac1BD
Rab35BD/Rab35WT-GPPNHP
Rab35WT-GPPNHP
Rab35BD
Rab35BD-
Rab35WT-GPPNHP-
D
Flag
Ctrl
Flag-Rac1
WT Q61L T17N
Flag-Rab35
WT Q67L S22N
MiniBAR
FLAG
IP: FLAG
Input
E
MiniBAR Rac1BD
N
70
202
C
204
α1
α2
α3
F
MiniBAR Rab35BD
SD2
SD3
SD1
543
225
G
Rac1-GTP
Rab35BD
Rac1BD
Rab35-GTP

Figure 1. MiniBAR is a dual Rac1 and Rab35 effector with a truncated BAR domain

(A) Scheme representing MiniBAR domains.

(B) Yeast 2-hybrid assays reveal interactions with the indicated proteins when growth is detected without histidine (-His).

(C) Analytical gel-filtration elution profiles of Rac1BD (left panels), Rab35 BD (right panels), Rab35-GPPNHP and $Rac1^{Q61L}$ in comparison with their complexes. The elution fractions corresponding to the complexes elution peaks (black dashed lines) were analyzed by SDS-PAGE, and masses were determined by MALS. Rac1BD ($Mass_{MALS}$ 30.1 $\pm$ 0.4% kDa), $Rac1^{Q61L}$ ($Mass_{MALS}$ 20.6 $\pm$ 0.8% kDa), Rac1BD/$Rac1^{Q61L}$ complex ($Mass_{MALS}$ 69.9 $\pm$0 .3% kDa), Rab35BD ($Mass_{MALS}$ 36.4 $\pm$ 0.7% kDa), Rab35-GPPNHP ($Mass_{MALS}$ 22.2 $\pm$ 0.1% kDa), Rab35BD/Rab35-GPPNHP complex ($Mass_{MALS}$ 50.8 $\pm$ 0.8% kDa).

(D) Co-immunoprecipitated endogenous MiniBAR from RPE-1 cells with indicated flagged proteins were detected by western blot. Bottom panels: inputs (3% of total lysates).

(E) Crystal structure of Rac1BD.

(F) Crystal structure of Rab35BD.

(G) Model of MiniBAR Rac1BD-Rab35BD unit, the putative positions of Rac1, Rab35 binding sites and the C-terminal disordered domain are indicated.

See also Figures S1, S2, S3, S5 and Table S1.

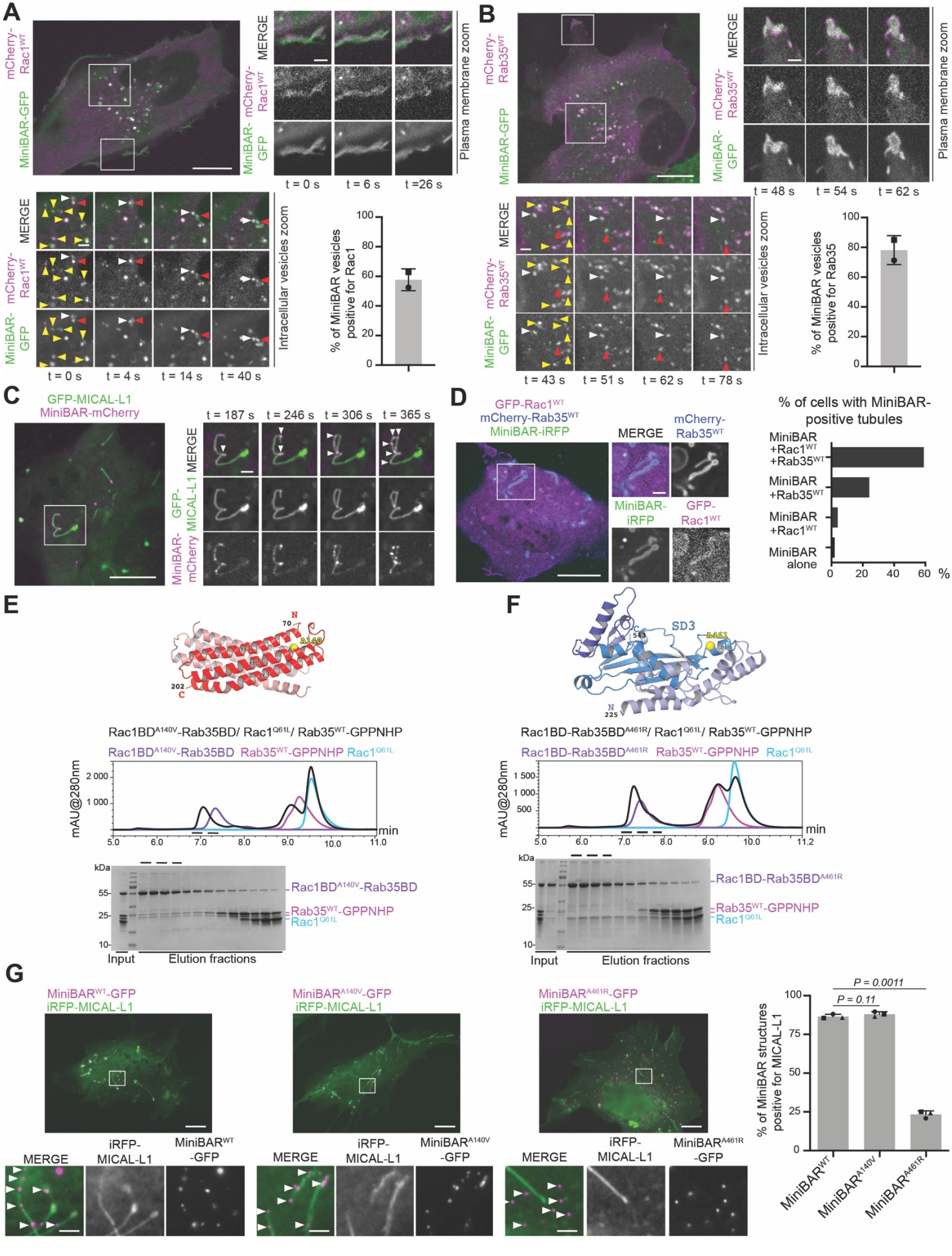
A
mCherry-Rac1WT
MiniBAR-GFP
MERGE
mCherry-Rac1WT
MiniBAR-GFP
t = 0 s
t = 6 s
t =26 s
Plasma membrane zoom
t = 0 s
t = 4 s
t = 14 s
t = 40 s
Intracellular vesicles zoom
% of MiniBAR vesicles positive for Rac1
B
mCherry-Rab35WT
MiniBAR-GFP
t = 48 s
t = 54 s
t = 62 s
t = 43 s
t = 51 s
t = 62 s
t = 78 s
% of MiniBAR vesicles positive for Rab35
C
GFP-MICAL-L1
MiniBAR-mCherry
t = 187 s
t = 246 s
t = 306 s
t = 365 s
GFP-MICAL-L1
MiniBAR-mCherry
D
GFP-Rac1WT
mCherry-Rab35WT
MiniBAR-iRFP
MiniBAR-iRFP
GFP-Rac1WT
% of cells with MiniBAR-positive tubules
MiniBAR +Rac1WT +Rab35WT
MiniBAR +Rab35WT
MiniBAR +Rac1WT
MiniBAR alone
E
Rac1BDA140V-Rab35BD/ Rac1Q61L/ Rab35WT-GPPNHP
Rac1BDA140V-Rab35BD
Rab35WT-GPPNHP
Rac1Q61L
mAU@280nm
min
Rac1BDA140V-Rab35BD
Rab35WT-GPPNHP
Rac1Q61L
Input
Elution fractions
F
Rac1BD-Rab35BDA461R/ Rac1Q61L/ Rab35WT-GPPNHP
Rac1BD-Rab35BDA461R
Rab35WT-GPPNHP
Rac1Q61L
mAU@280nm
min
Rac1BD-Rab35BDA461R
Rab35WT-GPPNHP
Rac1Q61L
Input
Elution fractions
G
MiniBARWT-GFP
iRFP-MICAL-L1
MiniBARA140V-GFP
iRFP-MICAL-L1
MiniBARA461R-GFP
iRFP-MICAL-L1
MERGE
iRFP-MICAL-L1
MiniBARWT-GFP
MERGE
iRFP-MICAL-L1
MiniBARA140V-GFP
MERGE
iRFP-MICAL-L1
MiniBARA461R-GFP
P = 0.0011
P = 0.11
% of MiniBAR structures positive for MICAL-L1
MiniBARWT
MiniBARA140V
MiniBARA461R

Figure 2. MiniBAR partially colocalizes with Rac1 and Rab35 at the plasma membrane and on dynamic intracellular vesicles

(A) Top left panel: Snapshot of a movie of RPE-1 cells stably co-expressing MiniBAR-GFP and mCherry-Rac1^{WT}. Top right and Bottom left panels: Selected time points of zoomed regions. Arrowheads: co-localization on vesicles; yellow and red arrowheads: displacement of two selected moving vesicles. Bottom right panel: percentage of MiniBAR-GFP vesicles positive for mCherry-Rac1^{WT}. Mean ± SD, n = 57-124 MiniBAR-positive vesicles per cell, n = 14 cells.

(B) Same as (A) for an RPE-1 cells co-expressing MiniBAR-GFP and mCherry-Rab35^{WT}. Bottom right panel: percentage of MiniBAR-GFP vesicles positive for mCherry-Rab35^{WT}. Mean ± SD, n = 91-143 MiniBAR-positive vesicles per cell, n = 6 cells.

(C) Left panel: Snapshot of a movie of an RPE-1 cells co-expressing GFP-MICAL-L1 and MiniBAR-mCherry. Right panels: snapshots of a zoomed region. Arrowheads: accumulation of MiniBAR.

(D) Left panels: RPE-1 cell co-expressing GFP-Rac1^{WT}, mCherry-Rab35^{WT} and MiniBAR-iRFP. Zoomed region: tubular structure labelled by the three proteins. Right panel: percentage of cells with MiniBAR-GFP-positive tubules after expression or not of Rab35 and/or Rac1, as indicated. n > 50 cells per condition.

(E-F) Analytical gel-filtration elution profiles of Rac1BD-Rab35BD (MiniBAR$^{70-553}$) mutants, Rab35-GPPNHP and Rac1^{Q61L} in comparison with the ternary protein complexes. The elution fractions corresponding to the complex elution peaks were analyzed by SDS-PAGE. (E) Yellow ball: A140V mutation. The Rac1BD^{A140V}-Rab35BD mutant co-elutes with Rab35 but not with Rac1. (F) Yellow ball: A461R mutation. The Rac1BD-Rab35BD^{A461R} mutant co-elutes with Rac1 but not with Rab35.

(G) Left panels: fixed RPE-1 cells co-expressing iRFP-MICAL-L1 with either MiniBAR^{WT}-GFP, MiniBAR^{A140V}-GFP or MiniBAR^{A461R}-GFP, as indicated. Right panel: percentage of MiniBAR-GFP structures positive for MICAL-L1 in the indicated conditions. Mean ± SD, n = 61-96 MiniBAR-positive vesicles per cell, n = 33-36 cells per condition, N = 3 independent experiments. Paired student *t*-test.

In A-D and G, cells were cultured in medium with serum; Scale bars, 10 μm (general views) and 2 μm (insets).

See also Figures S4 and S5.

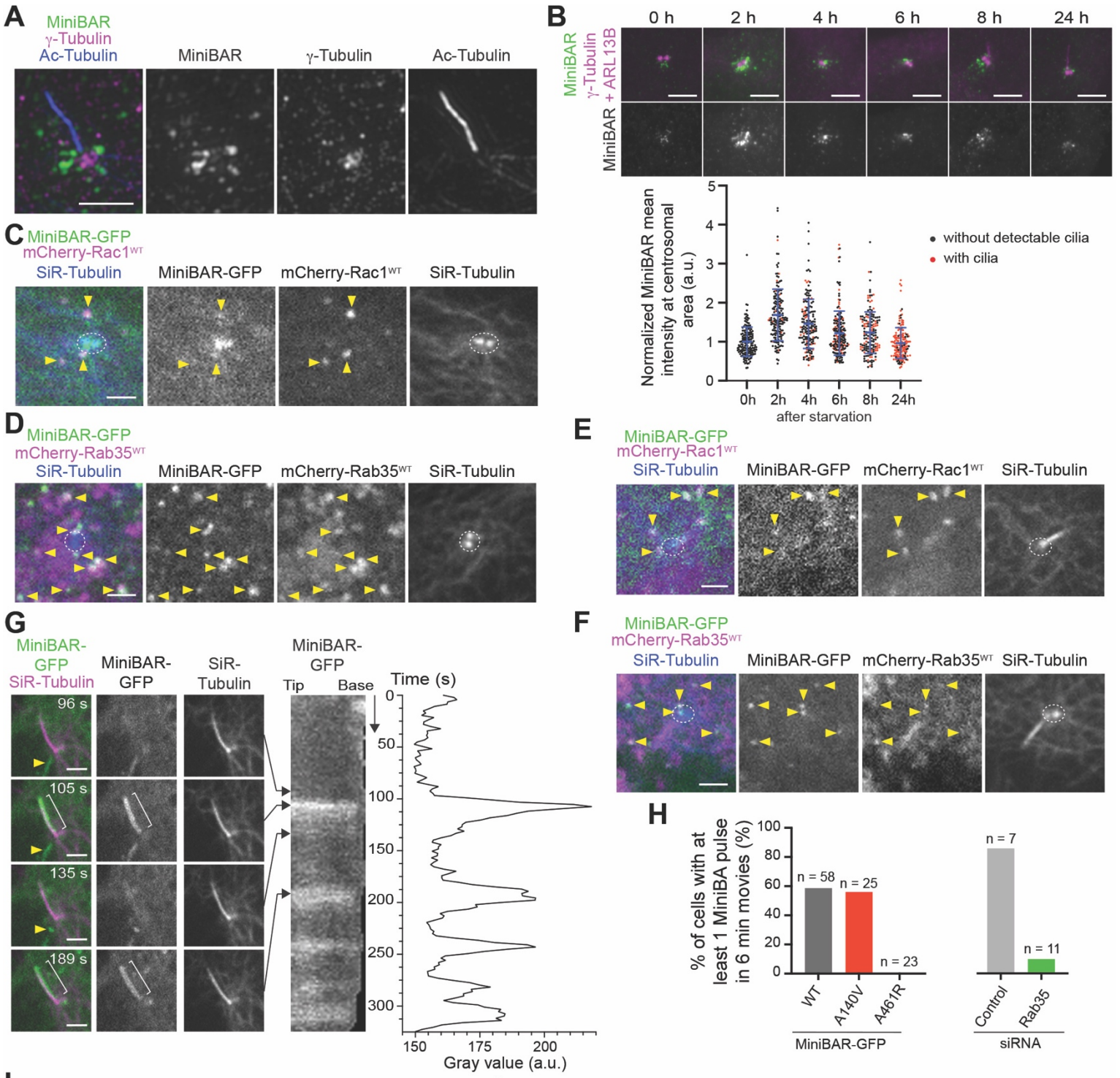
A
MiniBAR
γ-Tubulin
Ac-Tubulin
MiniBAR
γ-Tubulin
Ac-Tubulin
B
0 h
2 h
4 h
6 h
8 h
24 h
MiniBAR
γ-Tubulin
MiniBAR + ARL13B
Normalized MiniBAR mean intensity at centrosomal area (a.u.)
without detectable cilia
with cilia
0h
2h
4h
6h
8h
24h
after starvation
C
MiniBAR-GFP
mCherry-Rac1WT
SiR-Tubulin
MiniBAR-GFP
mCherry-Rac1WT
SiR-Tubulin
D
MiniBAR-GFP
mCherry-Rab35WT
SiR-Tubulin
MiniBAR-GFP
mCherry-Rab35WT
SiR-Tubulin
E
MiniBAR-GFP
mCherry-Rac1WT
SiR-Tubulin
MiniBAR-GFP
mCherry-Rac1WT
SiR-Tubulin
F
MiniBAR-GFP
mCherry-Rab35WT
SiR-Tubulin
MiniBAR-GFP
mCherry-Rab35WT
SiR-Tubulin
G
MiniBAR-GFP
SiR-Tubulin
MiniBAR-GFP
SiR-Tubulin
MiniBAR-GFP
Tip
Base
Time (s)
96 s
105 s
135 s
189 s
Gray value (a.u.)
H
% of cells with at least 1 MiniBA pulse in 6 min movies (%)
n = 58
n = 25
n = 23
WT
A140V
A461R
MiniBAR-GFP
n = 7
n = 11
Control
Rab35
siRNA
I
t = 145 s
t = 152 s
t = 167 s
MiniBAR-GFP
mCherry-Rac1WT
SiR-Tubulin
MiniBAR-GFP
mCherry-Rac1WT
SiR-Tubulin
J
t = 87 s
t = 102 s
t = 125 s
t = 130 s
t = 135 s
MiniBAR-GFP
mCherry-Rab35WT
SiR-Tubulin
MiniBAR-GFP
mCherry-Rab35WT
SiR-Tubulin

Figure 3. MiniBAR accumulates at the ciliary base and rapidly pulses at the ciliary membrane

(A) Structured Illumination Microscopy images of a ciliated RPE-1 cell stained with endogenous MiniBAR, acetylated-Tubulin and γ-Tubulin. Scale bar, 2 μm.

(B) Top panels: Endogenous localization of MiniBAR, ARL13B and γ-Tubulin in fixed RPE-1 cells following serum removal. Scale bar, 4 μm. Bottom panel: Quantification of MiniBAR intensity at the centrosomal area following serum removal. n = 164-177 cells per condition. N = 3 independent experiments.

(C) Snapshot of a movie of RPE-1 cells stably co-expressing MiniBAR-GFP and mCherry-Rac1^{WT}, incubated with SiR-Tubulin. Acquisition started 3-4 h after serum removal. Arrowheads: co-localization on vesicles at the encircled centrosome area.

(D) Snapshot of a movie of RPE-1 cells stably expressing MiniBAR-GFP, transfected with mCherry-Rab35^{WT} and incubated with SiR-Tubulin. Acquisition started 3-4 h after serum removal. Arrowheads: co-localization on vesicles at the centrosome area.

(E) and (F) Same as in (C) and (D), respectively, in RPE-1 cells with detectable cilia.

(G) Left panels: Snapshots of a movie of RPE-1 cells stably expressing MiniBAR-GFP and incubated with SiR-Tubulin. Acquisition started 3-4 h after serum removal. Yellow arrowhead: a MiniBAR-positive tubulo-vesicle at the ciliary base. White brackets: pulsatile accumulation of MiniBAR-GFP along the cilium. Right panels: Corresponding kymograph of MiniBAR-GFP intensity along the cilium and quantification of the intensity during a 6-minute movie, showing 5 pulses of MiniBAR.

(H) Percentage of cells with at least 1 pulse of MiniBAR-GFP in 6-minute movies in RPE-1 cells stably expressing MiniBAR^{WT}-GFP, MiniBAR^{A140V}-GFP or MiniBAR^{A461R}-GFP, and in RPE-1 cells stably expressing MiniBAR^{WT}-GFP after indicated depletion.

(I) Snapshots of a movie of RPE-1 cells stably expressing MiniBAR-GFP, transfected with mCherry-Rac1^{WT} and incubated with SiR-Tubulin. Acquisition started 3-4 h after serum removal. White brackets: MiniBAR-GFP pulse along the cilium, while mCherry-Rac1^{WT} levels were unchanged.

(J) Snapshots of a movie of RPE-1 cells stably expressing MiniBAR-GFP, transfected with mCherry-Rab35^{WT} and incubated with SiR-Tubulin. Acquisition started 3-4 h after serum removal. White brackets: simultaneous pulsatile accumulation of mCherry-Rab35^{WT} and MiniBAR-GFP along the cilium.

In A-J, cells were cultured in medium without serum. In C-G, I and J: Scale bars, 2 μm.

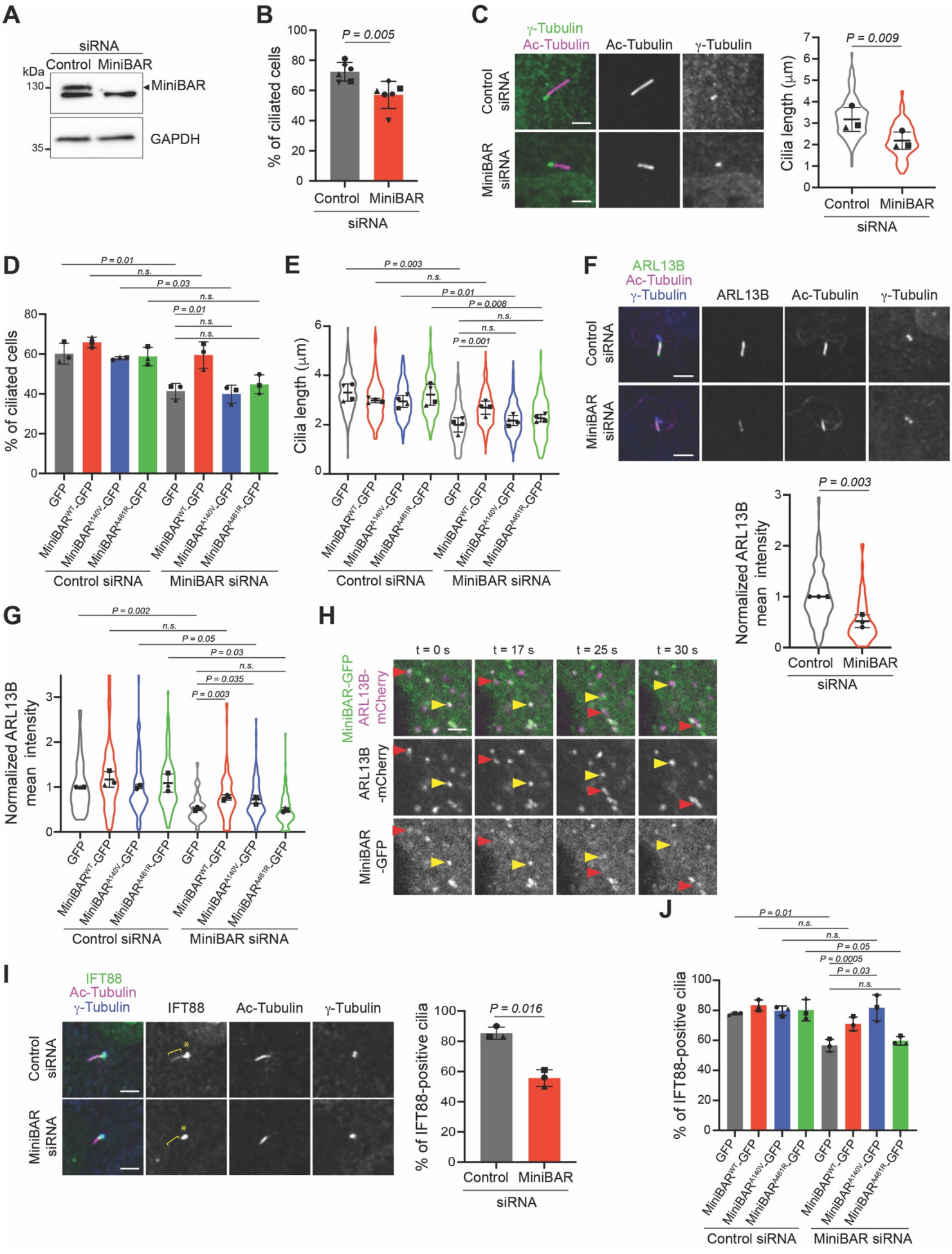
A
siRNA
Control MiniBAR
kDa
130
MiniBAR
35
GAPDH
B
P = 0.005
% of ciliated cells
Control MiniBAR
siRNA
C
γ-Tubulin
Ac-Tubulin
Ac-Tubulin
γ-Tubulin
Control siRNA
MiniBAR siRNA
P = 0.009
Cilia length (μm)
Control MiniBAR
siRNA
D
P = 0.01
n.s.
P = 0.03
n.s.
P = 0.01
n.s.
n.s.
% of ciliated cells
GFP
MiniBARWT-GFP
MiniBARA140V-GFP
MiniBARA461R-GFP
Control siRNA
MiniBAR siRNA
E
P = 0.003
n.s.
P = 0.01
P = 0.008
n.s.
n.s.
P = 0.001
Cilia length (μm)
F
ARL13B
Ac-Tubulin
γ-Tubulin
ARL13B
Ac-Tubulin
γ-Tubulin
Control siRNA
MiniBAR siRNA
P = 0.003
Normalized ARL13B mean intensity
Control MiniBAR
siRNA
G
P = 0.002
n.s.
P = 0.05
P = 0.03
n.s.
P = 0.035
P = 0.003
Normalized ARL13B mean intensity
H
t = 0 s
t = 17 s
t = 25 s
t = 30 s
MiniBAR-GFP
ARL13B-mCherry
ARL13B -mCherry
MiniBAR -GFP
I
IFT88
Ac-Tubulin
γ-Tubulin
IFT88
Ac-Tubulin
γ-Tubulin
Control siRNA
MiniBAR siRNA
P = 0.016
% of IFT88-positive cilia
Control MiniBAR
siRNA
J
P = 0.01
n.s.
n.s.
P = 0.05
P = 0.0005
P = 0.03
n.s.
% of IFT88-positive cilia
Control siRNA
MiniBAR siRNA

Figure 4. MiniBAR promotes cilia growth and controls the localization of IFT88 and ARL13 into cilia

(A) Lysates of RPE-1 cells transfected with control or MiniBAR siRNAs were blotted for MiniBAR and GAPDH (loading control).

(B) Percentage of control- and MiniBAR-depleted cells with cilia (with acetylated-Tubulin-positive axonemes) measured 24 h after serum removal. Mean ± SD, N = 6 independent experiments. Paired student *t*-test.

(C) Left panel: Representative images of cilia in control- and MiniBAR-depleted cells, 48 h after serum removal. Right panel: Mean cilia length ± SD, n = 154-157 cells per condition, N = 3 independent experiments. Paired student *t*-test. In these and all subsequent "violin plots", the distribution of all data points are indicated.

(D) Percentage of ciliated cells 48 h after serum removal, in RPE-1 cells stably expressing either GFP alone, siRNA-resistant MiniBAR^{WT}-GFP, MiniBAR^{A140V}-GFP or MiniBAR^{A461R}-GFP and transfected with either control or MiniBAR siRNAs. Mean ± SD, n = 427-858 cells per condition, N = 3 independent experiments. Paired student *t*-tests.

(E) Cilia length (acetylated-Tubulin staining) in the cells described in (D). Mean ± SD, n = 86-158 cells per condition, N = 3 independent experiments. Paired student *t*-tests.

(F) Top panel: Representative images of cilia in control- and MiniBAR-depleted cells, 48 h after serum removal. Bottom panel: Normalized mean ARL13B intensity in cilia ± SD, n = 144-154 cells per condition, N = 3 independent experiments. Paired student *t*-test.

(G) Mean ARL13B intensity ± SD in cells described in (D), n = 90-130 cells per condition, N = 3 independent experiments. Paired student *t*-tests.

(H) Snapshots of a movie of RPE-1 cells stably expressing MiniBAR-GFP, transfected with ARL13B-mCherry and incubated with SiR-Tubulin. Acquisition started 3-4 h after serum removal. Arrowheads: co-localization on two selected moving vesicles.

(I) Left panel: Representative images of cilia in control- and MiniBAR-depleted cells, 48 h after serum removal. Stars and brackets: IFT88 at ciliary base and the axoneme, respectively. Right panel: Mean percentage of IFT88-positive cilia ± SD, n = 114-128 cells per condition, N = 3 independent experiments. Paired student *t*-test.

(J) Mean percentage of IFT88-positive cilia in cells described in (D) ± SD, n = 85-210 cells per condition, N = 3 independent experiments. Paired student *t*-tests.

In A-J, cells were cultured in medium without serum. Scale bars, 4 μm (C,F, I) and 2 μm (H).

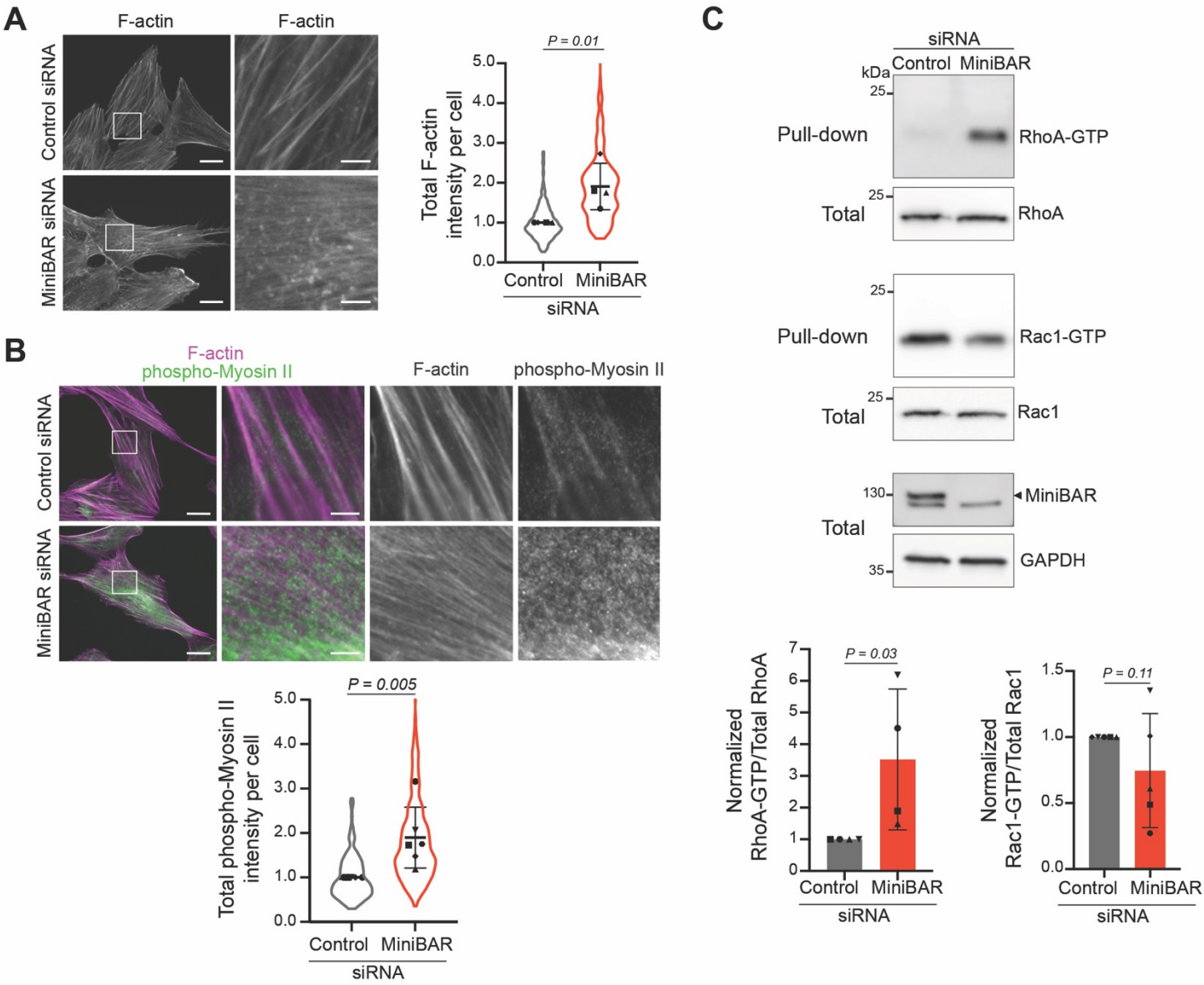
A
F-actin
F-actin
Control siRNA
MiniBAR siRNA
P = 0.01
Total F-actin intensity per cell
5.0
4.0
3.0
2.0
1.0
0.0
Control
MiniBAR
siRNA
B
F-actin
phospho-Myosin II
F-actin
phospho-Myosin II
Control siRNA
MiniBAR siRNA
P = 0.005
Total phospho-Myosin II intensity per cell
5.0
4.0
3.0
2.0
1.0
0.0
Control
MiniBAR
siRNA
C
siRNA
Control
MiniBAR
kDa
25
Pull-down
RhoA-GTP
25
Total
RhoA
25
Pull-down
Rac1-GTP
25
Total
Rac1
130
MiniBAR
Total
35
GAPDH
P = 0.03
Normalized RhoA-GTP/Total RhoA
7
6
5
4
3
2
1
0
Control
MiniBAR
siRNA
P = 0.11
Normalized Rac1-GTP/Total Rac1
1.5
1.0
0.5
0.0
Control
MiniBAR
siRNA
D
Rho-GTP
ROCK
ROCKinh
Y27632
p-Myosin II
actomyosin
contractility
P = 0.004
P = 0.2
P = 0.001
P = 0.01
% of ciliated cells
80
60
40
20
0
Control
ROCKinh
Control
ROCKinh
Control siRNA
MiniBAR siRNA
E
Control
ROCKinh
siRNA
Control
MiniBAR
Ac-tubulin γ-tubulin
Cumulated frequency (%)
100
75
50
25
0
0
2
4
6
8
Cilia length (μm)
siRNA Control
Control
ROCKinh
P = 0.06
siRNA MiniBAR
Control
ROCKinh
P< 0.0001
P< 0.0001
P< 0.0001

Figure 5. MiniBAR also controls cilia length by regulating actin-dependent contractility and RhoA vs. Rac1 activation

(A) Left panel: F-actin staining (phalloidin) in control- and MiniBAR-depleted RPE-1 cells, 48 h after serum removal. Right panel: Normalized mean intensity of total F-actin ± SD, n = 263-402 cells per condition, N = 4 independent experiments. Unpaired student *t*-test.

(B) Top panels: F-actin and phospho-S19 Myosin Regulatory Light Chain staining in cells described in (A). Bottom panel: Normalized mean intensity of total phospho-S19 MRLC ± SD, n = 361-342 cells per condition, N = 5 independent experiments. Unpaired student *t*-test. In A-B: Scale bars, 20 μm (general views) and 4 μm (insets).

(C) Top panels: Pull-down of endogenous Rho^{GTP} and $Rac1^{GTP}$ from lysates of control- and MiniBAR-depleted RPE-1 cells. The total levels of endogenous RhoA, Rac1 and MiniBAR in each condition are also shown. Bottom panels: quantification of $RhoA^{GTP}$ over total RhoA and $Rac1^{GTP}$ over total Rac1. Normalized mean ± SD, N = 5 independent experiments. Unpaired student *t*-test.

(D) Percentage of control- and MiniBAR-depleted cells with cilia 48 h after serum removal and treated or not with the ROCK inhibitor Y27632 for the last 24 h. Mean ± SD, n= 330-429 cells per condition, N = 3 independent experiments. Paired student *t*-tests.

(E) Top panel: Representative images of cilia in cells described in (D). Scale bars, 4 μm. Bottom panel: Distribution of cilia length, n = 187-219 cells per condition, N = 3 independent experiments. KS test.

In A-E, cells were cultured in medium without serum.

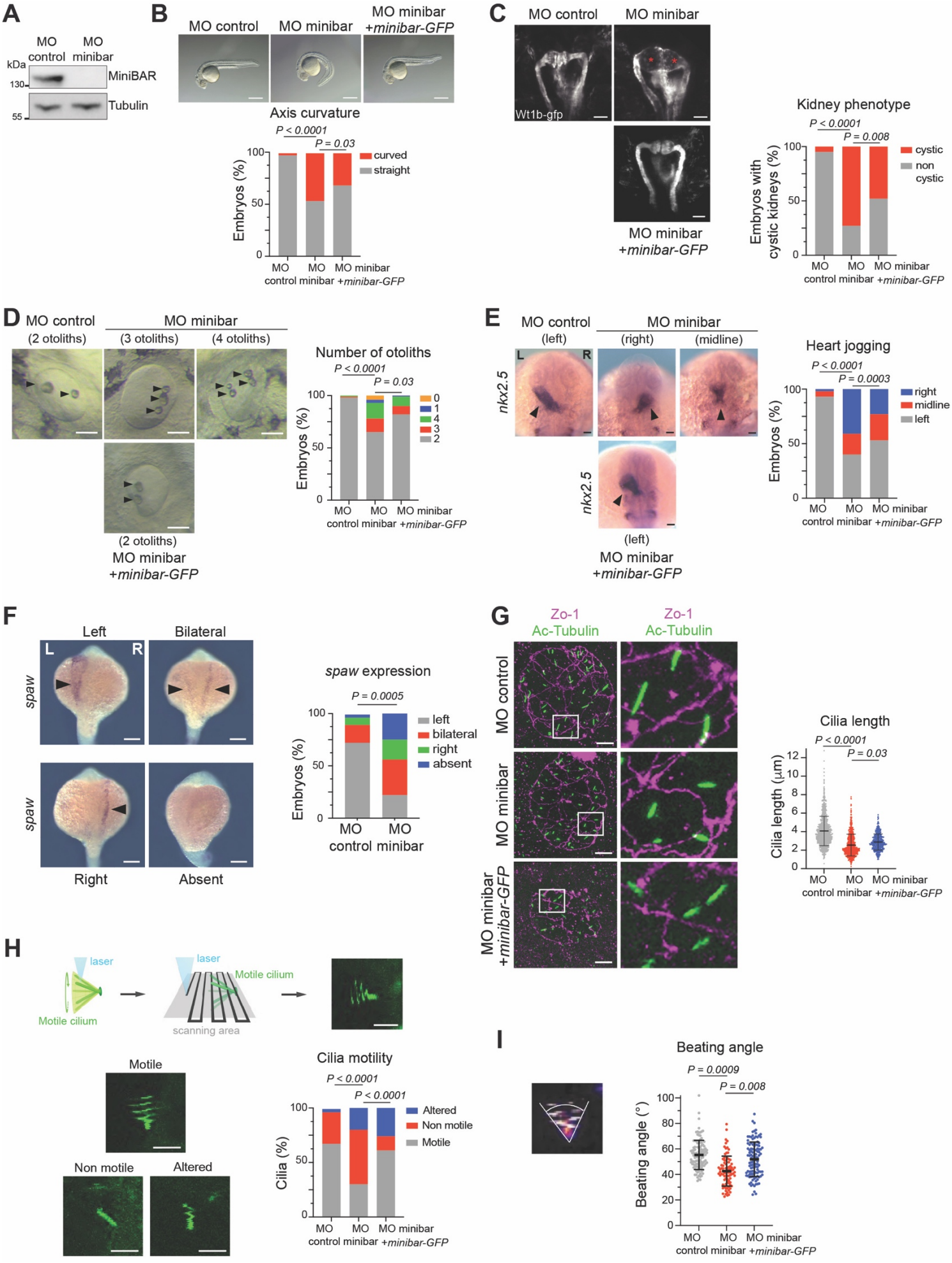
A
MO control
MO minibar
kDa
130
55
MiniBAR
Tubulin
B
MO control
MO minibar
MO minibar +minibar-GFP
Axis curvature
P < 0.0001
P = 0.03
curved
straight
Embryos (%)
MO control
MO minibar
MO minibar +minibar-GFP
C
MO control
MO minibar
Wt1b-gfp
MO minibar +minibar-GFP
Kidney phenotype
P < 0.0001
P = 0.008
cystic
non cystic
Embryos with cystic kidneys (%)
D
MO control
(2 otoliths)
MO minibar
(3 otoliths)
(4 otoliths)
(2 otoliths)
MO minibar +minibar-GFP
Number of otoliths
P < 0.0001
P = 0.03
0
1
4
3
2
E
MO control
(left)
MO minibar
(right)
(midline)
nkx2.5
(left)
MO minibar +minibar-GFP
Heart jogging
P < 0.0001
P = 0.0003
right
midline
left
F
Left
Bilateral
spaw
Right
Absent
spaw expression
P = 0.0005
left
bilateral
right
absent
G
Zo-1
Ac-Tubulin
MO control
MO minibar
MO minibar +minibar-GFP
Cilia length
P < 0.0001
P = 0.03
Cilia length (μm)
H
laser
Motile cilium
scanning area
Motile
Non motile
Altered
Cilia motility
P < 0.0001
P < 0.0001
Altered
Non motile
Motile
Cilia (%)
I
Beating angle
P = 0.0009
P = 0.008
Beating angle (°)
MO
MO
MO minibar
control
minibar
+minibar-GFP

Figure 6. MiniBAR depletion leads to dysfunctional cilia and hallmarks of ciliopathy *in vivo*

(A) Lysates of 24 hours after fertilization (hpf) zebrafish embryos injected with either control or minibar morpholinos (MO) were blotted for MiniBAR and Tubulin (loading control).

(B) Axis curvature at 24 hpf in embryos injected with either MO control, MO minibar or MO minibar co-injected with *minibar-GFP* mRNA. Scale bars, 500 µm. n =68; 130; 95 embryos. Chi-square test.

(C) Kidneys visualized with the *wt1b:gfp* line at 48 hpf in indicated morphants. Asterisks indicate glomerular cysts. Scale bars, 50 µm. n = 37; 59; 60 embryos. Fisher's Exact Test.

(D) Otoliths number at 48 hpf in indicated morphants. Scale bars, 50 µm. Arrowheads: otoliths. n= 84; 99; 139 embryos. Fisher's Exact Test.

(E) Heart jogging defects at 24 hpf, revealed by *in situ* hybridization for *nkx2.5* in indicated morphants. Scale bars, 100 µm. n = 96; 166; 232 embryos. Chi-square test.

(F) *spaw* expression at the 20-somite stage. Scale bars, 200 µm. n= 29; 32 embryos. Fischer's Exact Test.

(G) Left panels: Zo-1 and acetylated-Tubulin immunostaining on Kupffer's vesicle from 8-somite stage of indicated morphants. Scale bars, 10 µm. Right panel: quantification of cilia length. n = 43; 34; 17 embryos and n= 1307; 916; 489 cilia. Linear mixed effect model.

(H) Representative patterns obtained for normally beating, abnormally beating and immobile cilia in *β-actin2:arl13b-gfp* embryos. Scale bars, 5 µm. Bottom right panel: quantification of the different beating patterns in indicated morphants, n=190; 214; 175 cilia. Chi-square test.

(I) Beating angle of motile cilia in indicated morphants. n = 5; 7; 7 embryos and 114; 86; 116 cilia. Linear mixed effect model.

See also Figure S7.

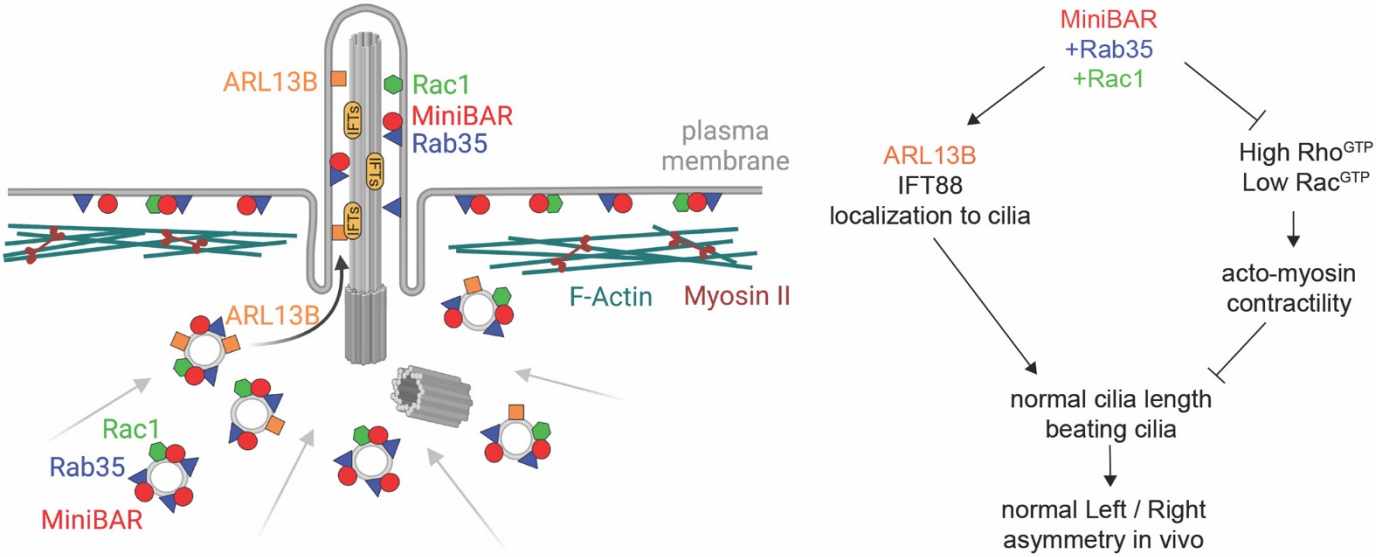

Figure 7. Summary model of the functional role of MiniBAR in ciliogenesis by controlling membrane trafficking and acto-myosin contractility

Left panel: localization of MiniBAR (red), Rab35 (blue) and Rac1 (green) at the plasma membrane and on intracellular vesicles at the ciliary base, and role of MiniBAR in the delivery of ARL13B (orange) and IFT88 (not represented) in cilia.

Right panel: MiniBAR and its interaction with Rab35 and Rac1 promote cargo delivery in cilia and limit acto-myosin contractility. This is both necessary for correct cilia length and beating, and thus normal left-right asymmetry i*n vivo*.

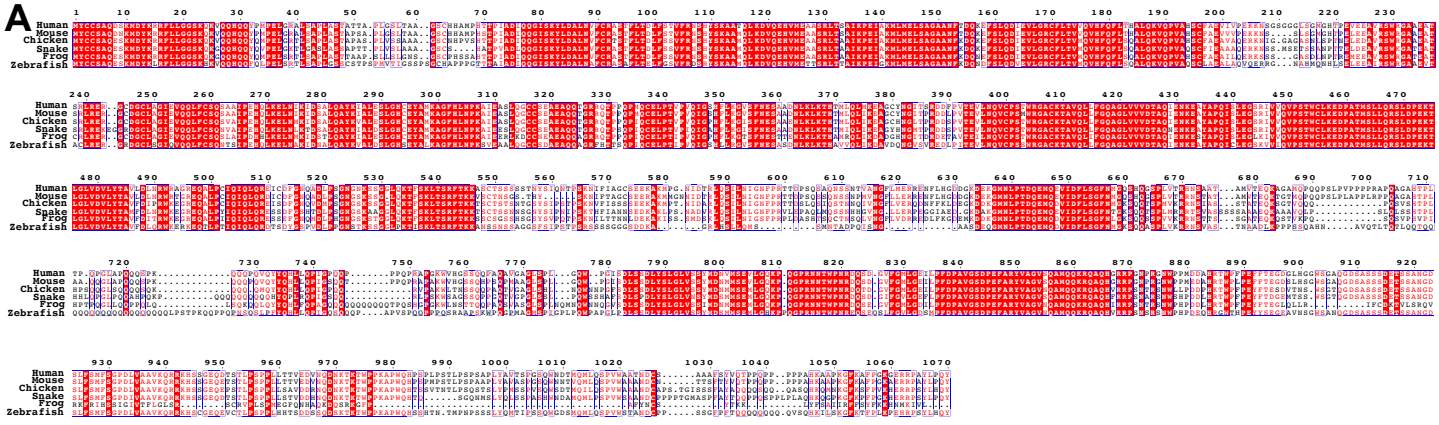

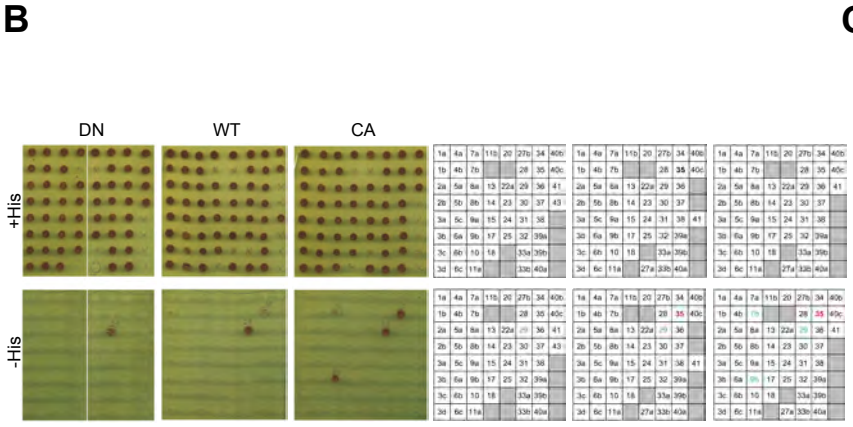

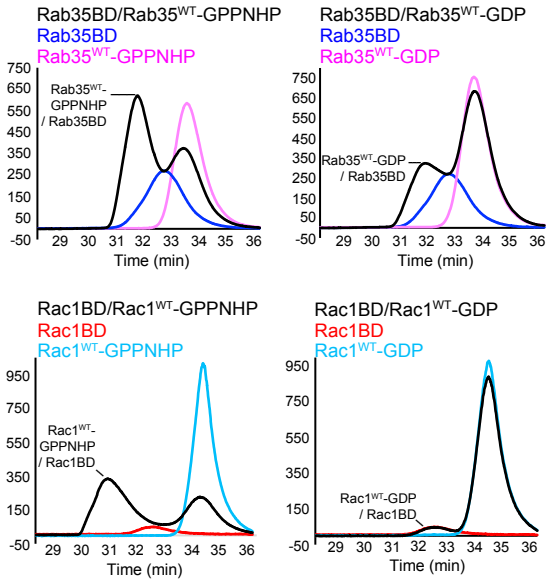

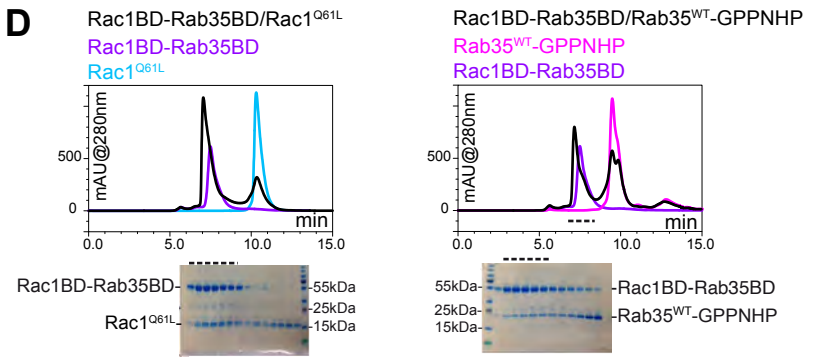

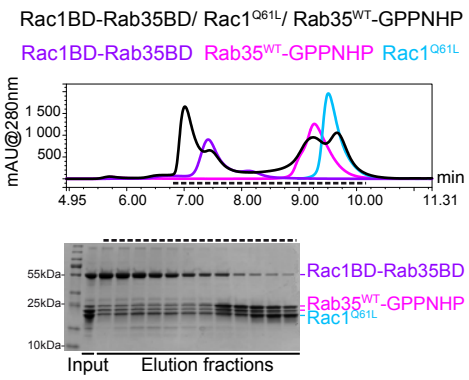

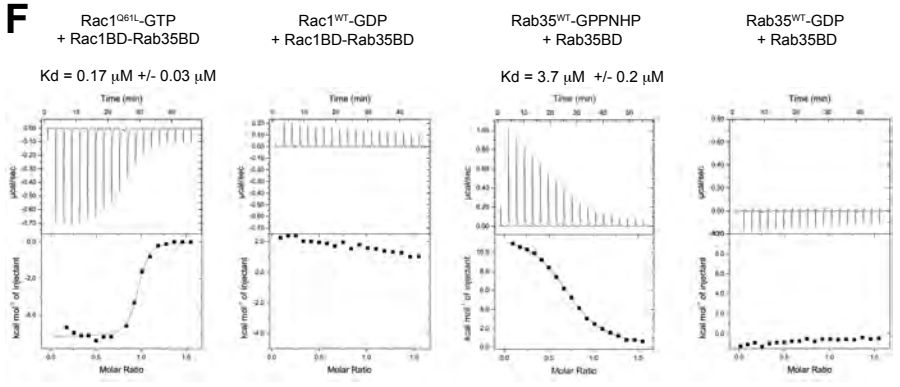

MiniBAR fragment	GTPase	Kd (ITC)
Rab35BD	Rab35WT-aa1-175-GPPNHP	3.7μM +/- 0.2 μM
Rab35BD	Rab35WT-aa1-175-GDP	N.D.
Rab35BD	Rab35WT-aa6-175-GPPNHP	2.07μM +/- 0.17μM
Rab35BD	Rab35WT-aa1-199-GPPNHP	2.8 μM +/- 0.24 μM
Rac1BD-Rab35BD	Rac1Q61L-aa1-177-GTP	0.17 μM +/- 0.03 μM
Rac1BD-Rab35BD	Rac1WT-aa1-177-GDP	N.D.

N.D. = no detected binding

Figure S1

Figure S1. Alignment of full-length MiniBAR proteins from different species. Specificity of MiniBAR interaction with Rab35. Biochemical characterization of Rac1 and Rab35 interaction with MiniBAR domains, Related to Figure 1.

(A) The N-terminal part of the protein (MiniBAR$^{70-553}$) that binds both Rac1 and Rab35 GTPases is highly conserved in vertebrates, showing 76% identity and 85.5% similarity between human and fish sequences. The C-terminal part of the protein (MiniBAR$^{554-1070}$) is predicted to be intrinsically disordered.

UniProt accession numbers: Human (*Homo sapiens):* O15063; Mouse (*Mus musculus*) Q6PAL5, Chicken (*Gallus gallus*): E1BT43; Frog (*Xenopus tropicalis*): A0A6I8S090; Snake (*Pseudonaja textilis): A0A670YC05* and Zebrafish (*Danio rerio*): A0A0R4IGD5.

(B) *S. cerevisiae* L40 reporter strain was transformed with plasmids encoding Gal4 Activation Domain (GAD) fused to MiniBAR Rab35BD to examine interactions with LexA fused to 55 different human Rab GTPases either wild type (WT) or dominant negative (DN, mutation equivalent to S22N in Rab35) and constitutively active (CA, mutation equivalent to Q67L in Rab35). Growth on a medium without histidine (- His) indicates an interaction with the corresponding proteins in this two-hybrid assay. Among all tested Rab GTPase, only Rab35 WT and CA showed a specific growth (red numbers). Growth with RAB29 and RAB9b is not conclusive since it is observed with any GAD fusions (constitutive growth due to autoactivation by RAB29 and RAB9, blue numbers).

(C) Purified wild type Rab35 and wild type Rac1 proteins were incubated with 10 times molar excess of GPPNHP or GDP in magnesium free buffer supplemented with 10 mM EDTA for 1 hour; then 20 mM MgCl2 was added to terminate the nucleotide exchange; the nucleotides excess was removed from the protein solution by buffer exchange on Sephadex G-25 spin columns. Analytical gel-filtration was performed using Superdex200 increase 10/300 column in 50 mM Hepes pH8, 50 mM NaCl2, 2 mM MgCl2, 2 mM TCEP with 0.5 ml/min flow rate. Protein complexes were prepared by mixing MiniBAR fragments with 1.5 molar excess of corresponding GTPases loaded with indicated nucleotides. Elution was monitored by UV absorbance at 280 nm (Top panels: Rab35BD; Bottom panels: Rac1BD). The elution profiles of complexes were compared with profiles of corresponding individual components. Note the preferential binding of Rab35-GTP to Rab35BD, compared to Rab35-GDP and the exclusive binding of Rac1-GTP to Rac1BD in these experimental conditions.

(D) Analytical gel-filtration elution profiles of individual proteins: Rac1BD-Rab35BD fragment (MiniBAR$^{70\text{-}553}$), Rab35-GPPNHP and Rac1^{Q61L} in comparison with their complexes. The elution fractions corresponding to the complexes elution peaks were analyzed by SDS-PAGE (marked with black dashed lines), masses of the eluted proteins and complexes were determined by MALS and indicated below. Left panel: Rac1BD-Rab35BD ($Mass_{MALS}$ 97.2 $\pm$ 0.7 % kDa), Rac1^{Q61L} ($Mass_{MALS}$ 20.6 $\pm$ 0.3 % kDa), Rac1BD-Rab35BD/Rac1^{Q61L} complex ($Mass_{MALS}$ 123.8 $\pm$ 0.4% kDa). Right panel: Rac1BD-Rab35BD ($Mass_{MALS}$ 97.2 $\pm$ 0.7 % kDa), Rab35-GPPNHP ($Mass_{MALS}$ 22.2 $\pm$ 0.1 % kDa), Rac1BD-Rab35BD/Rab35-GPPNHP complex ($Mass_{MALS}$ 117.1 $\pm$ 0.5 % kDa).

(E) Analytical gel-filtration elution profiles of individual proteins Rac1BD-Rab35BD, His-tagged-Rab35-GPPNHP and Rac1^{Q61L} in comparison with their complexes. His-tagged-Rab35 migrates as a double band. Both GTPases co-elute with the Rac1BD-Rab35BD fragment.

(F) The ITC curves show the interactions between the active state (Rac1^{Q61L} (aa 1-177) bound to GTP) or inactive state (Rac1^{WT} (aa 1-177) bound to GDP) of Rac1 with Rac1BD-Rab35BD (2 left panels) and the active state (Rab35^{WT} (aa 1-175) loaded with GPPNHP) or inactive state (Rab35^{WT} (aa 1-175) bound to GDP) of Rab35 and Rab35BD (2 middle panels). The right table shows the measured Kd for different Rac1/Rab35 constructs bound to indicated nucleotides. N.D.= no detected binding under these experimental conditions.

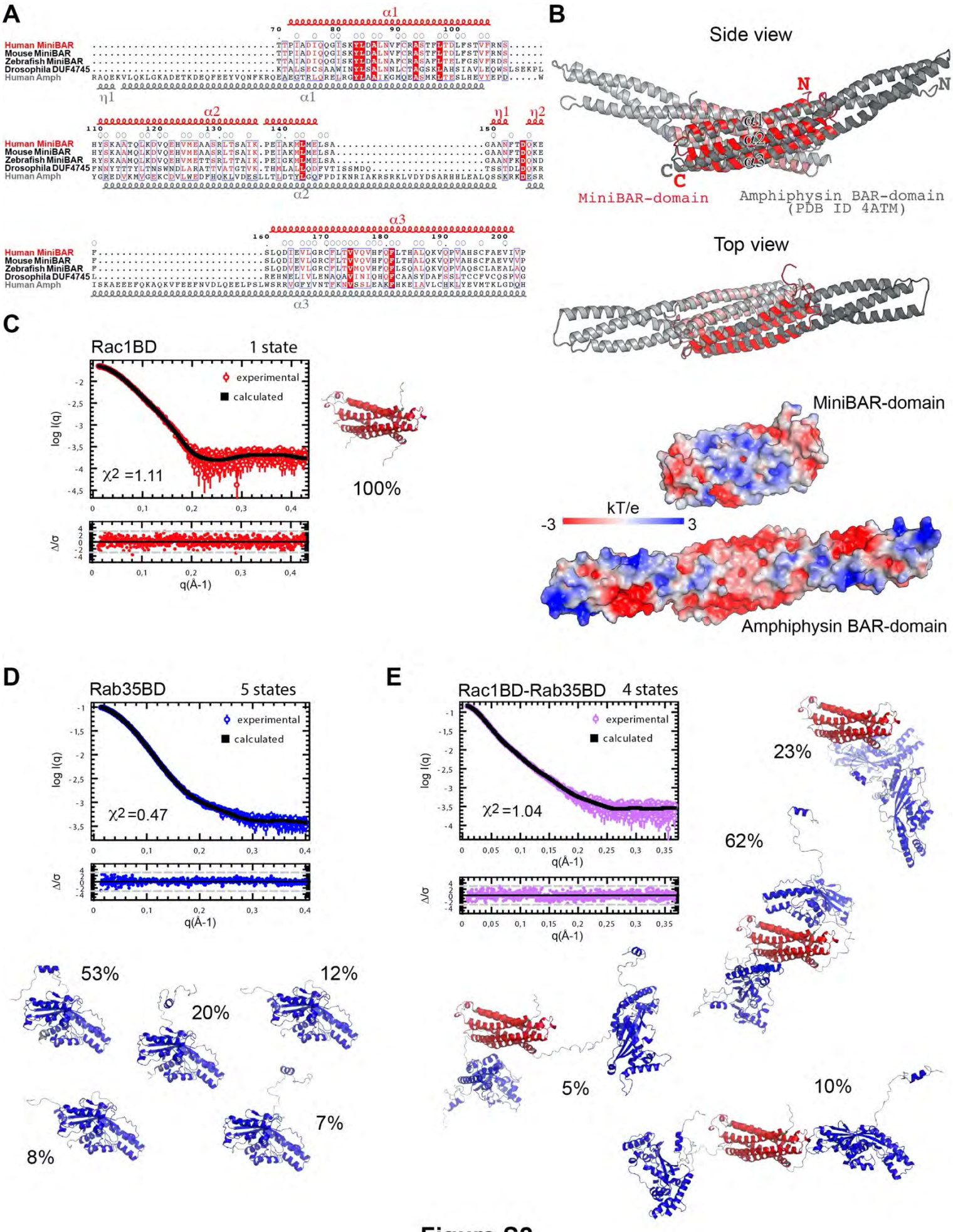
A
α1
70 80 90 100
Human MiniBAR
Mouse MiniBAR
Zebrafish MiniBAR
Drosophila DUF4745
Human Amph
η1
α1
α2
110 120 130 140 150
η1 η2
α2
α3
160 170 180 190 200
α3
B
Side view
N
N
α1
α2
α3
C
C
MiniBAR-domain
Amphiphysin BAR-domain
(PDB ID 4ATM)
Top view
MiniBAR-domain
kT/e
-3
3
Amphiphysin BAR-domain
C
Rac1BD
1 state
experimental
calculated
log I(q)
χ2 =1.11
Δ/σ
q(Å-1)
100%
D
Rab35BD
5 states
experimental
calculated
log I(q)
χ2 =0.47
Δ/σ
q(Å-1)
53%
20%
12%
7%
8%
E
Rac1BD-Rab35BD
4 states
experimental
calculated
log I(q)
χ2 =1.04
Δ/σ
q(Å-1)
23%
62%
5%
10%

Figure S2

Figure S2. Comparison of the truncated BAR domain of MiniBAR and the BAR domain of Amphiphysin. Models of MiniBAR fragments fitted to the SAXS data, Related to Figure 1.

(A) Sequence alignment of the truncated BAR domains from human, mouse and fish MiniBAR with DUF4745 domain (http://pfam.xfam.org/family/DUF4745) from *D. melanogaster* protein (B5RJJ4) and human Amphyphisin BAR domain. Residues participating to the homodimer formation are marked with open circles. Secondary structure elements distribution of the human MiniBAR and human Amphiphysin are shown in red above the alignment and in grey below the alignment, respectively.

(B) Top panels: Side view and Top view of the superimposition of the truncated BAR domain of human MiniBAR (red) on the core part of the canonical human Amphiphysin BAR domain (in grey), a concave homodimer made of 2x3 α-helices usually present in proteins that sense and/or induce membrane curvature. The MiniBAR homodimer interface is mostly hydrophobic. MiniBAR helix-2 and helix-3 are kinked at the positions of Pro-137 and Pro-191 respectively helping the typical BAR domain monomers mutual wrapping. The MiniBAR connection loops between helix-1 and helix-2 are short, similar to the Amphiphysin structure; in contrast, the helix-2 and helix-3 are connected with a longer flexible loop, replacing the "arm" regions formed by the extensions of the helix-2 (C-terminal part), helix-3 (N-terminal part) and helix-1 (N-terminal part) of Amphiphysin.

Bottom panels: Electrostatic potential distribution maps on the surfaces of truncated BAR of human MiniBAR and the canonical BAR of human Amphiphysin at the top view orientation.

(C-E) Models of MiniBAR fragments fitted to the SAXS data using MultiFoXS algorithm. Fitting curves and error weighted residual plots of the models. Different states representative models and the state populations are also shown: 1 state for Rac1BD (C), 5 states for Rab35BD (D) and 4 states for Rac1BD-Rab35BD (E).

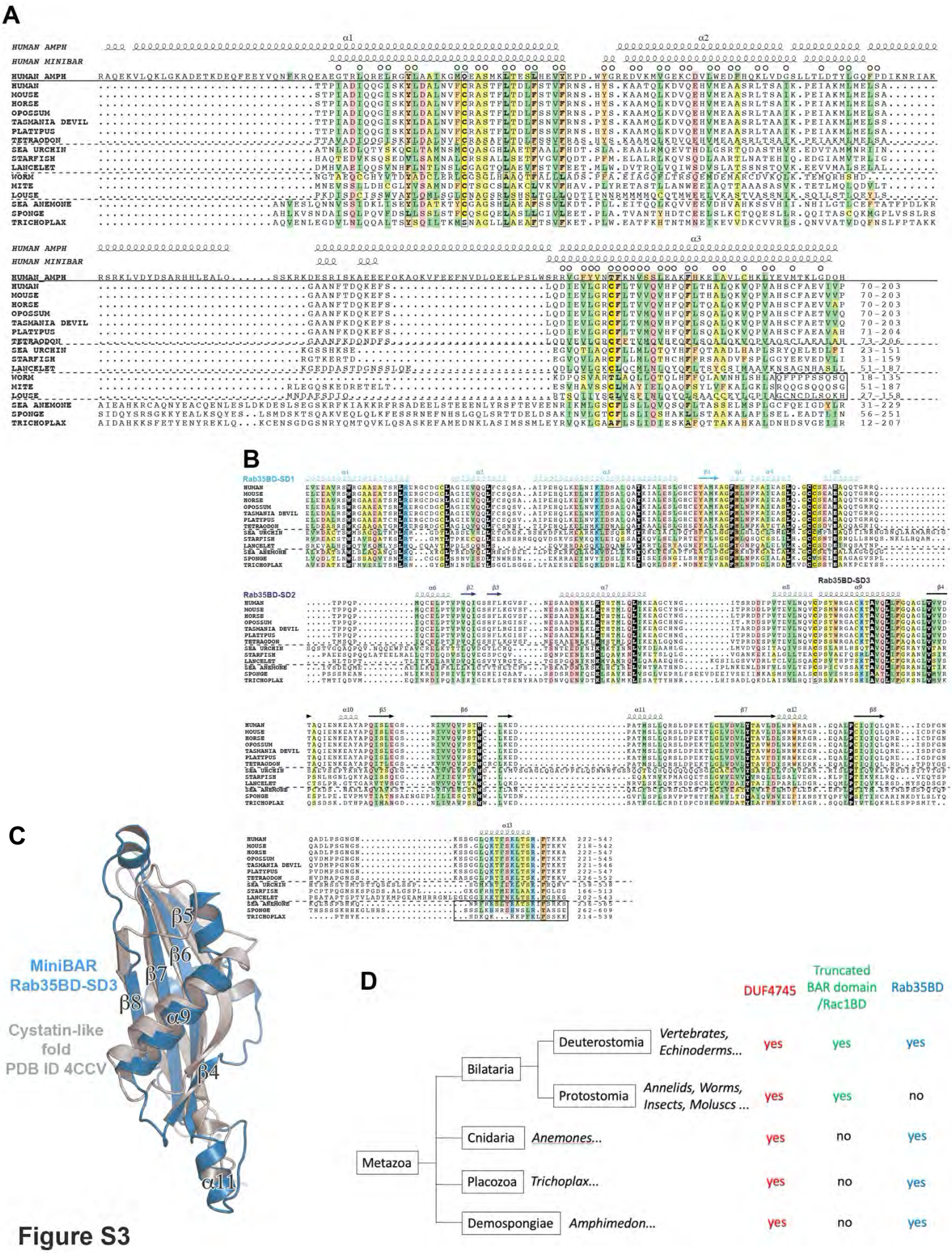
A
B
C
D
MiniBAR
Rab35BD-SD3
Cystatin-like
fold
PDB ID 4CCV
β5
β6
β7
β8
α9
β4
α11
Metazoa
Bilataria
Deuterostomia
Vertebrates,
Echinoderms...
Protostomia
Annelids, Worms,
Insects, Moluscs ...
Cnidaria
Anemones...
Placozoa
Trichoplax...
Demospongiae
Amphimedon...
DUF4745
Truncated
BAR domain
/Rac1BD
Rab35BD
yes
yes
yes
yes
yes
yes
yes
no
yes
yes
no
yes
yes
no
yes

Figure S3

Figure S3. Alignment of full-length MiniBAR, Rac1BD and Rab35BD in multiple species across evolution. Comparison of Rab35BD-SD3 and a cystatin-like fold, Related to Figure 1.

(A-B) Sequence alignments of Rac1BD (A) and Rab35BD (B) from different species, based on MAFFT run on the EMBL-EBI server [S1] and rendered using ESPript [S2]. In (A), the sequence of Amphiphysin, which displays a normal BAR domain, is given for comparison. Note that Sponges, Placozoa and Cnidaria have a normal BAR domain.

The secondary structures of experimental 3D structures (Human Amphiphysin: pdb 4ATM, Human MiniBAR: this study) are reported above the alignment, with residues participating in the dimer formation indicated with open circles, as in Figure S2A. Boxes indicate more variable regions, with uncertain alignment and for which differences are observed in the AF2 models. Colors are used to highlight positions for which conserved features observed (green: strong hydrophobic amino acids (V, I, L, M, F, Y, W); orange: aromatic amino acids (F, Y, W, H); light green: small, non-strong hydrophobic amino acids (A,G,C) and amino acids that can substitute for them (S, T); red : D,E,Q,N,S,T; blue : K,R,H).

UniProt accession numbers: HUMAN (*Homo sapiens*): O15063; MOUSE (*Mus musculus*): Q6PAL5; HORSE (*Equus caballus*): F7DL01; OPOSSUM (*Monodelphis domestica*): F7B911; TASMANIA DEVIL (*Sarcophilus harrisii*): A0A7N4NPN4; PLATYPUS (*Ornithorhynchus anatinus*): F7BGA3; TETRAODON (*Tetraodon nigroviridis*): H3CYU6; SEA URCHIN (*Strongylocentrotus purpuratus*): A0A7M7N6V8; STARFISH (*Acanthaster planci*): A0A8B7YHJ9; LANCELET (*Branchiostoma belcheri*): A0A6P5A9Y3; WORM (*Capitella teleta*): R7TMM2; MITE (*Varroa destructor*): A0A7M7J8J6; LOUSE (*Pediculus humanus*): E0W1T5; SEA ANEMONE (*Actinia tenebrosa*): A0A6P8H0T2; SPONGE (*Amphimedon queenslandia*): A0A1X7V5V2; TRICHOPLAX (*Trichoplax adhaerens*): B3RJE9.

(C) Rab35BD SD-3 superimposed on a cystatin fold representative structure (PDB 4CCV) using vector alignment search tool [S3]. In Rab35BD, the N-terminal SD-1 is mostly α-helical, it contains 5 α helices (α1-α5) and only one β strand (β1). SD-2 is formed by 3 helices (α6-α8) and two antiparallel β strands (β2 and β3). In Rab35BD, the C-terminal subdomain (SD-3) is formed by an extended 4-stranded β sheet with two α helices (α9 and α12) on the opposite surfaces of the sheet and two helical inserts (α10 and α11) in the loops connecting the β strands. β-strand from SD-1 extends the central SD-3 β-sheet at one edge and the two SD-2 β strands from another edge, thus forming a single 7 stranded mixed β sheet.

(D) Presence of DUF4745, of a truncated BAR domain/Rac1BD and of a Rab35BD across evolution. Note that the DUF4745 is ancient in metazoa, and that the truncated BAR domain is specific of Bilateria. The Rab35BD is ancient and has been lost in Protostomia. Thus, only Deuterostomia (which include Echinoderms, Cephalochordates, Tunicates and Vertebrates) have a truncated BAR domain followed by a Rab35BD.

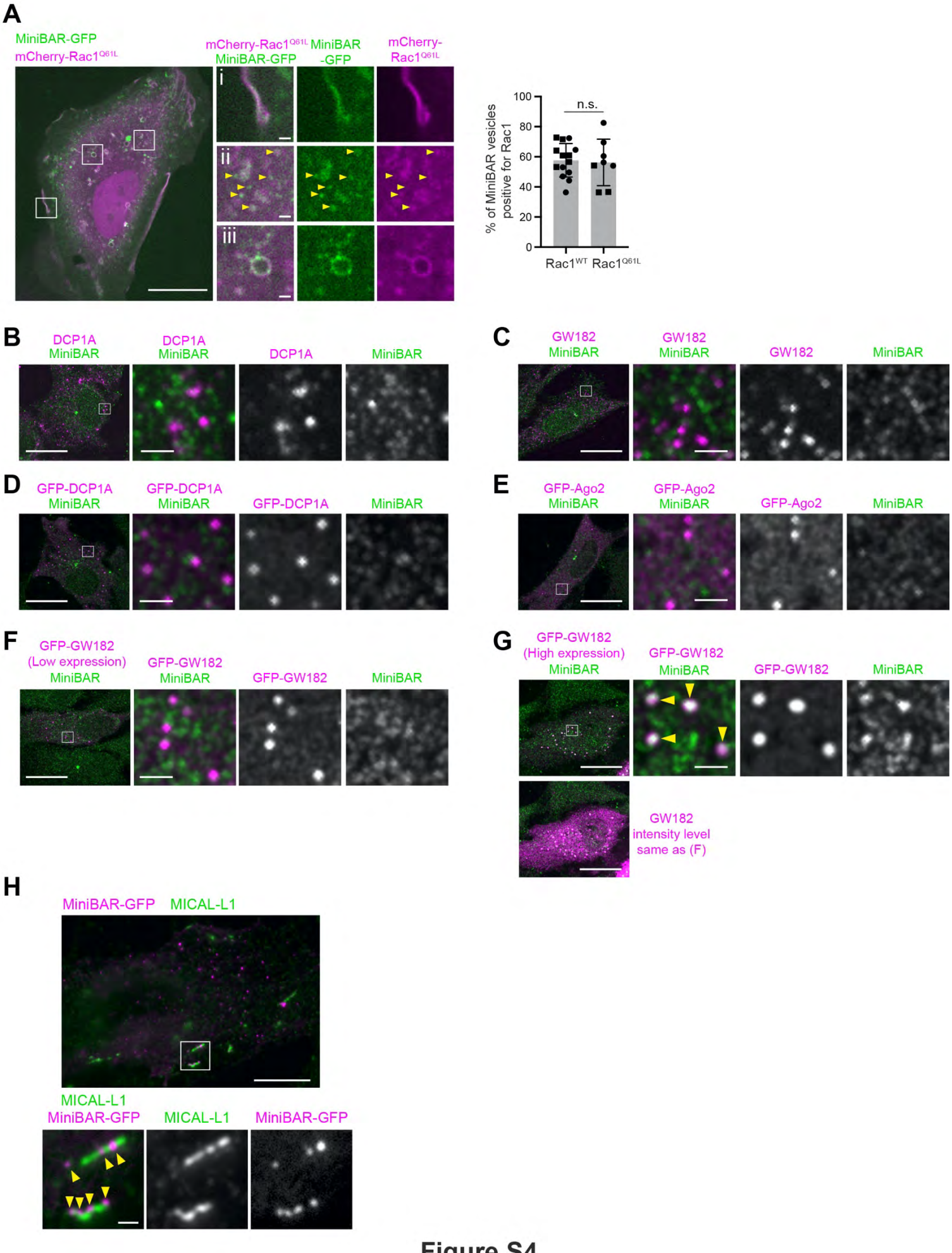
A
MiniBAR-GFP
mCherry-Rac1Q61L
mCherry-Rac1Q61L MiniBAR-GFP
MiniBAR -GFP
mCherry-Rac1Q61L
i
ii
iii
% of MiniBAR vesicles positive for Rac1
100
80
60
40
20
0
n.s.
Rac1WT
Rac1Q61L
B
DCP1A MiniBAR
DCP1A MiniBAR
DCP1A
MiniBAR
C
GW182 MiniBAR
GW182 MiniBAR
GW182
MiniBAR
D
GFP-DCP1A MiniBAR
GFP-DCP1A MiniBAR
GFP-DCP1A
MiniBAR
E
GFP-Ago2 MiniBAR
GFP-Ago2 MiniBAR
GFP-Ago2
MiniBAR
F
GFP-GW182 (Low expression) MiniBAR
GFP-GW182 MiniBAR
GFP-GW182
MiniBAR
G
GFP-GW182 (High expression) MiniBAR
GFP-GW182 MiniBAR
GFP-GW182
MiniBAR
GW182 intensity level same as (F)
H
MiniBAR-GFP MICAL-L1
MICAL-L1 MiniBAR-GFP
MICAL-L1
MiniBAR-GFP

Figure S4

Figure S4. Respective localization of MiniBAR and P-granule markers. Localization of MiniBAR and MICAL-L1, Related to Figure 2.

(A) Left panels: Snapshot of a movie of RPE-1 cells stably co-expressing MiniBAR-GFP and transfected with mCherry-Rac1^{Q61L}. Scale bars, 20 μm (general view) and 2 μm (zooms). Zooms of indicated regions: (i) plasma membrane, (ii) vesicles and (iii) macropinosome. Arrowheads indicate colocalization on vesicles. Right panel: percentage of MiniBAR-GFP vesicles positive for mCherry-Rac1^{Q61L}. Mean ± SD, n = 32-124 MiniBAR-positive vesicles per cell, n = 8-14 cells per condition.

(B) Representative image of RPE-1 cells stained with endogenous MiniBAR and endogenous DCP1A. Scale bars, 20 μm (general view) and 4 μm (insets of the boxed regions).

(C) Representative image of RPE-1 cells stained with endogenous MiniBAR and endogenous GW182. Scale bars, 20 μm (general view) and 4 μm (insets of the boxed regions).

(D) Representative image of RPE-1 cells transfected with plasmids encoding GFP-DCP1A and stained for endogenous MiniBAR. Scale bars, 20 μm (general view) and 4 μm (insets of the boxed regions).

(E) Representative image of RPE-1 cells transfected with plasmids encoding GFP-Ago2 and stained for endogenous MiniBAR. Scale bars, 20 μm (general view) and 4 μm (insets of the boxed regions).

(F-G) Representative images of RPE-1 cells transfected with plasmids encoding GFP-GW182 at low levels (F) or high levels (G) and stained for endogenous MiniBAR. Scale bars, 20 μm (general view) and 4 μm (insets of the boxed regions). In (G) top panels, the display of the magenta channel has been reduced for better visualization of the colocalization with MiniBAR. The magenta levels in the bottom picture have been set as in (F) for comparison of the expression levels.

In B-G, note that endogenous MiniBAR did not co-localize with endogenous markers of P-granules (DCP1A, GW182) (B-C) nor with GFP-DCP1A, GFP-Ago2 or GFP-GW182 when expressed at low levels (D-F). Only when over-expressed at high levels, did GFP-GW182 (but not GFP-DCP1 or GFP-Ago2) colocalize with endogenous MiniBAR (G).

(H) Representative image of RPE-1 cells transfected with plasmids encoding MiniBAR-GFP and stained for endogenous MICAL-L1, as indicated. Scale bars, 20 μm (general view) and 2 μm (insets of the boxed regions).

In A-H, cells were cultured in medium with serum.

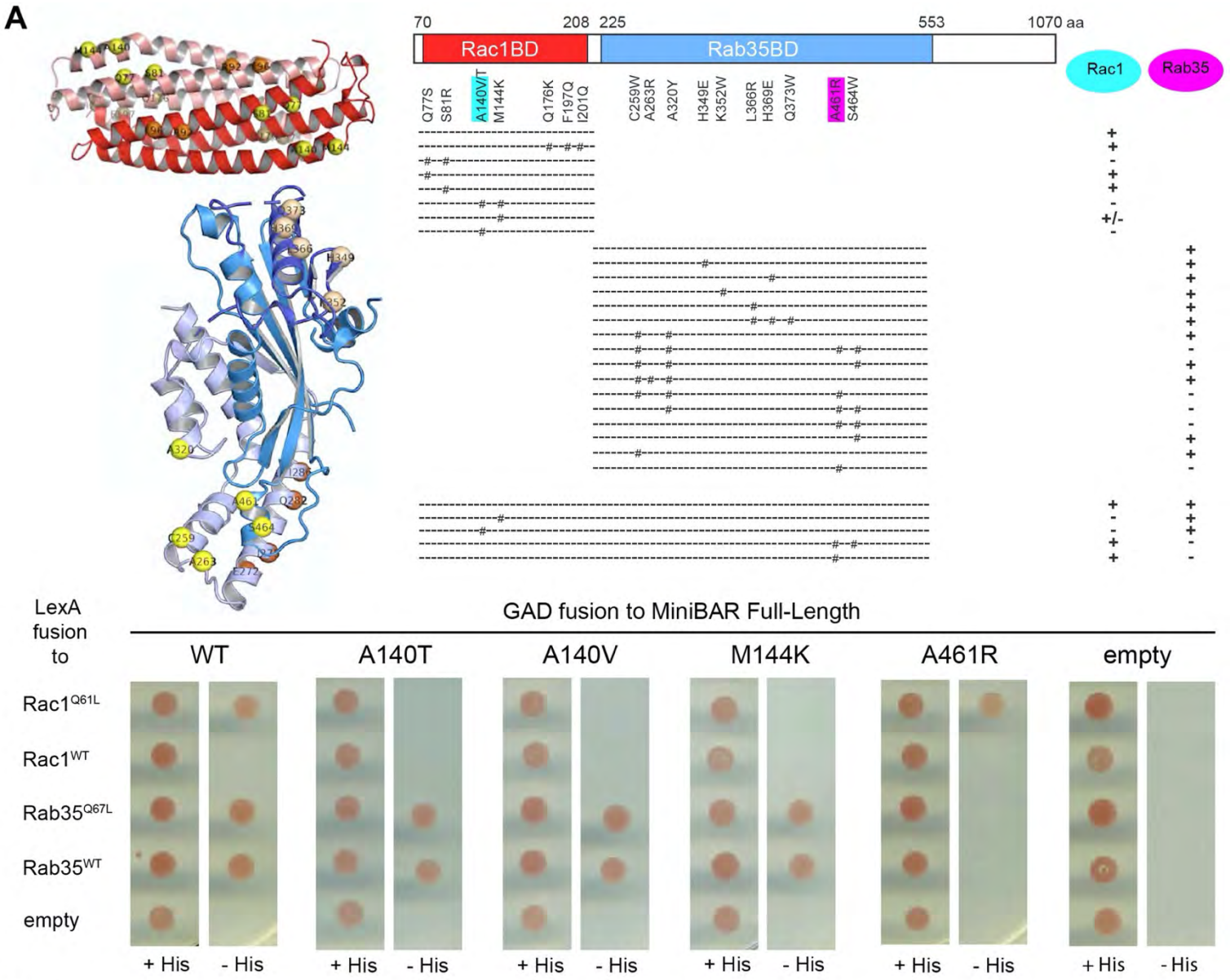
A
70
208
225
553
1070 aa
Rac1BD
Rab35BD
Rac1
Rab35
Q77S
S81R
A140V/T
M144K
Q176K
F197Q
I201Q
C259W
A263R
A320Y
H349E
K352W
L366R
H369E
Q373W
A461R
S464W
LexA fusion to
GAD fusion to MiniBAR Full-Length
WT
A140T
A140V
M144K
A461R
empty
Rac1Q61L
Rac1WT
Rab35Q67L
Rab35WT
empty
+ His
- His

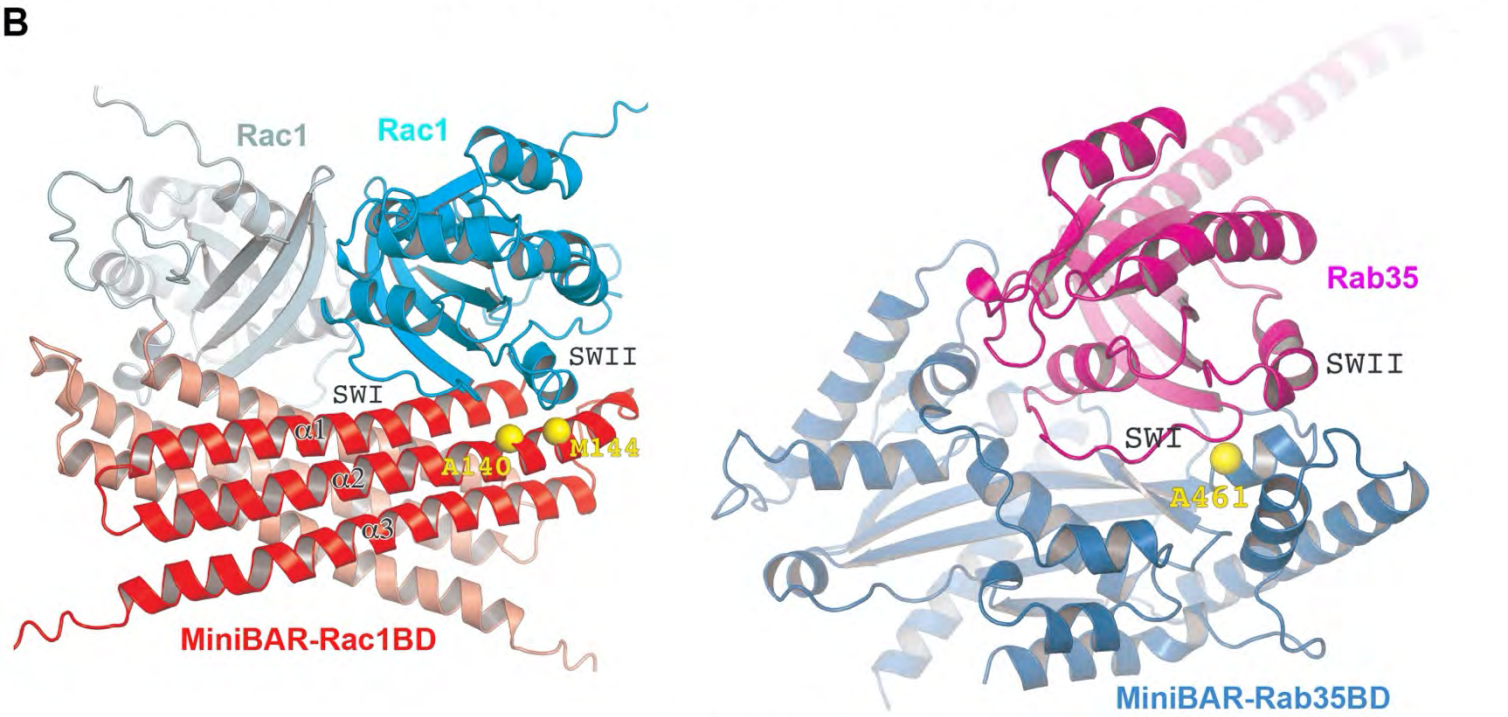
B
Rac1
Rac1
SWII
SWI
α1
α2
α3
A140
M144
MiniBAR-Rac1BD
Rab35
SWII
SWI
A461
MiniBAR-Rab35BD

Figure S5

Figure S5. Screening for point mutations that selectively disrupt MiniBAR interactions with either Rac1 or Rab35, Related to Figure 2.

(A) Left panel: The localization of the aa mutated in the Rac1BD (top) and in the Rab35BD (bottom) are shown as spheres. Right panel: Summary of the combined and single aa substitutions (#) in the Rac1BD, the Rab35BD and in the full-length MiniBAR tested in yeast 2-hybrid for interactions with either LexA-Rac1^{Q61L} or LexA-Rab35 ^{Q67L} fusions. +, ± and - indicate normal, weak and no growth of L40 reporter strain in the absence of Histidine, respectively. Bottom panel: results of the growth of the reporter L40 strain of single amino acid substitution in full-length MiniBAR, as indicated. Growth on a medium without histidine (- His) indicates an interaction with the corresponding proteins in this 2-hybrid assay.

(B) Left panel: AlphaFold predicted complex structure of Rac1BD with Rac1. The prediction is consistent with the A140 and M144 involvement in Rac1 binding shown in (A) and Figure 2E. Right panel: AlphaFold predicted complex structure of Rab35BD with Rab35. The prediction is consistent with the A461 involvement in Rab35 binding shown in (A) and Figure 2F.

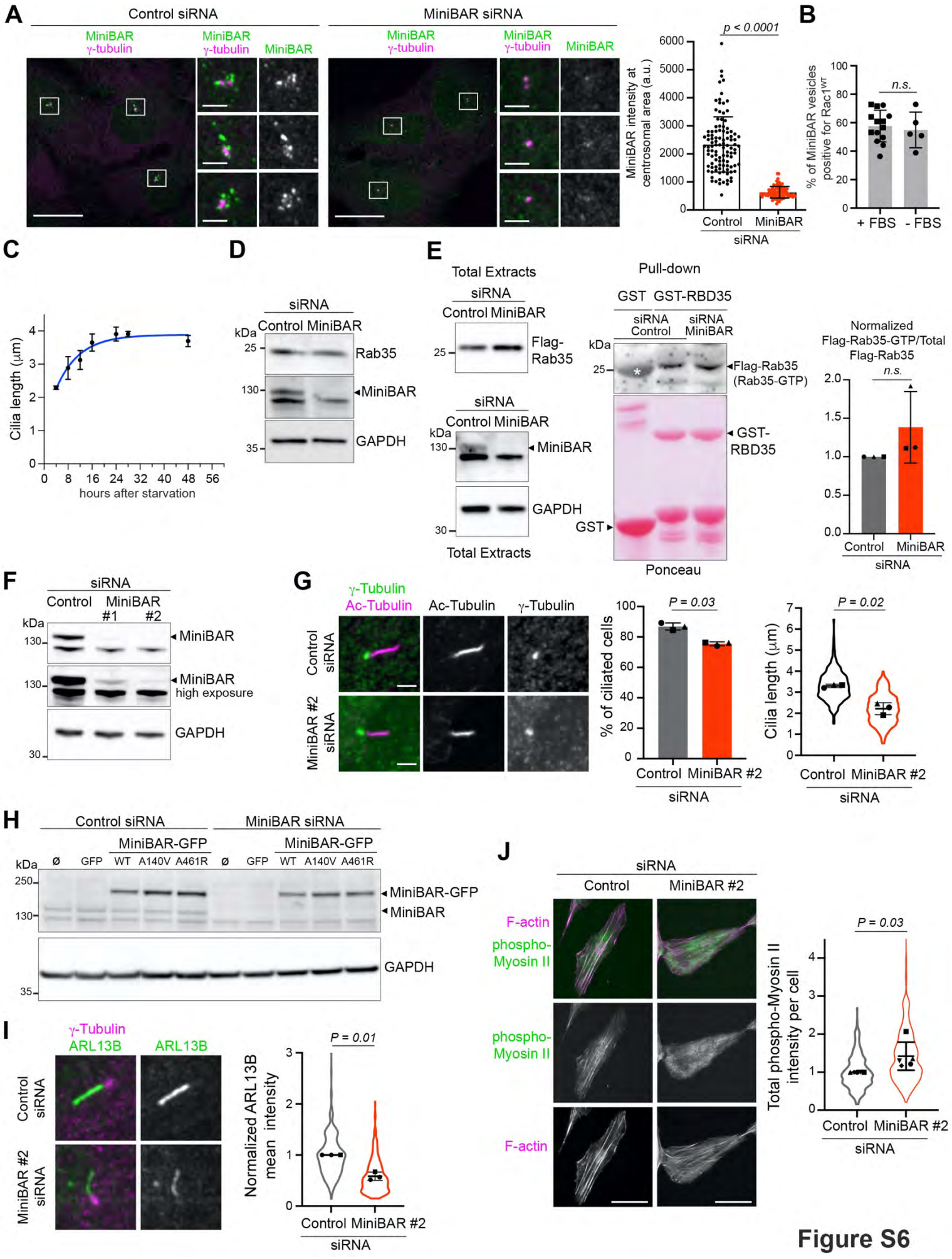
A
Control siRNA
MiniBAR siRNA
MiniBAR
γ-tubulin
MiniBAR intensity at centrosomal area (a.u.)
p < 0.0001
Control
MiniBAR
siRNA
B
% of MiniBAR vesicles positive for Rac1WT
n.s.
+ FBS
- FBS
C
Cilia length (μm)
hours after starvation
D
siRNA
Control MiniBAR
kDa
Rab35
MiniBAR
GAPDH
E
Total Extracts
Pull-down
GST GST-RBD35
Flag-Rab35
Flag-Rab35 (Rab35-GTP)
GST-RBD35
GST
Ponceau
Normalized Flag-Rab35-GTP/Total Flag-Rab35
F
Control
MiniBAR #1
MiniBAR #2
MiniBAR high exposure
GAPDH
G
γ-Tubulin
Ac-Tubulin
Control siRNA
MiniBAR #2 siRNA
% of ciliated cells
P = 0.03
Cilia length (μm)
P = 0.02
H
MiniBAR-GFP
WT
A140V
A461R
GFP
MiniBAR-GFP
MiniBAR
GAPDH
I
ARL13B
Normalized ARL13B mean intensity
P = 0.01
J
F-actin
phospho-Myosin II
Total phospho-Myosin II intensity per cell
P = 0.03

Figure S6

Figure S6. Specificity of MiniBAR staining in RPE cells. Levels of MiniBAR in stably expressing cells. Phenotypes upon MiniBAR depletion using an independent siRNA, Related to Figure 4.

(A) Representative images of RPE-1 cells transfected with either control or MiniBAR siRNAs and stained for endogenous MiniBAR and γ-Tubulin. Zoomed regions of the centrosomal area are displayed as well as the quantification of the mean intensity of MiniBAR at the centrosomal area. Scale bars, 20 μm (general view) and 2 μm (insets of the boxed regions).

(B) Percentage of MiniBAR-GFP vesicles positive for mCherry-Rac1^{WT} in RPE-1 cells incubated with serum (+FBS) or serum starved (-FBS) for 4-8 h. Mean ± SD, n = 48-70 MiniBAR-positive vesicles per cell, n = 5-14 cells.

(C) Cilia length (measured with ARL13B staining) following serum removal (time course indicated in hours). n = 50-81 cells per condition. Mean ± SD from triplicate.

(D) Lysates of RPE-1 cells transfected with control or MiniBAR siRNAs were blotted for endogenous Rab35, MiniBAR and GAPDH (loading control).

(E) Left panel: Total lysates of RPE-1 cells treated with control or MiniBAR siRNAs and transfected with Flag-Rab35^{WT} were blotted for MiniBAR and GAPDH (loading control). Amounts of lysates have been adjusted for pull down experiments to use similar levels of Flag-Rab35 in control and MiniBAR depleted cells. Middle panel: Pull-down of Flag-Rab35^{GTP} from lysates of control- and MiniBAR-depleted RPE-1 cells, and revealed with anti-Flag antibody. Rab35^{GTP} but not Rab35^{GDP} binds to GST-RBD35 (RUSC2). Asterisk: background levels of GST, below the Flag-Rab35 size. Right panel: quantification of Flag-Rab35^{GTP} over total Flag-Rab35. Normalized mean ± SD, N = 3 independent experiments. Unpaired student *t*-test.

(F) Lysates of RPE-1 cells transfected with either control siRNAs, MiniBAR siRNAs used in other experiments (MiniBAR#1) or MiniBAR#2 siRNAs were blotted for MiniBAR and GAPDH (loading control).

(G) Left panel: Representative images of cilia in control- and MiniBAR-depleted cells using MiniBAR#2 siRNAs, 48 h after serum removal. Scale bars, 2 μm. Middle panel: Percentage of control- and MiniBAR-depleted cells with cilia (with ARL13B-positive axonemes) measured 48 h after serum removal. Mean ± SD, N = 3 independent experiments. Paired student *t*-test. Right panel: Cilia length based on ARL13B staining in the aforementioned cells. Mean ± SD, n = 65-98 cells per condition, N = 3 independent experiments. Paired student *t*-test. In these

and all subsequent "violin plots", the mean of each experiment as well as the distribution of all data points are indicated.

(H) Lysates of RPE-1 cells stably expressing the indicated constructs and transfected with either control or MiniBAR siRNAs were blotted for MiniBAR and GAPDH (loading control).

(I) Left panel: Representative images of cilia in control- and MiniBAR-depleted cells using MiniBAR#2 siRNAs, 48 h after serum removal and stained for ARL13B. Scale bars, 2 μm. Right panel: mean ARL13B intensity in cilia in the aforementioned cells. Normalized mean ± SD, n = 69-91 cells per condition, N = 3 independent experiments. Paired student *t*-test.

(J) Left panels: F-actin and phospho-S19 Myosin Regulatory Light Chain staining in control- and MiniBAR-depleted cells using MiniBAR#2 siRNAs, 48 h after serum removal. Scale bars, 20 μm. Right panel: total phospho-S19 Myosin Regulatory Light Chain intensity in the aforementioned cells. Normalized mean ± SD, n = 49-74 cells per condition, N = 5 independent experiments. Unpaired student *t*-test.

In B-E, G and I-J, cells were cultured in medium without serum unless mentioned in B. In A, E and F, cells were cultured in medium with serum.

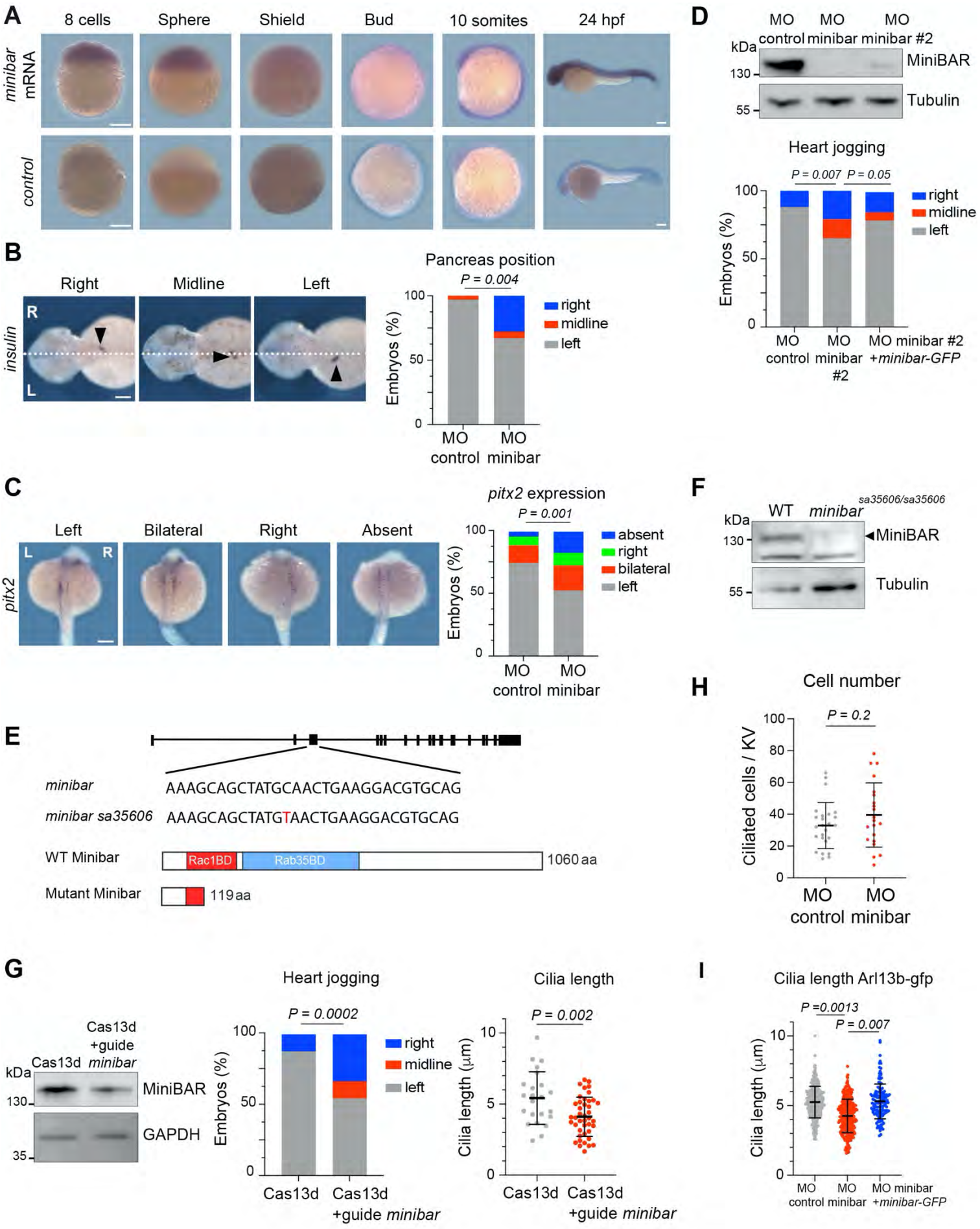
A
8 cells
Sphere
Shield
Bud
10 somites
24 hpf
minibar mRNA
control
B
Right
Midline
Left
insulin
R
L
Pancreas position
P = 0.004
Embryos (%)
right
midline
left
MO control
MO minibar
C
pitx2 expression
P = 0.001
absent
right
bilateral
left
D
MO control
MO minibar
MO minibar #2
kDa
130
55
MiniBAR
Tubulin
Heart jogging
P = 0.007
P = 0.05
MO minibar #2 +minibar-GFP
E
minibar
AAAGCAGCTATGCAACTGAAGGACGTGCAG
minibar sa35606
AAAGCAGCTATGTAACTGAAGGACGTGCAG
WT Minibar
Rac1BD
Rab35BD
1060 aa
Mutant Minibar
119 aa
F
WT
minibar
sa35606/sa35606
H
Cell number
P = 0.2
Ciliated cells / KV
G
Cas13d
Cas13d +guide minibar
GAPDH
35
Cilia length
P = 0.0002
P = 0.002
Cilia length (μm)
I
Cilia length Arl13b-gfp
P =0.0013
P = 0.007

Figure S7

Figure S7. Expression of *minibar* mRNA during early development. L/R asymmetry defects observed after MiniBAR depletion using several approaches, Related to Figure 6.

(A) Expression of *minibar* visualized by *in situ* hybridization in zebrafish embryos from the 8-cell stage to 24 hpf. Control is the sense probe. Scale bars, 200 µm.

(B) *In situ* hybridization of the pancreatic specific mRNA marker *insulin* at 48 hpf.

Scale bar, 100 µm. Quantification of left, midline and right expression of *insulin*. n = 33 and 21 embryos for control and minibar MO, respectively. Chi-square test.

(C) *pitx2* expression at the 23-somite stage. Scale bar, 200 µm. Quantification of left, bilateral, right and absent expression of *pitx2*. n = 59 and 34 embryos for control and minibar MO, respectively. Fischer exact test.

(D) Top panel: Lysates of 24 hpf zebrafish embryos injected with either a control morpholino (MO control), the morpholino targeting *minibar* (MO minibar) used in Figure 6 or a second *minibar* morpholino (MO minibar #2) were blotted for MiniBAR and Tubulin (loading control). The blot in Figure 6A is a truncated version of this blot. Exposure time has been increased here to show the differences in MiniBAR depletion obtained with the two MOs.

Bottom panel: effect of MO minibar #2 on heart jogging, and partial rescue by co-injection of *minibar-GFP* mRNAs. n = 43 embryos for control MO, 114 for minibar MO#2 and 124 for minibar MO#2 with *minibar-GFP* mRNAs. Chi-square test.

(E) *minibar*^{sa35606} is a point mutation in the third exon, inducing a premature stop codon in the Rac1 binding domain.

(F) Lysates of 24 hpf wild type (WT) or *minibar*$^{sa35606/sa35606}$ embryos were blotted for MiniBAR and Tubulin (loading control).

(G) Injection of Cas13 with guide RNAs targeting *minibar* leads to a reduction of MiniBAR expression (Western blot, left panel), heart jogging defects (middle panel) and a reduction of cilia length in Kupffer's vesicle (right panel).

(H) Number of ciliated cells per Kupffer's vesicle described in Figure 6G. n = 25 and 21 embryos for control and minibar MO, respectively. Unpaired student t-test.

(I) Cilia length in the Kupffer's vesicle in β-actin2:arl13b-gfp embryos injected with either control or minibar MOs. n = 9 embryos and 159 cilia for control and 9 embryos and 187 cilia for minibar MO.

X-ray data collection, structure refinement

Data collection	**Rac1BD**	**Rab35BD**
Beamline	Proxima2	Proxima1
Wavelength [Å]	0.98008	0.97911
Space group	C2	P21212
Unit cell (a, b, c) [Å] (α, β, γ) [°]	 44.714, 65.945, 90.438 90.0, 91.5, 90.0	 60.388, 123.956, 38.068 90.0, 90.0, 90.0
Resolution range [Å] (highest resolution shall)	28.944-1.597 (1.625-1.597)	28.576-1.856 (1.888-1.856)
Total reflections	166288(7691)	89205 (4668)
Unique reflections	34818 (1681)	24856 (1259)
Multiplicity/Anomalous multiplicity	4.8(4.6)	3.6 (3.7)/2.0(2.0)
Completeness (%)/Anomalous completeness (%)	99.9(100)	99.5(100.0)/93.5(97.4)
Mean I/sigma(I)	14.8(2.1)	10.6(2.2)
Wilson B-factor [Å^2]	37	24
R-merge	0.052(0.697)	0.083(0.670)
R-meas	0.058(0.788)	0.098(0.782)
R-pim	0.026(0.362)	0.050(0.398)
CC1/2; CC(ano)	0.999(0.796)	0.996 (0.849); 0.417(0.038)
Refinement		
Resolution range [Å]	28.33 - 1.6 (1.657 - 1.6)	28.58 - 1.86 (1.926 - 1.86)
Reflections used in refinement	34612 (3455)	24696 (2462)
Reflections used for R-free	1738 (151)	1199 (128)
R-work	0.1804 (0.2765)	0.1648 (0.2545)
R-free	0.2189 (0.3067)	0.2138 (0.2684)
Number of non-hydrogen atoms	2275	2473
macromolecules	2050	2202
solvent	225	271
Protein residues	263	292
RMS(bonds) [Å]	0.006	0.010
RMS(angles) [°]	0.73	1.05
Ramachandran favored (%)	100.00	98.93
Ramachandran allowed (%)	0	1.07
Ramachandran outliers (%)	0	0
Rotamer outliers (%)	0.88	0
Average B-factor [Å^2]	38.94	34.67
PDB ID	8BUY	8BUX

SAXS data collection and scattering-derived structural parameters of MiniBAR fragments

Data collection	**Rac1BD**		**Rab35BD**		**Rac1BD-Rab35BD**	
Beamline	SWING		SWING		SWING	
Detector	EIGER-4M		Aviex CCD		EIGER-4M	
Wavelength (Å)	1.033		1.033		1.033	
q range (Å^{-1})	0.0048-0.81		0.0084-0.63		0.0045-0.58	
Sample-detector distance (m)	1.49		1.79		1.99	
Exposure time (ms)	990		750		990	
SEC-SAXS column	Agilent, BioSec5 300		Agilent, BioSec5 300		Superdex200 increase 5/150	
Running buffer	50mM Hepes pH8, 50mM NaCl, 1mM DTT, 2mM MgCl2		50mM Hepes pH8, 50mM NaCl, 1mM DTT, 2mM MgCl2		20mM hepes 7.5 + 150NaCl + 1mM DTT + 5mM MgCl2 + 1mM TCEP	
Protein concentration (mg/ml)/ volume (ml)	10/ 40		20/ 40		25/23	
Structural parameters						
Gunier analysis						
I(0) (cm^{-1})	0.022±0.00029		0.1±0.000082		0.15±0.00018	
Rg (Å)	23.61±0.12		25.47±0.24		44.57±0.24	
qRg limits	0.37-1.29		0.6-1.25		0.39-1.2	
P(r) analysis						
I(0) (cm^{-1})	0.0225±0.0003		0.1016 ±0.00006776		0.1528±0.00015	
Real space Rg from P(r) (Å)	24.080±0.05		25.84±0.029		45.47±0.064	
D_{max} (Å)	78		92		152	
q range	0.0158-0.3383		0.0237-0.3136		0.087-0.28	
Molecular mass (kDa)	monomer	dimer	monomer	dimer	monomer	dimer
Calculated from sequence	15.8	31.6	36.28		52.7	105.4
From SAXS data	31.7		38.5		118.7	
From SEC-MALS	30.1 ± 0.39%		36.4 ± 0.66%		104.1±1.2%	
Model fitting. MultiFoXS						
Number of models in the starting set	10013		10022		10038	
q range for modelling	0.012-0.429		0.014-0.401		0.008-0.368	
Starting model	X-ray structure of Rac1BD (a.a.r. 65-69 – from the fusion, a.a.r. 70-208 from the human MiniBAR dimer), missing loops are modelled		X-ray structure of Rab35BD (a.a.r. 220-224 – from the fusion, a.a.r. 225-553 from the human MiniBAR), missing loops are modelled		X-ray structure of Rac1BD-Rab35BD with modelled loops (a.a.r. 65-69 – from the fusion, a.a.r. 70-548 from the human MiniBAR), missing loops are modelled	
Flexible residues	65-73, 199-208		220-226, 509-531, 541-553		65-73, 199-226, 509-531, 541-548	
Number of states	1	3	1	5	1	4
χ^2	1.11	1.11	1.33	0.47	1.71	1.04
c_1, c_2	1.03, 0.31	1.03, 0.49	1.01, 1,59	1.01, 1.7	1.02, 0.58	1.03, 0.45
Rg values of each state (Å)	23.04	23.04, 23.27, 22.57	24.57	23.90, 25.97, 23.46, 30.23, 25.93	45.24	42.27, 62.30, 43.78, 56.76
Weights w_n	1	0.661, 0.166, 0.174	1	0.119, 0.076, 0.532, 0.207, 0.066	1	0.624, 0.051, 0.220, 0.104

Table S1. X-ray and SAXS data collection and refinement, Related to Figure 1.

References

[S1] Madeira, F., Pearce, M., Tivey, A.R.N., Basutkar, P., Lee, J., Edbali, O., Madhusoodanan, N., Kolesnikov, A., and Lopez, R. (2022). Search and sequence analysis tools services from EMBL-EBI in 2022. Nucleic acids research 50, W276-279. 10.1093/nar/gkac240.

[S2] Robert, X., and Gouet, P. (2014). Deciphering key features in protein structures with the new ENDscript server. Nucleic acids research 42, W320-324. 10.1093/nar/gku316.

[S3] Madej, T., Marchler-Bauer, A., Lanczycki, C., Zhang, D., and Bryant, S.H. (2020). Biological Assembly Comparison with VAST. Methods Mol Biol 2112, 175-186. 10.1007/978-1-0716-0270-6_13.